HIGH TEMPERATURE OXIDATION AND NaCl-INDUCED ACCELERATED CORROSION OF HOT-DIP ALUMINIZED 9Cr-1Mo AND 310 STAINLESS STEEL

A Dissertation

by

CHARNG-CHENG TSAUR

Submitted to the Office of Graduate Studies of
Texas A&M University
in partial fulfillment of the requirements for the degree of

DOCTOR OF PHILOSOPHY

December 2004

Major Subject: Interdisciplinary Engineering

HIGH TEMPERATURE OXIDATION AND NaCl-INDUCED ACCELERATED CORROSION OF HOT-DIP ALUMINIZED 9Cr-1Mo AND 310 STAINLESS STEEL

A Dissertation

by

CHARNG-CHENG TSAUR

Submitted to Texas A&M University
in partial fulfillment of the requirements
for the degree of

DOCTOR OF PHILOSOPHY

Approved as to style and content by:

James C. Rock (Chair of Committee)	George R. Blakley (Member)
Bruce L. Freeman Jr. (Member)	Ian S. Hamilton (Member)
Karen L. Butler-Purry (Head of Department)	

December 2004

Major Subject: Interdisciplinary Engineering

ABSTRACT

High Temperature Oxidation and NaCl-induced Accelerated Corrosion of Hot-dip Aluminized 9Cr-1Mo and 310 Stainless Steel. (December 2004)

Charng-Cheng Tsaur, Dip., National Taipei Institute of Technology;

M.S., National Central University, Taiwan

Chair of Advisory Committee: Dr. James C. Rock

The behaviors of high temperature corrosion on hot-dip aluminized on 9Cr-1Mo and 310 stainless steels when catalyzed by NaCl and cyclic heating environment were studied experimentally. The corrosion behavior and morphological development were investigated by weight gain kinetics, metallographs, depths of attack, metal losses, and X-ray analyses. The results of 310SS deposited with salt mixtures show that weight gain kinetics in simple oxidation reveals a steady-state parabolic rate law after 3 hr, while the kinetics with salt deposits display multi-stage growth rates. NaCl is the main corrosive specie in high-temperature corrosion involving mixtures of $NaCl/Na_2SO_4$ and is responsible for the formation of internal attack. Uniform internal attack is the typical morphology of NaCl-induced hot corrosion, while the extent of intergranular attack is more pronounced as the content of Na_2SO_4 in the mixture is increased.

The thermal-cycling test results of 310SS deposited NaCl and coated 7wt%Si/93wt%Al show that the aluminized layers have good corrosion resistance during the first four cycles of testing, while degradation occurs after testing for five cycles. The reason for degradation of aluminized layers is attributed to the formation of inter-

connecting voids caused by aluminum inward diffusion, chloridation/oxidation cyclic reactions and the penetration of molten NaCl through the voids into the alloy substrate.

The 9Cr-1Mo steels coated with 7wt%Si/93wt%Al oxidized at 750, 850, and 950°C in static air show that oxidation kinetics followed a parabolic rate law at 750 and 850°C. The cracks propagated through the Fe_xAl_y layer due to the growth of brittle $FeAl_2$ and Fe_2Al_5 at 750 and 850°C. The voids condensed in the interface of intermetallics and substrate are attributed to the Kirkendall effect. At 950°C, the fast growing aluminide layer has a different expansion coefficient than oxide scale, leading to scale cracking, oxygen penetration, and internal oxidized, evidenced by a rapid mass gain.

To the memory my father, Dian-Ying Tsaur

ACKNOWLEDGMENTS

At times, I believe my family is more excited than myself at the completion of this Ph.D. program. This is not to say that I am not ecstatic about this accomplishment, just an indication of the love and support that I have received from my family. My dear mother, Da-Mei Chen, my lovely wife, Chi-Lin, my son, Erh-Jenn and my daughter, Yuan, have been extremely supportive in this endeavor. Thank you!

Dr. Rock, what can I say! You have provided me much more than just an education; you have provided me the ability to live with the dynamic world. There are no words to describe the magnitude of my gratitude. Thank you!

I would also like to thank my committee members, Dr. Blakley, Dr. Freeman, and Dr. Hamilton, for their support and help. I would also like to thank Mr. C.F. Di, Mr. S.S. Wu, Dr. D.S. Shi and Dr. C.Y. Gau of the Institute of Occupational Safety and Health, Council of Labor Affairs, Executive Yuan, Republic of China, for making this journey a reality. I would like to thank my government in Taiwan for providing the financial support for me studying abroad. Finally, I would like to personally thank Dr. C.J. Wang and Dr. Y.Y. Chang for making this work a reality. Thanks all of you!

TABLE OF CONTENTS

Page

ABSTRACT iii

ACKNOWLEDGMENTS vi

TABLE OF CONTENTS vii

LIST OF TABLES ix

LIST OF FIGURES x

CHAPTER

I INTRODUCTION 1

II INTRODUCTION OF HIGH TEMPERATURE OXIDATION AND CORROSION 10

A. Thermodynamics considerations 10
B. Formation of protective scale 13
C. Effects of temperature 17
D. Effects of atmosphere compositions 18
E. Effects of alloying elements 20
F. Breakdown of protective scales 23
G. Kirkendall effect 23

III THE HOT CORROSION OF 310 STAINLESS STEEL WITH PRE-COATED $NaCl/Na_2SO_4$ MIXTURES 26

A. Introduction 26
B. Experimental procedure 27
C. Results 30
D. Discussions 40
E. Summary of 310SS hot corrosion with $NaCl/Na_2SO_4$ 45

CHAPTER Page

IV THE EFFECT OF NaCl DEPOSIT AND THERMAL CYCLE ON AN ALUMINIDE LAYER COATED ON 310 STAINLESS STEEL ... 47

A. Introduction ... 47
B. Experimental procedure ... 48
C. Results ... 50
D. Discussion ... 60
E. Summary for hot-dipped aluminizing 310SS ... 68

V THE HIGH-TEMPERATURE OXIDATION BEHAVIOR OF AN ALUMINIDE COATING ON 9Cr-1Mo STEEL ... 69

A. Introduction ... 69
B. Experimental procedure ... 70
C. Results ... 71
D. Discussion ... 80
E. Summary of HAD coated 9Cr-1Mo Steel ... 91

VI THE EFFECT OF NaCl DEPOSIT AND THERMAL CYCLE ON AN ALUMINIDE LAYER COATED ON 9Cr-1Mo STEEL ... 93

A. Introduction ... 93
B. Experimental procedure ... 94
C. Results ... 95
D. Discussion ... 109
E. Summary of HDA 9Cr-1Mo steel with thermal cyclic process ... 113

VII CONCLUSIONS ... 115

REFERENCES ... 121

VITA ... 127

LIST OF TABLES

Page

Table 1 Logarithmic parabolic rate constants (g^2 cm^{-4} s^{-1}) for 310SS oxidized with and without $NaCl/Na_2SO_4$ deposits at 750°C at different time intervals 33

Table 2 The quantitative analyses in the bulk alloy substrate between the voids after cyclic test(wt%) 52

Table 3 The thermal properties of various chlorides at 850°C[94]. 61

Table 4 Summary of 310SS hot corrosion research discovery 117

Table 5 Summary of 9Cr-1Mo steel hot corrosion research discovery 119

LIST OF FIGURES

Page

Fig. 1 Standard free energy of formation of selected oxides as a function of temperature[108] 13

Fig. 2 Schematic showing the effect of chromium in Fe-Cr alloys on oxidation rate and oxide scale structure based on isothermal oxidation studies at 1000^{o}C[40] 14

Fig. 3 The effect of solute content on the transition from internal to external oxidation when the oxygen partial pressure is too low to oxidize element A. (a) Schematic diagram of the cross-section and concentration profile for B when NB is less than the critical value showing internal oxidation. (b) Similar schematic diagram for NB greater than the critical value showing continuous external BO formation[41] 15

Fig. 4 The effect of solute content on the transition from internal to external oxidation when the oxides of both elements can form. (a) Schematic diagram of the cross-section when N_B is less than the critical value showing internal oxidation of B under an external scale of AO. (b) Schematic diagram of'the cross-section when N_B exceeds the critical value and result in the formation of external BO to the exclusion of AO[41] 17

Fig. 5 Oxidation resistance of several stainless steels as a function of temperature[52] 18

Fig. 6 Oxidation resistance of carbon, low-alloy, and stainless steels in air after 1000hr at temperatures from 590 to 930^{o}C[53] 19

Fig. 7 Effects of chromium and/or silicon on the oxidation resistance of steel in air[63] 21

Page

Fig. 8 Schematic of Kirkendall effect[7] 24

Fig. 9 The schematic representation of the spring balance TGA apparatus 29

Fig. 10 Evaporation weight loss of salt deposits at 750°C. (The labels are wt% NaCl / wt% Na_2SO_4) 30

Fig. 11 Corrosion kinetics as a function of square root of time 32

Fig. 12 Corrosion attack and weight gain of 310SS alloy corroded for 24 hr. (correlation coefficient, r=0.96) 34

Fig. 13 Optical cross-sectional micrographs of 310SS corroded for 24 hr. (a)pre-coated $NaCl/Na_2SO_4$ mixtures with the ratio of 100/0, (b) 75/25, (c) 50/50, (d) 25/75, (e) 0/100, (f) simple oxidation in air. (Maker M: Mounting material, E: External scale, S: Subscale, A: Alloy) 35

Fig. 14 (a) EPMA cross-sectional micrograph and X-ray maps of (b) Fe, (c) Cr, (d) Ni, (e) O, (f) Cl, (g) S of 310SS with 75% $NaCl/25\%Na_2SO_4$ mixture corroded for 1 hr. (Maker M: Mounting material, E: External scale, S: Subscale, A: Alloy) 37

Fig. 15 XRD analyses of corrosion products formed on 310SS with $25\%NaCl /75\%Na_2SO_4$ deposits exposed at 750°C for 24 hr detecting from (a) outer side of external scale, (b) inner side of external scale, (c) alloy substrate after light brushing of the external scale 38

Fig. 16 XRD analyses of 310SS corroded with different salts 39

Fig. 17 The hypothetical phase diagram of the $NaCl\text{-}Na_2SO_4$ system[79]. Bullets stand for at experiment temperature 750°C with $NaCl/Na_2SO_4$ compositions 41

Page

Fig. 18 Cross sections of uncoated 310SS deposited with NaCl. (a) four cycles, (b) ten cycles (Maker S: scale; U: subscale; M: matrix) 51

Fig. 19 The total depths of attack of uncoated and coated 310SS deposited with NaCl in each cycle 52

Fig. 20 Optical cross-sectional micrograph of coated 310SS without NaCl deposit exposed at 850°C for seven cycles, at elevated temperature for 20 hr and air-cooling for ten min 53

Fig. 21 (a)Cross-sectional BEI micrograph of Al-coated 310SS with 2 mg/cm^2 NaCl deposit treated at 850°C for 20 hr, and X-ray maps of (b) Al, (c) Fe , (d) Si, (e) Cr, (f) Ni, (g) O, (h) Cl of (a). (Maker S: scale; A: aluminized layer with voids filled with internal oxides in the outer layer; B: the alloy substrate) 55

Fig. 22 XRD analysis of aluminized coated 310SS with repeated NaCl depositing exposed at 850°C for (a) one cycle, (b) four cycles (c) five cycles 56

Fig. 23 (a)Cross-sectional SEI micrograph of Al-coated 310SS with repeated NaCl deposit treated at 850°C for four thermal cycles, and X-ray maps of (b) Al, (c) Fe , (d) Si, (e) Cr, (f) Ni, (g) O, (h) Cl of (a). (Maker S: scale; A: aluminized layer with voids filled with internal oxides; N: Ni-Al layer; B: the alloy substrate) 57

Fig. 24 EDS results showing the concentration variations of Al, Fe, Si, Cr, Ni, and O elements near the surface of the aluminized 310 stainless steel with repeated NaCl depositing exposed at 850°C for four thermal cycles 58

Fig. 25 (a)Cross-sectional SEI micrograph of Al-coated 310SS with repeated NaCl deposit treated at 850°C for five thermal cycles, and X-ray maps of (b) Al, (c) Fe , (d) Si, (e) Cr, (f) Ni, (g) O, (h) Cl of (a).

Page

(Maker S: scale; A: aluminized layer with voids filled with internal oxides; I: internal void zone in the alloy substrate; M: matrix) 59

Fig. 26 Surface morphology of 310SS at 850°C for 9 cycles without coating and depositing 60

Fig. 27 Schematic illustration of corrosion processes on coated 310SS with NaCl deposit in each thermal cycle test. (a) NaCl deposit, (b) oxides form on the surface of the aluminized layer and voids form in the outer aluminized layer, (c) NaCl penetrates through voids and cracks, (d) growth of voids in the aluminized layer, (e) NaCl inward penetration, (f) occurrence of internal attack, (g) NaCl penetrates into the alloy substrate, (h) the aluminized layer breaks away..... 66

Fig. 28 Corrosion kinetics of 9Cr-1Mo steel as function of time at temperature = 950, 850 and 750°C..... 72

Fig. 29 Corrosion kinetics of 9Cr-1Mo steel (square of weight gaining) as function of time at temperature = 950, 850 and 750°C 73

Fig. 30 Optical cross-sectional micrograph of 9Cr-1Mo steel as coated aluminum..... 74

Fig. 31 The phases distribution of Fe-Al intermetallic compound of 9Cr-1Mo steel as coated aluminum..... 75

Fig. 32 Optical surface micrograph of 9Cr-1Mo steel as coated aluminum..... 75

Fig. 33 Optical cross-sectional micrographs of 9Cr-1Mo steel corroded from 45 sec to 56 hr at 750 and 850°C..... 77

Fig. 34 SEI cross-sectional micrographs of 9Cr-1Mo alloy exposed for 8hr at 850 °C..... 78

Page

Fig. 35 SEI cross-sectional micrographs of 9Cr-1Mo alloy exposed for 24hr at 850 ^{o}C 79

Fig. 36 EPMA examination of 9Cr-1Mo alloy specimens for raw material, exposed for 10min and 30min 81

Fig. 37 EPMA examination of 9Cr-1Mo alloy specimens for exposed for 1hr, 8hr and 24hr 82

Fig. 38 9Cr-1Mo steel oxide surface phases spectrums (a)850^{o}C-10min; (b)850^{o}C-60min; (c)850^{o}C-24hr; (d)750^{o}C-8hr, where 850^{o}C-10min is similar to HD-raw; 750^{o}C-8hr is similar to 750^{o}C-24hr..... 83

Fig. 39 9Cr-1Mo steel phases spectrums at 850^{o}C for 8hr from (a)surface to (e)substrate 84

Fig. 40 Optical cross-sectional micrographs except g (g: SEI cross-sectional micrograph, high magnification of FeAl island) of 9Cr-1Mo steel corroded from 4min to 56 hr at 750, 850, and 950°C 87

Fig. 41 Schematic configuration for the stages of growth of aluminized layer and internal voids during oxidation at high temperature. (a) as-coated steel, where Fe-Al consists of $FeAl_3$, Fe_2Al_5, and $FeAl_2$ (1 to 10 min). (b) the growth of the aluminized layer and crack formation (~10 to 30 min). (c) the growth of $FeAl_2$+Fe_2Al_5.(0.3 to 8 hr) (d) the growth of the FeAl phase (0.5 to 56 hr). (e) vacancies formation in Fe_2Al_5+$FeAl_2$. (f) internal voids and oxides formation. (g) the growth of voids and FeAl in the inner layer. (h) the growth of the FeAl phase through the entire aluminized..... 88

Fig. 42 The Fe-Al phase diagram 89

Fig. 43 SEI fractograph of the impact-fractured 9Cr-1Mo steel specimen after exposure for 1hr at 850°C. 90

Page

Fig. 44 (a)Microstructure of annealed 9Cr-1Mo steel, (b) 9Cr-1Mo steel with neither HDA nor NaCl deposit oxidized at 850°C for 7 thermal cycles, (c) uncoated 9Cr-1Mo steel with 2mg/cm^2 NaCl deposit exposed at 850°C for 8 hr..... 97

Fig. 45 XRD analysis of uncoated 9Cr-1Mo steel steel exposure for 8 hr. (a) without NaCl deposit at 750°C; (b) without NaCl deposit at 850°C; (c) outer surface of steel with NaCl deposit at 850°C; (d) same as (c) after careful grinding for removing the external layer 98

Fig. 46 SEI surface topographies of 9Cr-1Mo steel without Al-Si coating exposed for 8 hr. (a) at 750°C without NaCl deposit, (b) at 850°C without NaCl deposit, (c) at 750°C with NaCl deposit, (d) at 850°C with NaCl deposit..... 99

Fig. 47 SEI surface topographies of 9Cr-1Mo steel with Al-Si coating exposed for 8 hr. (a) at 750°C without NaCl deposit, (b) at 850°C without NaCl deposit, (c) at 750°C with NaCl deposit, (d) at 850°C with NaCl deposit..... 100

Fig. 48 Optical cross-sectional micrographs of coated 9Cr-1Mo steel exposure from 1 to 7 cycles at 750 and 850°C, where A represents $FeAl_2$+Fe_2Al_5; B represents FeAl. ((a)~(f): steel coated with Al-Si without NaCl deposit; (g)~(l): steel coated with Al-Si and deposited with NaCl)..... 101

Fig. 49 XRD analysis of Al-Si coated 9Cr-1Mo steel without NaCl deposit tested for 1 cycle at 850°C, detecting from (a)surface to (e)the steel substrate..... 102

Fig. 50 EPMA examination and the corresponding schematic configuration of Al-Si coated steel without NaCl deposit tested for 7 cycles at 750°C..... 103

Page

Fig. 51 XRD analysis of Al-Si coated 9Cr-1Mo steel with NaCl deposit, (a-b) tested for 4 cycles at 850°C; (c-d) tested for 5 cycles at 750°C, where (a)surface, (b)after scale partly removed, (c)surface, (d)after scale partly removed..... 106

Fig. 52 EPMA x-ray maps and the corresponding concentration variations of Al, Fe, Cr, Si and O elements of Al-Si coated 9Cr-1Mo steel with NaCl deposit tested for 2 cycles at 750°C..... 107

Fig. 53 (a) SEM micrograph showing the Al-Si coated 9Cr-1Mo steel specimen with repeated NaCl depositing exposed at 850°C for four thermal cycles, (b) EDS results of the concentration (at.%) of O, Al, Fe, Cr, Si, Cl and Na at positions 1~10..... 108

Fig. 54 SEI micrographs of scales formed on 9Cr-1Mo steel without Al-Si coating and NaCl deposit oxidized at 850°C for 1 cycles..... 110

Fig. 55 A schematic illustration circulation of chlorine in active oxidation mechanism. Where (a) is oxychloridation process, (b) is chloridation process, and (c) is re-oxidation process. 111

Fig. 56 Mechanism of aluminum coating protection..... 112

CHAPTER I

INTRODUCTION

The objective of this research is to investigate experimentally the mechanisms of high temperature oxidation on hot-dip aluminized on 9Cr-1Mo and 310 stainless steel when catalyzed by NaCl, Na_2SO_4 and cyclic heating environment.

An important but poorly understood consequence of the aluminide coating on 9Cr-1Mo and 310 stainless steel is observed as accelerated high temperature oxidation and corrosion. In an NaCl or Cl_2 environment, we do not know how NaCl or Cl_2 affects those steel substrates at high temperature. This is important to modern industrials halides-containing high temperature environments are common in petrochemical industries, incinerators, gas turbines, and marine equipment[1-3].

Additionally, a global issue exists in material selection for incinerators to handle municipal waste. Thus, the material selection at elevated temperature and the corrosion behavior of material employed in incinerators are becoming an increasingly important issue for modern society today. As far as halide is concerned, NaCl is most common in seawater and all kinds of foods and kitchen waste. During incineration, the evaporated salt in air will deposit directly on materials at elevated temperature, or will mix with other ash constituents and deposit onto component surfaces, resulting in severe corrosion attack by oxidation, sulfidation, chloridation and even hot corrosion[3-4]. It has been reported that the corrosion loss of Fe-Ni-Cr alloys in the presence of NaCl at high tem-

---

This dissertation follows the style and format of the Journal of Corrosion Science.

peratures is 30 to 120 times higher than that without NaCl presence[5].

A 9Cr-1Mo alloy is sometimes an adequate substitute for the more expensive stainless steels. 9Cr-1Mo alloy steel, as SA213 T9, is commonly used for heat exchanger tubes because it offers good oxidation and corrosion resistance with good high-temperature strength. The boiler code allows it to be used in thermal environments with temperatures up to 650°C.

On the other hand, 310SS has excellent high temperature properties with good ductility and weldability, and it can resist oxidation in thermal environments with temperature up to 1150°C in continuous service and up to 1140°C in intermittent service[6]. The 310SS has also good resistance to thermal cycling and thermal fatigue. The high chromium content of 310SS, about 25%, tends to support its high temperature properties and gives the alloy good aqueous corrosion resistance. The 310SS alloy exhibits superior resistance to seawater corrosion at normal temperatures about 20-25°C, similar to that of Grade 316SS, and the 310SS alloy exhibits good resistance to carburizing and oxidizing atmospheres at elevated temperature. The 310SS alloy is more resistance to stress corrosion cracking (SCC) than 304SS or 316SS. Taken together, these properties mean that 310SS is usually used at temperatures above 800 or 900°C. Neither 304SS nor 316SS stainless steels are effective at these temperatures.

Al_2O_3 and Cr_2O_3 are known as the most effective oxide forming coatings to slow oxidation of alloys at high temperature. The Al_2O_3-forming alloys showed better corrosion resistance than Cr_2O_3-forming alloys in chlorine-containing environments such as Cl_2-Ar, Cl_2-O_2-Ar, HCl-O_2 and NaCl deposits[7-11].

Strong corrosion resistance is required for high temperature materials, in addition to excellent mechanical properties: high temperature strength, good creep resistance, and microstructure stability. However, these requirements sometimes cannot be achieved simultaneously by alloy development alone. An alternative approach, which mechanical strength is accomplished by alloy development and corrosion resistance by surface coating or surface treatment is commonly used[11].

Due to the superior high temperature corrosion resistance of Al_2O_3-forming alloys and Fe-Al intermetallics[12], aluminum coatings are applied to alloy surfaces. Aluminum coating processes such as hot dipping, thermal spray, pack cementation, slurry, cladding, and electroplating are the most common methods used for coating iron base alloys[13]. An aluminum coating process is selected to accommodate the size and shapes of workpiece, thickness of coating required, accuracy requirement, and cost. On the basis of cost and feasibility, the hot-dip aluminizing process, is the one commonly used for the surface treatment of alloys I propose to study.

Previous studies[11,13] pointed out that alloys with hot-dip aluminum coating reveal excellent oxidation and corrosion resistance in an environment free from halogen and sulfer containing gases. The thin, slow-growing alumina scale acts as a barrier to corrosion and is beneficial to long-term service at high temperature. The dependability of hot-dip aluminum against chloride-induced degradation has rarely been investigated systematically, if ever. So far as I know, there has been no publication of oxidation behavior or of salt mixtures accelerated corrosion related to the hot-dip aluminate coating 9Cr-1Mo and 310 stainless steel. Because the 9Cr-1Mo alloy with hot-dip treat-

ment is often substituted for more expensive stainless steels, I performed corrosion experiments of two iron base alloys, 9Cr-1Mo and 310SS, over the temperature range 750-950°C, with and without NaCl.

There are some papers discussing the high temperature oxidation of industrial Fe-Cr-Mo steel[14-17]. The steel's hardness and resistance to various forms of corrosion are determined by the composition of the oxide layer formed on the alloy at elevated temperatures. The oxide layer forms a duplex structure consisting of iron and chromium oxides at high temperatures. Iron oxide is present at the gas/oxide interface, whereas chromium oxide is closest to the oxide/metal interface. Oxide concentrations depend on the oxidation temperature[16]: below 400°C the oxide layer consists mainly of Fe_2O_3 and a small amount of Cr_2O_3; between 400 and 600°C the oxide layer consists of a mixture of Fe_2O_3 and Cr_2O_3; and above 600°C the layer consists mainly of Cr_2O_3. The composition and thickness of the oxide layer determines the hardness and corrosion resistance of the oxide layer. Additional processes that reduce the strength of steel alloys include: sulfur segregation affection[17], external stress affection[18], steam oxidation, precipitation effects and welding-creep effects in 9Cr-1Mo steel. These have been discussed by other authors[19-34]. However, I found no article discussing the relationship between the hot-dip aluminized and 9Cr-1Mo steel at high temperature.

Low-grade fuels with high concentrations of sulfur, vanadium, and sodium are often used for firing industrial processes, such as oil- and coal-fired power generation. During combustion, alkali metal sulfates and V_2O_5 vapors combine with other ash constituents and deposit onto cooler component surfaces, resulting in severe corrosion attack

by oxidation, sulfidation, chloridation and even hot corrosion. Aircraft engines and the boilers of off-shore industrial rigs undergo hot corrosion when the sodium chloride from the ocean breeze mixes with Na_2SO_4 from the fuel and deposits on hot-section components, leading to accelerated attack of the alloy substrate. The hot corrosion often increases the corrosion loss of heat-resisting alloys by over a hundred times.

The formation of an aluminized layer with a self-healing oxide surface is responsible for the better hot corrosion resistance of as-dipped low carbon steel and 310SS[11]. Furthermore, siliconization treatment provided better high temperature corrosion resistance for 310SS both in air and in a reducing gas environment at elevated temperature[35].

Studies of hot corrosion induced by mixtures of $NaCl/Na_2SO_4$ have generally focused on Ni-base superalloys, and Ni-Cr alloys used in turbine engines or gas turbines. The addition of 10% NaCl in Na_2SO_4 coatings can easily cause the cracking of protective Cr_2O_3 layers and increase the amount of sulfur incorporated into the substrate, accelerating the corrosion of alloys. It has been reported that the most severe hot corrosion attack is observed on Ni- and Co-base alloys at 900°C in still air with mixtures of $NaCl/Na_2SO_4$ containing 40wt% NaCl. The 310SS is a good candidate in using in most parts of the waste incinerator. A slow-going chromia scale can be formed with adequate amounts of chromium content, and act as a protective barrier in oxygen-containing atmospheres. The performance of the steel in oxidizing environments is well established, but its behavior in corrosive environments, particularly those containing chlorides, has not been studied extensively.

NaCl has a major effect on corrosion of uncoated 31SS and sulfur plays an important role in intergranular corrosion. After high-temperature exposure with a 100% NaCl coating, the morphologies of alloy 310 show typical uniform subscale attack and the depths of attack increase with increasing temperature[32]. The surface microstructure of aluminized 310SS mainly consisted of an outer high aluminum-containing layer, an intermediate intermetallic compound layer and a ferritic stainless steel layer followed by the austenitic substrate. Oxidation resistances of 310 stainless steel exhibit a parabolic oxidation behavior at 700°C and 1000°C[34].

Enhanced oxidation resistances were found for the aluminized layers as compared with 310 stainless steel substrate. On the whole, there remains no clear understanding the high temperature oxidation mechanisms, reaction rates, thermal cycling effect, and the corrosion resistance of 9Cr-1Mo steel and 310SS with hot-dip aluminide coated layer. There are five open questions needing to be resolved.

First, what is the high temperature oxidation mechanism for 9Cr-1Mo steel coated with hot-dip aluminide? The oxidation resistance of iron-based alloys depends on thin protective films consisting of the reaction products between the alloy and the atmosphere. The alloys' hardness and resistance to corrosion are determined by the composition of the oxide layer. The oxide layer formed at elevated temperatures has a duplex structure consisting of iron and chromium oxides. Iron oxide is present at the gas/oxide interface, whereas chromium oxide is closest to the oxide/metal interface, with concentrations that depend on the oxidation temperature[15]. 9Cr-1Mo steels showed negligible oxidation rates at the temperatures up to 650°C due to the formation of protective Cr_2O_3. How-

ever, the oxidation rates dramatically rise after 650°C due to the formation of non-protective oxides[3]. Al_2O_3 is known as the most effective oxide forming coatings to slow oxidation of alloys at high temperature. Does it increase the oxidation resistance up to 750 or 850°C as 9Cr-1Mo steels with hot-dipped aluminide? What is the high temperature oxidation behavior for 9Cr-1Mo steels with hot-dipped aluminide? How do the compounds grow and the roles they play at high temperature oxidation?

Secondly, what is the high temperature oxidation mechanism for hot-dipped aluminide 310 stainless steels with and without NaCl and Na_2SO_4? The 310SS has good oxidation resistance in high temperature up 1150°C. Does it can keep the good oxidation resistance at high temperatures under NaCl and Na_2SO_4 environment? Can it increase its oxidation resistance by hot-dipped aluminide deposited with NaCl/ Na_2SO_4 salt? What is the oxidation behavior and microstructure during the high temperature corrosion with NaCl/ Na_2SO_4 salt deposited?

Thirdly, does oxidation rate of 310SS increase at elevated temperature with deposit NaCl or Na_2SO_4? NaCl and Na_2SO_4 play an important role in hot corrosion behavior. Hot corrosion requires a molten salt to be contacted with the alloys. How does the corrosion rate vary with the NaCl/ Na_2SO_4 ratio? How does the corrosion rate vary with the exposure duration for various NaCl/ Na_2SO_4 ratio?

Fourthly, does thermal cycling affect the corrosion more severely or more quickly than under constant high temperature? What is the mechanism to degrade the corrosion resistance of hot-dip aluminized 310SS and 9Cr-1Mo steel? What is microstructure and mechanism to affect the corrosion more severely? Finally, will a coating, such as

aluminum, reduce the rate of oxidation/corrosion under high temperature and thermal cycling?

In order to understand the high temperature oxidation mechanisms, reaction rates, thermal cycling effect, and the corrosion resistance of 9Cr-1Mo steel and 310SS with hot-dipped aluminide, Chapter II briefed some basic theories and effect factors for both of the steels.

Chapter III explored the hot corrosion of 310SS with pre-coated $NaCl/Na_2SO_4$ mixtures at elevated temperature. It emphasized the hot corrosion behavior of the commercial 310SS exposed in chloride and sulfide containing environment. The high-temperature behavior of 310SS with NaCl and/or Na_2SO_4 deposits at temperature between the melting point of NaCl or Na_2SO_4 and the eutectic of $NaCl/Na_2SO_4$ were studied. Both kinetics and morphological development were investigated by means of thermal gravimetric analyses, measurements of corrosion attack, metallographic examination, and the identification of the corrosion products. The relationship between the corrosion morphology and salt compositions was also explored.

Chapter IV explores the effect of thermal cycling on 310SS with and without hot-dip aluminide in NaCl-containing environment. It emphasized the benefits of HD-coating. Effects of the supplying NaCl and the cyclic treatment on the formation of oxide scale morphology were studied. My hypothesis was that the high density Al-Si depositing on the surface of 310SS will produce an increased corrosion resistance due to formation of protective Al_2O_3 oxide scale. The high-temperature corrosion mechanism of an aluminide coating on 310 stainless steel was also be studied.

Chapter V investigated the high-temperature oxidation behavior of an aluminide coating on 9Cr-1Mo steel. It emphasized the high temperature oxidation behavior of the coating layer. The oxidation process was investigated by measuring oxidation attack, probing metallographics, and identifying corrosion products. The mechanisms of corrosion development and void formation were also explored. My hypothesis was that they are due to phase transformation and Kirkendall effect. Further more, I also investigated the formation process of the inter-metallic compounds and its affects on internal oxidation.

Chapter VI investigated the effect of NaCl deposit and thermal cycle on an aluminide layer coated on 9Cr-1Mo Steel. The mechanisms of corrosion and coating protection were studied. Chapter VII concluded my investigations and discoveries.

CHAPTER II

INTRODUCTION OF HIGH TEMPERATURE OXIDATION AND CORROSION

Oxidation is the most important high temperature reaction. Oxidation of metals or alloys takes place when they are heated in a highly oxidizing atmosphere such as air or oxygen. An oxidation reaction is represented by the interaction of metals with oxygen to form oxide. There are a variety of factors on which the oxidation behaviors of a metal depends and the reaction mechanism involved may often be quite complex. An oxidation reaction begins with adsorption of oxygen molecules from the atmosphere, nucleation of oxides, formation of a thin oxidation layer, followed by its growth to a thicker scale[7].

A. Thermodynamics considerations

The second law of thermodynamics predicts whether or not a reaction can occur. Because the conditions most often encountered in high temperature reactions are constant temperature and pressure, the second law is conveniently written in terms of the Gibbs free energy (G):

$$\Delta G = \Delta H - T\Delta S \tag{1}$$

Where ΔH is the enthalpy change and ΔS is the entropy change of the system. Under these conditions the second law states:

$\Delta G < 0$ spontaneous reaction expected

$\Delta G = 0$ equilibrium

$\Delta G > 0$ thermodynamically impossible process

For a chemical reaction, e.g.

$$aA + bB = cC + dD \quad (2)$$

ΔG is expressed as

$$\Delta G = \Delta G^o + RTln[(a^c_C \times a^d_D)/(a^a_A \times a^b_B)] \quad (3)$$

where ΔG^o is the free energy change when all species are present in their standard states; a_A, a_B, a_C and a_D are the activity of element A, B, C and D. An oxidation reaction between a metal (M) and the oxygen gas (O_2) can be written as:

$$M_{(s)} + O_{2(g)} = MO_{2(s)} \quad (4)$$

Thermodynamically, an oxide will form on the surface of a metal when the oxygen potential in the environmental is greater than the oxygen partial pressure in equipment with the oxide (dissociation pressure of the oxide). The standard free energy of the oxidation reaction of Eq (5) is:

$$\Delta G^o = -RT \ln [\, a_{MO2}/(a_{M} \cdot p_{O2})] \quad (5)$$

Where a_{MO2} and a_M are the activities of the oxide and the metal respectively and p_{O2} is the partial pressure of the oxygen gas. Assuming unit activity for the solid constituents, i.e. the metal and oxide, the Eq. (5) becomes:

$$\Delta G^o = RT \ln (p_{O2}) \quad \text{or} \quad (6)$$

$$p_{O2} = \exp (\Delta G^o/RT) \quad (7)$$

Eq. (7) permits the determination of the partial pressure of oxygen in equilibrium with the oxide from the standard free energy of formation. A plot of the standard free standard energies for the formation of oxides as a function of temperature is known as Ellingham/Richardson diagram as shown in Fig. 1 Salient features of the Ellingham dia-

gram as follows:

1. The free energy of the most metals shows linear relationship with temperature with a positive slope. This implies that most of the oxidation reactions take place with decrease in entropy.
2. The change in the slope of the lines at certain points indicates a phase change in the metal. This could be melting, boiling, or a change in structure.
3. The most stable oxide has the largest negative value of ΔG^o and is presented by the lowest line in the diagram.
4. Determination of the oxygen potential values.

One of the most important applications of the Ellingham diagram is the determination of equilibrium dissociation pressure of oxides at various temperatures. The free energy change of a reaction in terms of the partial pressure of the gas is written as

$$\Delta G = \Delta G^o + RT \ln (p_{O2}) \tag{8}$$

which is numerically equal to the decrease in the free energy of one mole of oxygen when its partial pressure is decreased from 1 atmosphere to p_{O2} at the temperature T. Oxygen partial pressure can be read by drawing a straight line from the point marked "O" on the left vertical axis of Fig. 1 through the free energy line of the oxide at the temperature of interest[36].

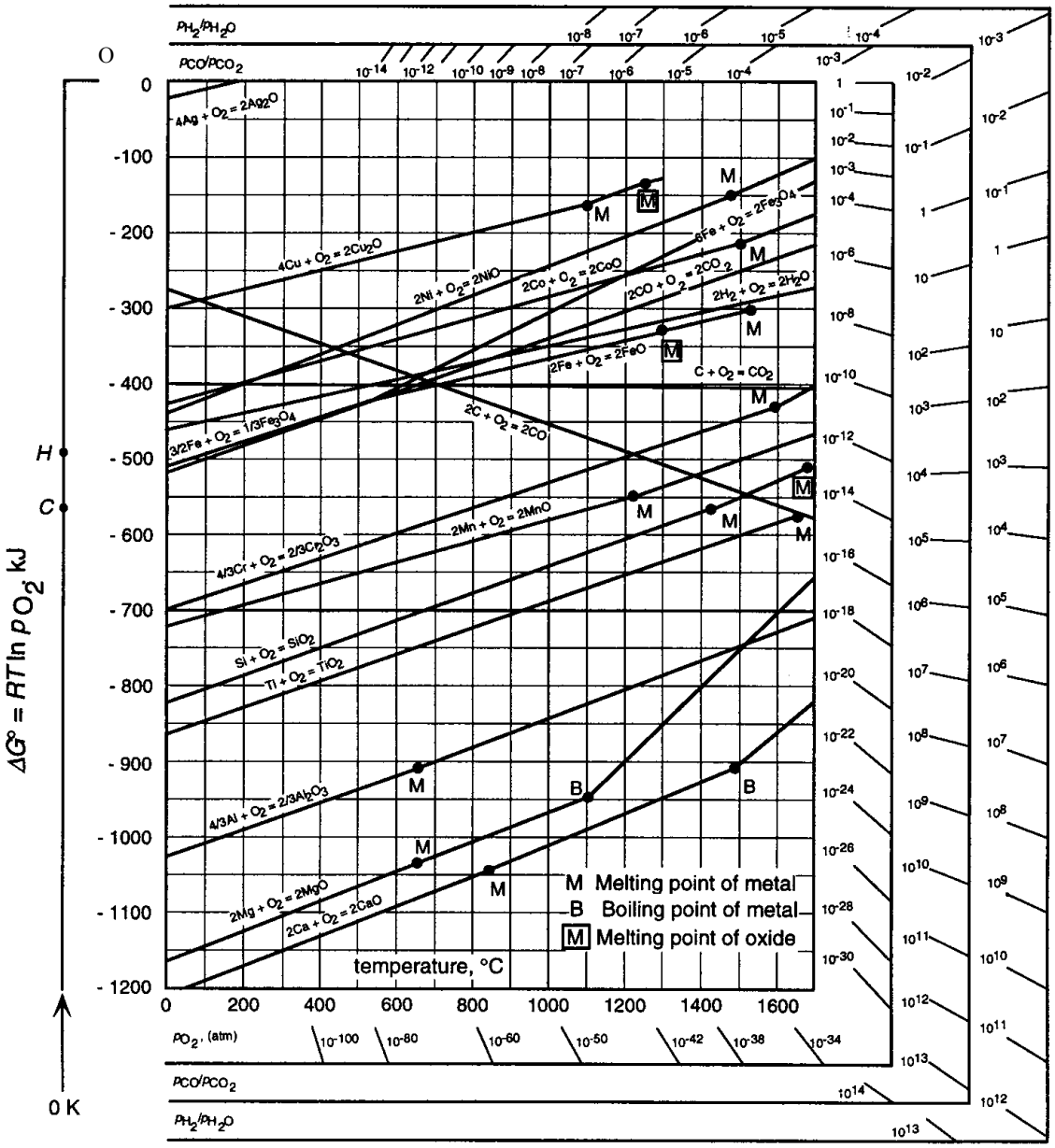

Fig. 1 Standard free energy of formation of selected oxides as a function of temperature[36]

B. Formation of protective scale

The development of oxidation resistance in alloys is based on the addition of an

element, usually chromium, aluminum or silicon, which will oxidize selectively and produce a protective surface oxide[37-39]. Fig. 2 schematic showing the effect of chromium in Fe-Cr alloys on oxidation rate and oxide scale structure based on isothermal oxidation studies at 1000°C [40]. Therefore, the factors which influence the development of the protective oxide and those which can render it non-protective are of prime importance.

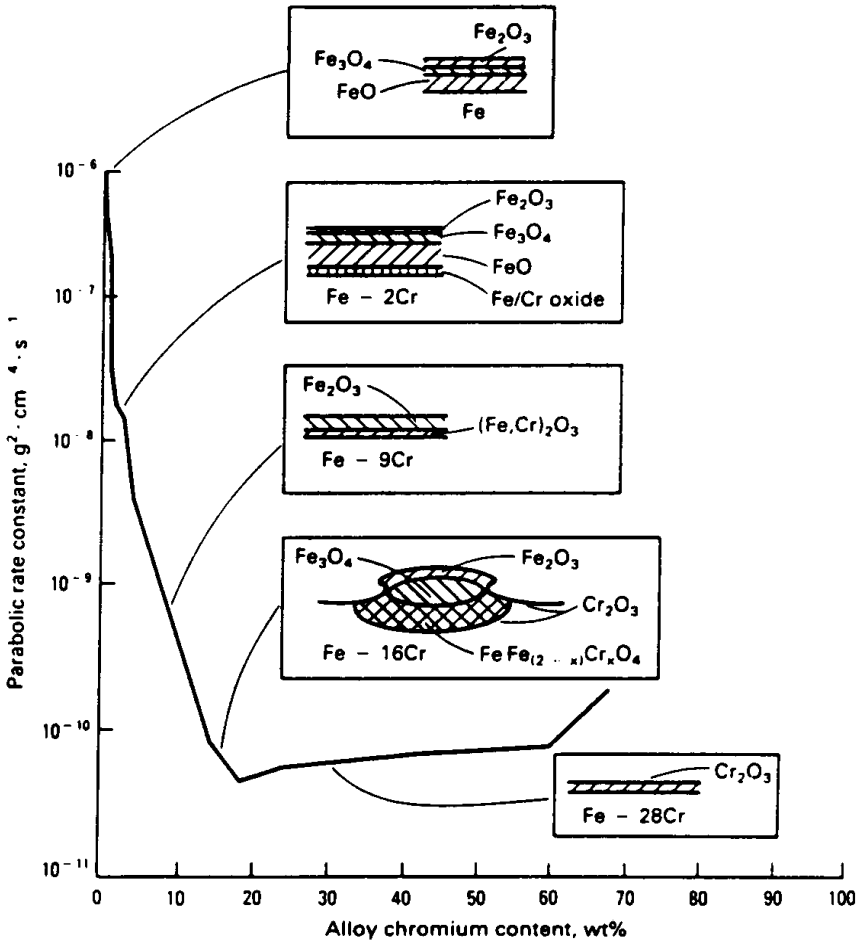

Fig. 2 Schematic showing the effect of chromium in Fe-Cr alloys on oxidation rate and oxide scale structure based on isothermal oxidation studies at 1000°C[40]

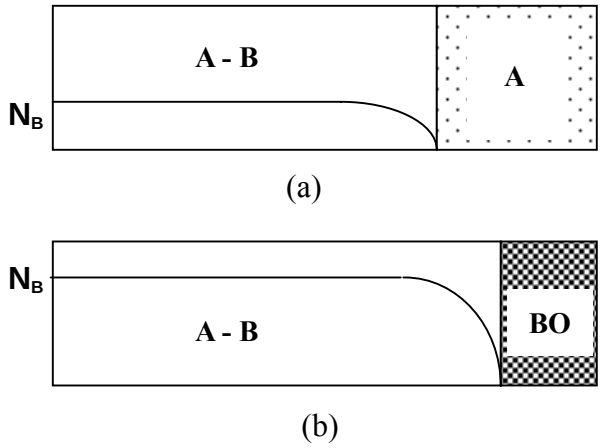

Fig. 3 The effect of solute content on the transition from internal to external oxidation when the oxygen partial pressure is too low to oxidize element A. (a) Schematic diagram of the cross-section and concentration profile for B when NB is less than the critical value showing internal oxidation. (b) Similar schematic diagram for NB greater than the critical value showing continuous external BO formation[41]

The formation of a protective surface scale by selective oxidation of a solute B requires that the oxide of B is more stable than the lowest oxide of the base metal A and that the concentration of the element added is high enough to provide a sufficient flux to the surface for the formation of its oxide as an external layer [41]. Two possibilities for the case where the alloy has a significant oxygen permeability, the oxide of B is much more stable than that of A and the oxygen partial pressure is too low to oxidize A, are illustrated in Fig. 3. Alloys with low solute concentrations allow inward diffusion of oxygen which results in internal oxidation (Fig. 3(a)), while for high solute contents the outward diffusion of solute results in the formation of a continuous external layer of oxide (Fig. 3(b)). The critical solute concentration for the transition from internal to ex-

ternal oxidation has been expressed by Wagner [42] as:

$$N^*_B = [(\pi g^* N_o D_o V_M) / (2 D_B V_{OX})]^{1/2} \quad (9)$$

Here $N_o D_o$ is the oxygen permeability in A, D_B is the solute diffusivity, g^* is a factor determined by the volume fraction of oxide required for the transition, and V_M and V_{OX} are the molar volumes of the alloy and oxide, respectively. The solute content required for external scale formation is seen to increase with the solubility and diffusivity of oxygen and to decrease with an increase in the solute diffusivity in the alloy [43]. However, for most systems of interest, the oxide of the base metal can also form in the ambient atmosphere and grows until the more stable oxide of the solute B becomes continuous and stops the growth of the transient oxide. This situation is illustrated schematically in Fig. 4. The effect of transient oxidation on the transition from internal to external oxidation of B has to be $N_B > N^*_B$[44]. The amount of excess solute required is predicted to increase as the growth rate of the transient oxide increases [45].

Long-term stability of the protective scale requires that the flux of solute to the alloy-scale interface remains large enough to prevent oxides of A from becoming stable[46,47]. The concentration of solute required to maintain the growth of an external scale requires [48]:

$$N_B = V_M / 16 Z_B (\pi k_p / D_B)^{1/2} \quad (10)$$

where k_p is the parabolic rate constant for the growth of the protective seale and Z_B is the valence of B.

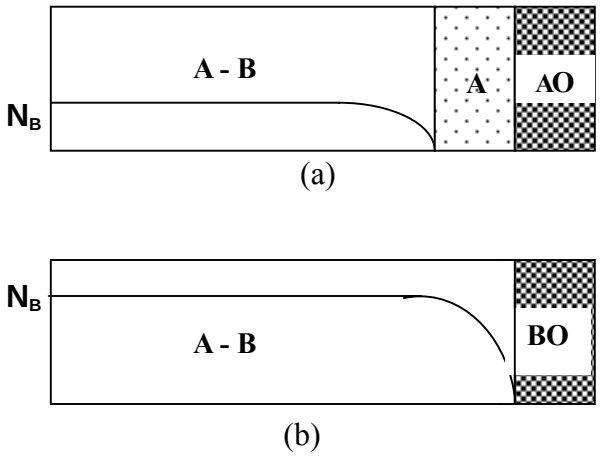

Fig. 4 The effect of solute content on the transition from internal to external oxidation when the oxides of both elements can form. (a) Schematic diagram of the cross-section when N_B is less than the critical value showing internal oxidation of B under an external scale of AO. (b) Schematic diagram of'the cross-section when N_B exceeds the critical value and result in the formation of external BO to the exclusion of AO[41]

C. Effects of temperature

The effect of temperature on the selective oxidation process is determined by the temperature dependence of all of the terms in Eqns. (9) and (10) and that of the growth rate of the transient oxides. The diffusion of solute is increased as temperature increasing, which provides a greater flux to the surface to develop and maintain the protective scale[48,49]. However, this phenomenon is not universal, e.g. TiAl compound develops an external $A1_2O_3$ scale in pure oxygen promoted at low temperature [50,51]. Fig. 5 and Fig. 6 illustrate the oxidation resistance of several austenitic stainless steels as function of temperature[52,53]. General speaking, the metal loss increased with temperature increasing[54-56].

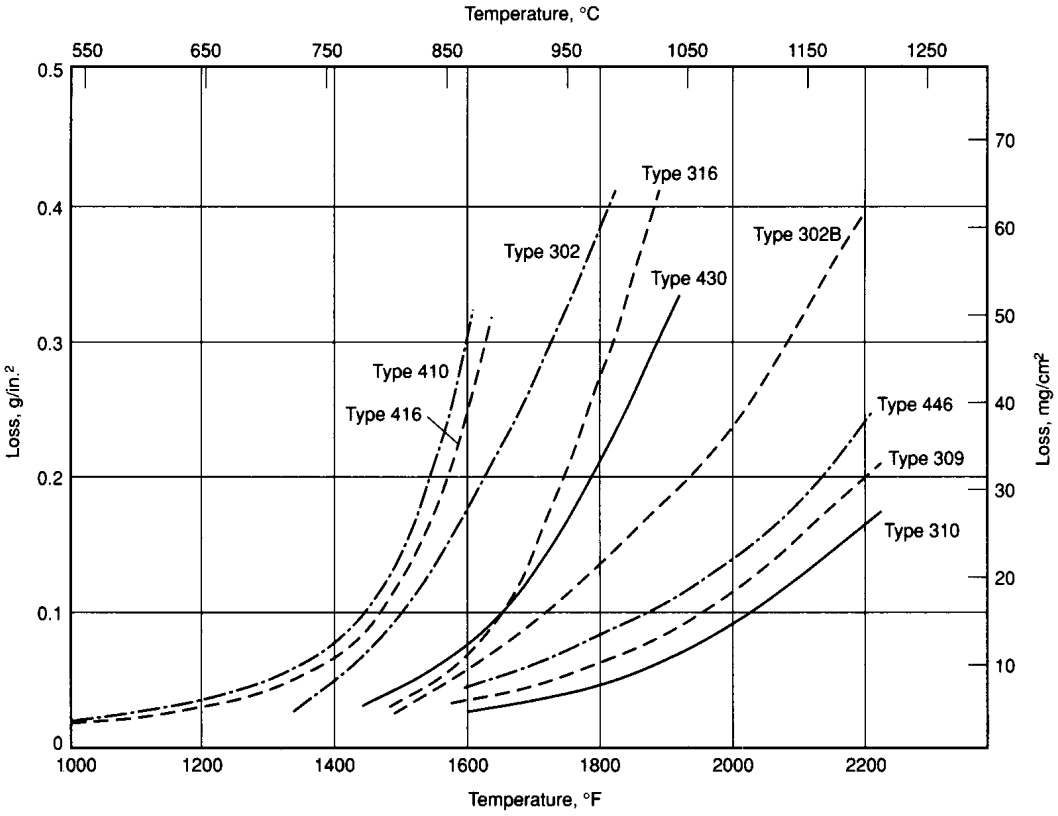

Fig. 5 Oxidation resistance of several stainless steels as a function of temperature [52]

D. Effects of atmosphere compositions

The presence of a second component, such as nitrogen promoting to produce non-protective oxide[12], in the oxidizing gas has been shown to have detrimental effects on the selective oxidation behavior of a number of alloys. CO_2 had a similar effect as carbides formed in Fe-Cr oxidized. Generally, presulfidation[57] or precarburization[58] impair the ability of an alloy to form a protective chromia scale. On the other hand, it is observed that presulfidation of some nickel-base alloys or the presence of carbides in stainless steels and cobalt-base alloys are not deleterious to the oxidation

resistance. The critical factors appear to be the size and distribution of the second-phase particles and the conditions under which they are formed. Coarse particles tend to be detrimental while fine, uniformly dispersed particles can often dissolve rapidly enough to supply the scale-forming element to maintain a protective scale. If the particles are formed under conditions *(i.e.* low activity of carbon, nitrogen, or sulfur) which leave a substantial amount of the scale-forming element free in solution, they are less likely to degrade the oxidation resistance.

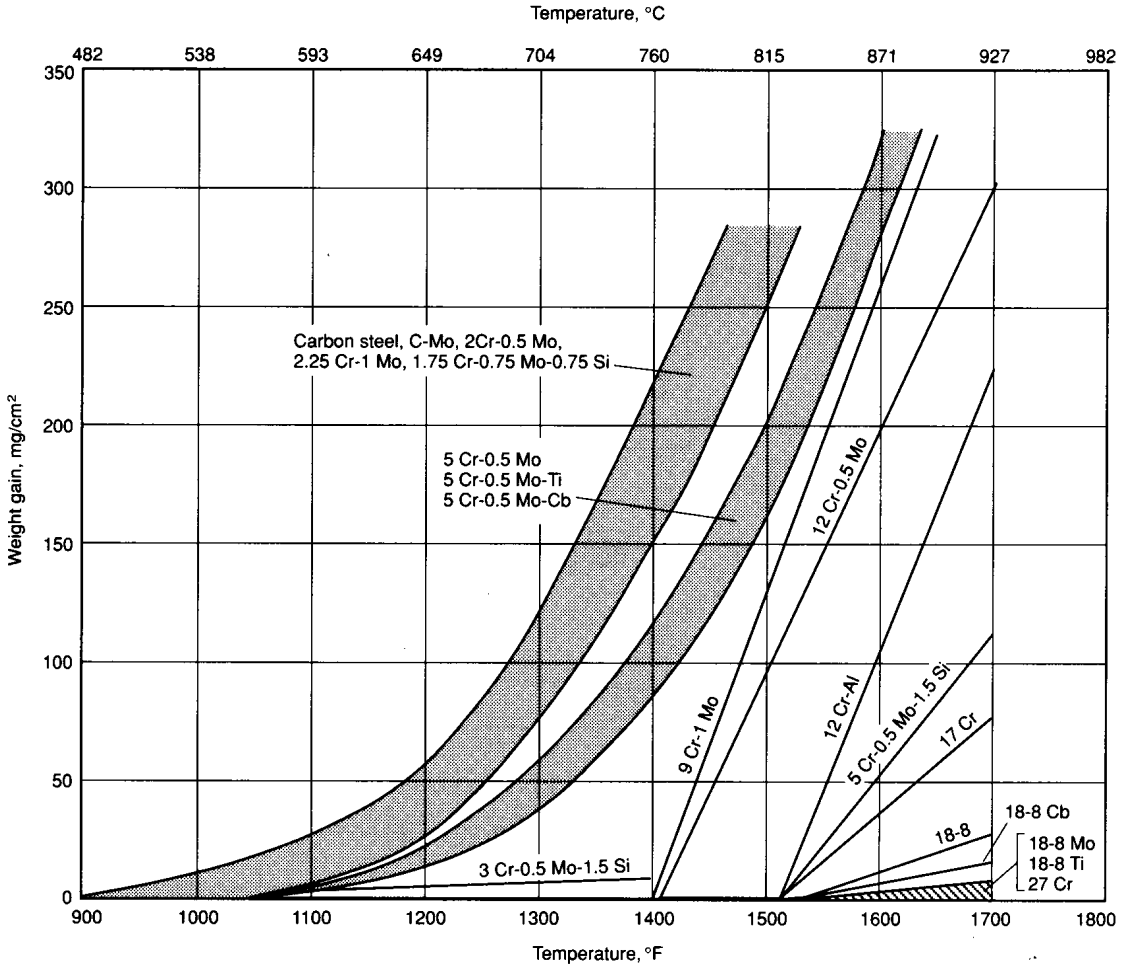

Fig. 6 Oxidation resistance of carbon, low-alloy, and stainless steels in air after 1000hr at temperatures from 590 to 930°C[53]

E. Effects of alloying elements

Nickel and chromium are the two major alloying elements in various heat resistance alloys, whose beneficial effect on oxidation resistance is well known. Silicon and aluminum are also quite effective for resisting oxidation, but they have a harmful effect on the mechanical properties, if not alloyed judiciously. In addition, small amounts of several other alloying elements are added to FeCrNi alloys to achieve specific properties. Alloying chromium reduces the oxygen solubility; that promotes external Al_2O_3 scale formation at substantially lower aluminum content[59,60]. Chromium and vanadium additions to titanium aluminides[61] and titanium and chromium additions to niobium aluminides[62] also promote external Al_2O_3 scale formation at much lower aluminum contents than those required for the binary alloys.

1. Effect of chromium addition

Oxidation of iron can be reduced if addition of some alloying element can eliminate the formation of wustite. This can be achieved when chromium is added as an alloying element to iron. The effect on the oxidation behavior of pure or mild steel when chromium is added to it is shown in Fig. 7[63]. Addition of a small percent of chromium results in the formation of a chromium-rich oxide, along with iron oxides, and with an increase in concentration of chromium, iron chromium spinel are formed and the FeO layer correspondingly becomes thinner relative to Fe_3O_4 as Fe^{+2} ions are blocked by the spinel oxides. With the further increases in Cr, a mixed spinel of type $Fe(Fe, Cr)_2O_4$ is produced which decreases the oxidation rate significantly and leads to parabolic kinetics. Since the Fe ions are more mobile through this layer than Cr^{3+} ions, the

outer layer can still consist of the iron oxide especially after long oxidation times.

When the Cr concentration exceeds the critical concentration N^*_B (~12wt% or more), an initial outer layer of pure chromia is formed. But to sustain the chromia layer over a long exposure time, a substantially larger amount of chromium is required, of about 20 and 25 wt% at 900^{o}C and 1000 ^{o}C, respectively.

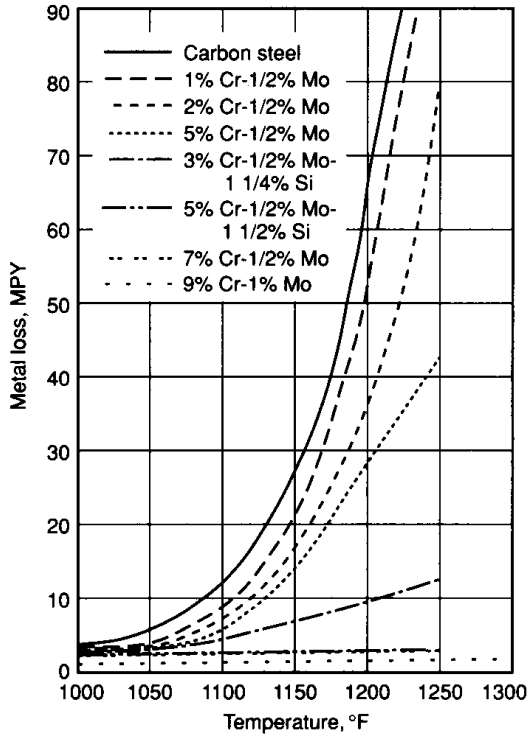

Fig. 7 Effects of chromium and/or silicon on the oxidation resistance of steel in air[63]

2. Effect of nickel addition

Nickel is generally not alloyed with Fe for the purpose of improving high temperature properties of Fe. The main purpose of alloying Ni to Fe-Cr is to transform the Fe from a ferritic to austentitic phase which has an FCC structure and is more stable at high temperatures. Nevertheless, it was seen that addition of Ni to an Fe-11% Cr steel,

results in a significant reduction in the oxidation rate at several temperatures[85,p120]. Thus from the corrosion standpoint, ~20 wt% nickel is effective at 870^{o}C, 30% at 980^{o}C and ~50 wt% at 1200^{o}C. At higher chromium levels, the optimum nickel concentration for maximum air oxidation resistance decreases.

3. Effect of aluminum

The beneficial effect of Al additions to Fe in suppressing its oxidation in air is very strong. For example, ~10 wt% of Al added to Fe decreases the corrosion loss in Fe from > 6 to <2 inches per year. However, mechanical properties of such binary alloys are degraded, making this approach less practical. Under these conditions, a selective alumina scale is formed on the outer surface, protecting the base alloy from further oxidation.

4. Effect of silicon

Silicon additions are beneficial in restricting the oxidation rate. However, when the amount exceeds 2 to 3%, marked embrittlement of the alloy appears. Nevertheless, when used in combination with other beneficial alloying elements, silicon can be quite effective. As shown in Fig. 7, addition of about 1.5% Si to 5Cr-0.5Mo alloy, reduces the oxidation rate substantially.

5. Effect of other alloying elements

Addition of rare earth elements in small concentrations improves not only the oxidation resistance but also enhances the scale adherence and reduces scale spallation. Mn which is generally present in most of the Fe-base alloys, has no pronounced effect on the oxidation rate. In fact a mild detrimental effect on oxidation has been reported

for the 200 and 300 series stainless steels. Mo and V if present in large quantities have a deleterious effect as they can form low melting oxides, MoO_2 and V_2O_5 and can lead to catastrophic oxidation.

The effect of certain tramp elements, such as sulfur, phosphorus, boron etc. has also been found to be detrimental to the scale adherence and its spallation resistance. Hence, where good scale adherence is required, these impurities have to be reduced to very low level (part per million). Boron, however is added to many superalloys for grain boundary strengthening.

F. Breakdown of protective scales

The formation of a protective scale on an alloy by selective oxidation necessarily depletes the scale-forming element from the underlying alloy. The depletion must eventually result in the protective scale becoming unstable[64]. Particularly important among these conditions are temperature cycling, which causes loss of protective scale by spallation, and exposure to mixed oxidants or surface deposits, which can result in the protective scale-forming element being localized in a non-protective morphology. The cause is stress generation arising from thermal expansion mismatch between the scale and alloy (thermal stresses) which may be superposed on stresses generated by scale growth (growth stresses).

G. Kirkendall effect

When two metals with a large difference in their diffusion coefficients interdiffuse, there is a net transport of material across the plane that initially separated them[7,p49]. This phenomenon is known as the Kirkendall effect. Schematic of Kirkendall effect is

shown as Fig. 8. A diffusion couple is made by joining two metals, e.g. Au and Ni, that diffusion occurs across the marked interface. An inert metal such as tungsten can be used as a marker and can be placed in the plane of joining. Such a couple for annealing at a sufficiently high temperature, e.g. 1000^{o}C, or more for a long a change time so that interdiffusion of gold and nickel will occur, resulting in a change in concentration distribution as shown in the figure. However, since $D_{Au} > D_{Ni}$, more gold atoms than nickel atoms will have diffused past the inert markers. Consequently, the inert markers will no longer be at their original positions but will have moved toward the gold end of the specimen. This movement is known as the Kirkendall shift.

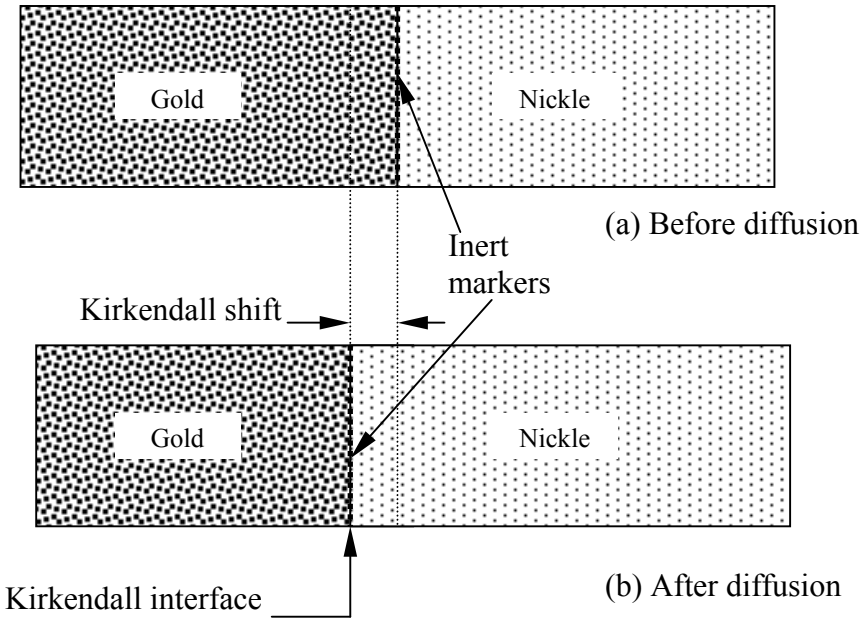

Fig. 8 Schematic of Kirkendall effect[7]

The fact that the flux of gold is greater than of nickel means that a net flux of vacancies occurs across the Kirkendall interface. In the absence of reactions involving the vacancies, this flux of vacancies would lead to large excess of vacancies in one part of the specimens and a deficiency in another part. In fact, vacancies react in various ways to maintain their concentration essentially at an equilibrium value everywhere in the specimen. The simplest reaction, which occurs in regions where the vacancy concentration is above the equilibrium value, is the destruction of vacancies at dislocations, grain boundaries or other discontinuities. The reverse reaction, i.e. the formation of vacancies occurs on these discontinuities, in regions where the vacancy concentration is below the equilibrium value. In case the vacancy concentration is very much above the equilibrium value, i.e. if it is supersaturated, additional reactions such as precipitation of vacancies to form voids within the crystal lattice are quite possible. A region of porosity resulting from this reaction is commonly found on the side of the Kirkendall interface where the vacancies are supersaturated.

CHAPTER III

THE HOT CORROSION OF 310 STAINLESS STEEL WITH PRE-COATED $NaCl/Na_2SO_4$ MIXTURES

A. Introduction

The iron-base austenitic alloy, 310 stainless steel (310SS), is one of the most utilized high-temperature alloy components in industrial engineering plants. Low-grade fuels with high concentrations of sulfur, vanadium, and sodium are often used for firing industrial processes, such as oil- and coal-fired power generation. During combustion, the products, alkali metal sulfates and V_2O_5 vapors, combine with other ash constituents and deposit onto cooler component surfaces, resulting in severe corrosion attack by oxidation, sulfidation, chloridation and even hot corrosion[65]. Aircraft engines and the boilers of off-shore industrial rigs undergo hot corrosion when the sodium chloride from the ocean breeze mixes with Na_2SO_4 from the fuel and deposits on hot-section components, leading to accelerated attack of the alloy substrate. The hot corrosion often increases the corrosion loss of heat-resisting alloys by over a hundred times[5].

Studies of hot corrosion induced by mixtures of $NaCl/Na_2SO_4$ have generally focused on Ni- and Co-base superalloys, and Ni-Cr alloys used in turbine engines or gas turbines[65-68]. The addition of 10wt% NaCl in Na_2SO_4 coatings can easily cause the cracking of protective Cr_2O_3 layers and increase the amount of sulfur incorporated into the substrate, accelerating the corrosion of alloys[68]. It has been reported that the most severe hot corrosion attack is observed on Ni- and Co-base alloys at 900°C in still

air with mixtures of $NaCl/Na_2SO_4$ containing 40wt% NaCl[69]. The 310SS is a good candidate in using in most parts of the waste incinerator. A slow-going chromia scale can be formed with adequate amounts of chromium content, and act as a protective barrier in oxygen-containing atmospheres. The steel's performance in oxidizing environments is well established, but it's behavior in corrosive environments, particularly those containing sulfidizing species and/or chlorides has not been studied extensively. Thus, the high-temperature behavior of 310SS with NaCl and/or Na_2SO_4 deposits at temperatures between the melting point of NaCl or Na_2SO_4 and the eutectic of $NaCl/Na_2SO_4$ is studied. Both kinetics evolution and morphological development are investigated by means of thermal gravimetric analyses, measurements of corrosion attack, metallographic examination, and the identification of the corrosion products. The relationship between the corrosion morphology and composition of deposited salt layers is also explored.

B. Experimental procedure

Commercial cold rolled alloy plates of 310SS were used as experimental materials in this study. The chemical composition of the alloy is Fe -25.57wt%Cr -20.04wt%Ni -1.77wt%Mn -0.58wt%Si -0.02wt%C via ICP (inductively coupled plasma atomic emission spectrometry) analysis. Rectangular specimens were cut to the dimensions of 15×10×2mm by a water-cooled cutting machine. Each specimen to be measured for depth of attack was ground by a precision polishing machine prior to corrosion tests, and the deviation of thickness for each polished specimen was carefully controlled within 5μm.

Specimens for hot corrosion tests were coated with five $NaCl/Na_2SO_4$ mixtures (100/0 wt%, 75/25 wt%, 50/50 wt%, 25/75 wt% and 0/100 wt%, hereafter in wt%) separately until a total coating weight of 2 mg/cm^2 was reached. The salt coating procedures started with weighing (±0.1mg) and measuring (±0.01mm) each specimen, and then heating to 110°C on a hot plate. An air gun was used to spray one of five saturated aqueous salt solutions to produce coat of fine salt particles on the specimen surface after the water evaporated. The process was repeated until the dry salt particles were deposited up to the designed value. Control specimens of 310SS were kept salt free in their as polished condition. Oxidation was performed in static air at 750°C from 1 to 24 hr. In addition, weight change kinetics of alumina plate coated with various deposits of $2mg/cm^2$ salts were also conducted to quantify the evaporation of the various salt deposits at the temperature of our tests.

The depths of corrosion attacks of specimens after tests were measured according to ASTM G54[70]. The terms of "metal loss", "subscale attack", and "total depth of attack" are defined in the specification. During the measurement, nine points were randomly selected from the middle cross-section of the specimens to derive the mean and standard deviation.

The weight change kinetics was measured as a function of time using the spring balance of the thermal gravimetric analyzer (TGA), and the rate of high temperature oxidation was determined. Fig. 9 shows the apparatus schematically. The K value of the spring constant is 2.79 mg/mm, and the precision of measurement is $0.05mg/cm^2$.

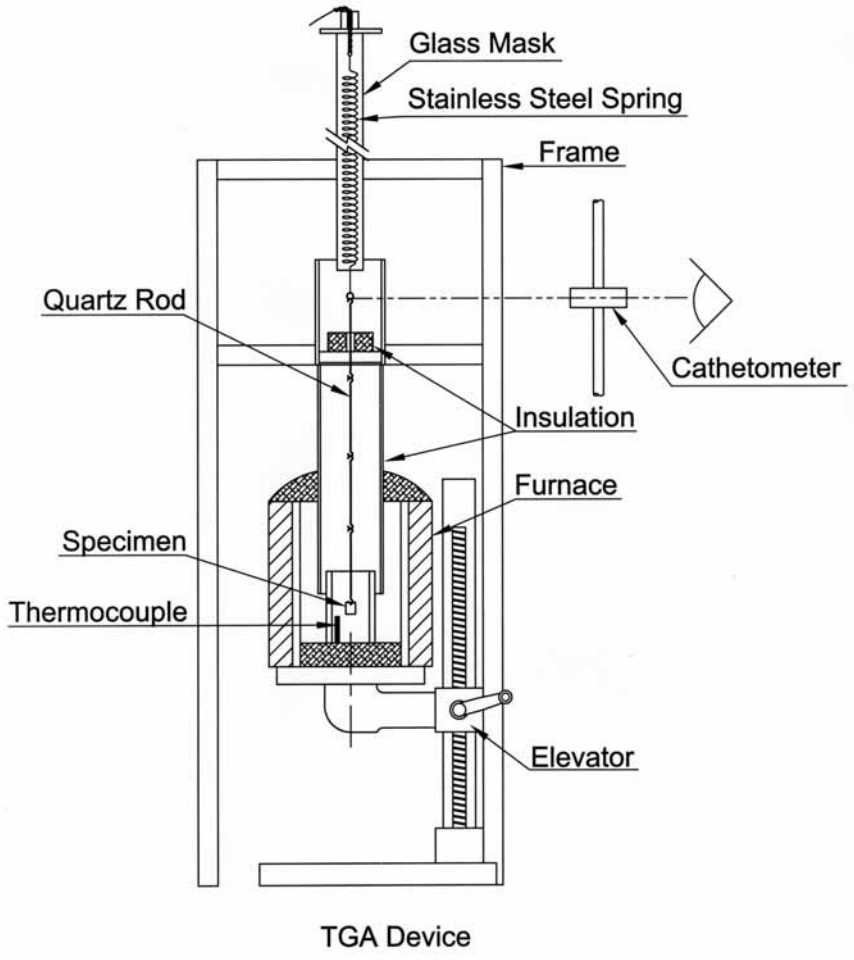

Fig. 9 The schematic representation of the spring balance TGA apparatus

The corrosion products were analyzed by X-ray diffraction (XRD) using mono-chromatic Cu-Kα radiation operated at 40 KV and 100 mA. A sequential grinding technique was adopted to investigate the distribution of the different phases present in the scale and the alloy substrate. XRD data were compared with JCPDS standard files to identify the various phases present. Characterization of the cross-sectional scales was carried out with optical microscopy (OM), scanning electron microscopy (SEM) and

electron probe microanalysis (EPMA) with X-ray wavelength-dispersive spectrometry (WDS).

C. Results

1. Corrosion kinetics

Fig. 10 shows the evaporation weight loss of salt deposits at 750°C. It shows that, qualitatively, NaCl was the main substance evaporated, while a small amount of Na_2SO_4 also evaporated.

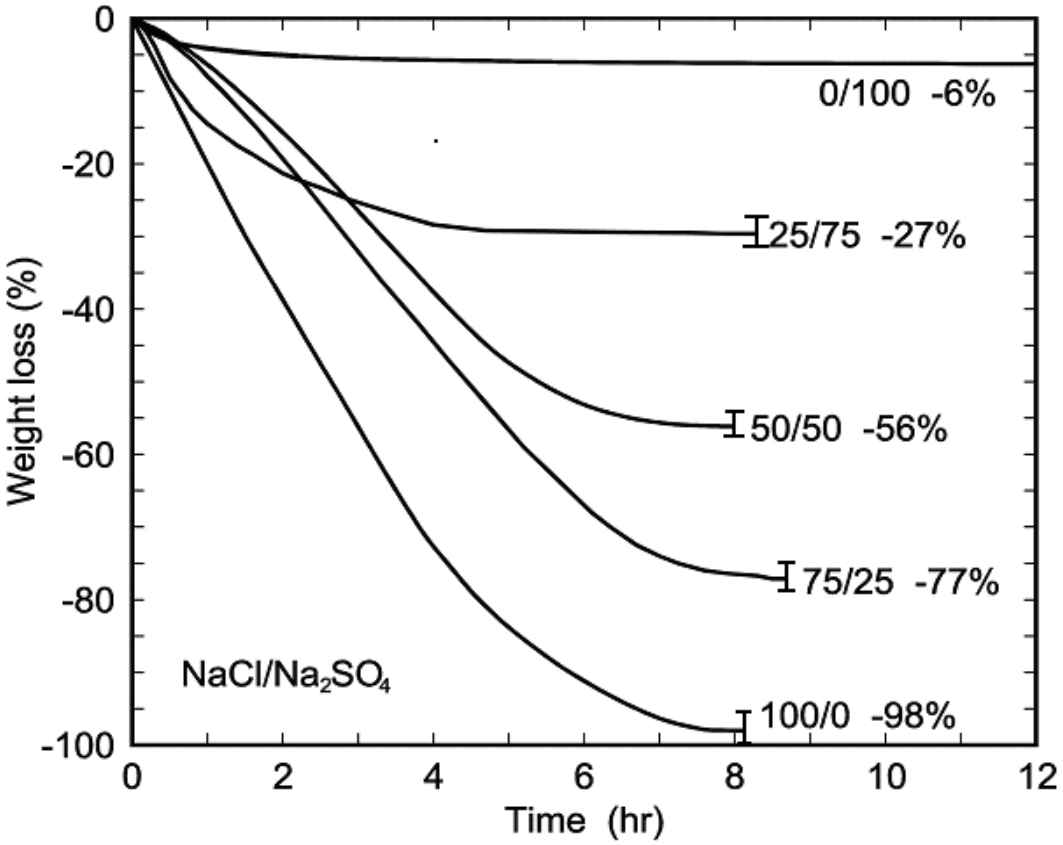

Fig. 10 Evaporation weight loss of salt deposits at 750°C. (The labels are wt% NaCl / wt% Na_2SO_4)

The corrosion kinetics of specimens with and without salt deposits is shown as parabolic plots of weight change versus $t^{1/2}$ in Fig. 11. The figure indicates that the weight gain kinetics in simple oxidation show a steady state parabolic rate law after about 3 h, while the kinetics with salt deposits all display multi-stage weight-gain growth rate involved in the steady state and after breakaway corrosion. The alloy with 75% NaCl mixtures revealed the highest weight change after corrosion for 24 hr, followed by that with 100% NaCl deposit. The calculated parabolic rate constants at different time intervals are summarized in Table 1. The minimum corrosion rate is the steady state growth of scale, it is found that the corrosion rates increase by many orders of magnitude with the addition of NaCl in the salt coatings. The corrosion rate of 100% Na_2SO_4 coating is two orders of magnitude higher than that of simple oxidation.

The depths of attack and weight changes of alloys corroded for 24 hr are shown in Fig. 12. The three depth of attack indices and the corrosion weight changes show consistent results (correlation coefficient, r=0.96), that the corrosion attack increases as the NaCl content increases in mixtures ranging from 25% to 75% NaCl, and alloy coated with 75% NaCl mixture experiences the most severe attack.

2. Morphology and scale constitution

Fig. 13 shows typical cross-sectional micrographs of 310SS after simple oxidation and hot corrosion for 24 hr, indicating that NaCl induces hot corrosion of alloy 310SS and results in the formation of uniform internal attack. The depth of internal attack increases with increasing NaCl content. Compare Fig. 13(a), (b), (c), and (d) to see that intergranular attack is more pronounced as the Na_2SO_4 content in salt mixtures is in-

creased. Contrast with Fig. 13(e) to see that hot corrosion with 100% Na_2SO_4 produces no internal attack in the alloy substrate for 24 hr exposure; an intact Na_2SO_4 layer remains on the specimen surface after XRD detection. No obvious scale could be observed on specimens after simple oxidation by using optical microscope examination. Compare Fig. 13(a), (b), (c), and (d) to see that the quantity of total depth of attack increases with increasing NaCl proportion, all the way to 100%NaCl.

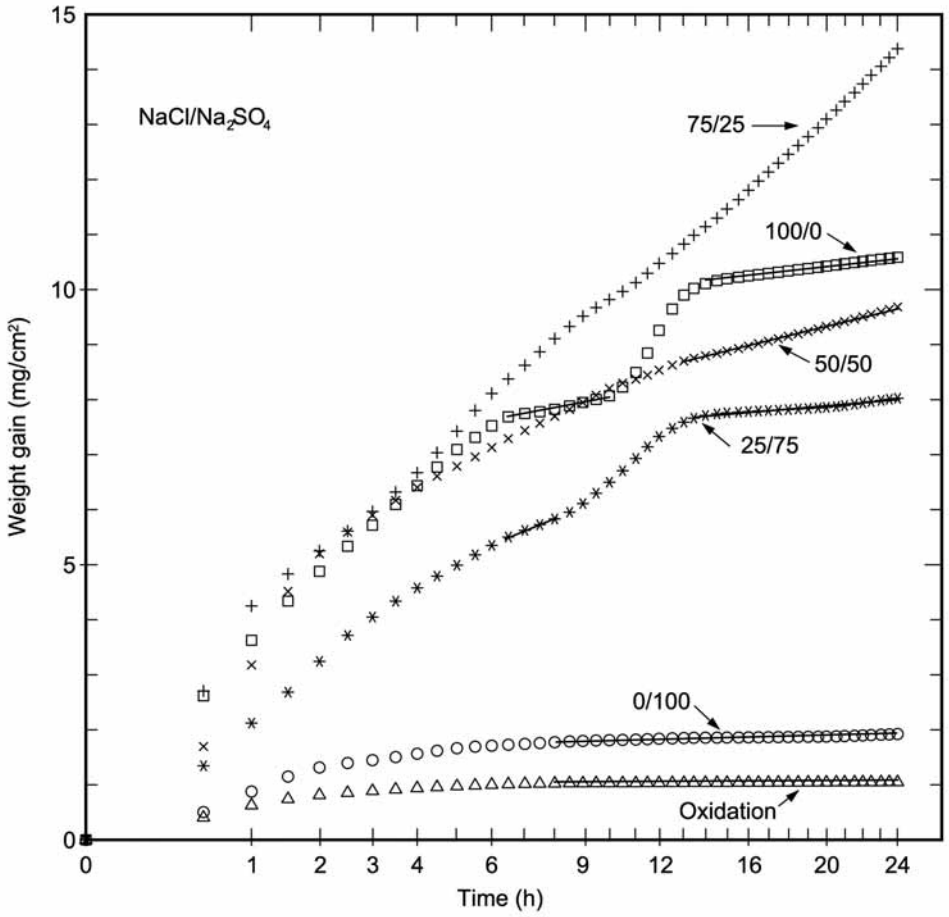

Fig. 11 Corrosion kinetics as a function of square root of time

Table 1 Logarithmic parabolic rate constants (g^2 cm^{-4} s^{-1}) for 310SS oxidized with and without $NaCl/Na_2SO_4$ deposits at 750°C at different time intervals.

Salt composition	K_{p1}	K_{p2}	K_{p3}	K_{p4}
100/0	3.10×10^{-9} [0.5 - 1.5 hr]	1.00×10^{-10} [6.5 - 10 hr]*	7.34×10^{-9} [11 - 13 hr]	4.21×10^{-11} [14 - 24 hr]*
75/25	2.09×10^{-9} [0.5 - 9.5 hr]	1.20×10^{-9} [10 - 11.5 hr]	2.13×10^{-9} [13 - 24 hr]	
50/50	8.55×10^{-9} [0.5 - 1.5 hr]	1.60×10^{-10} [13 - 24 hr]*		
25/75	1.78×10^{-9} [0.5 - 1.5 hr]	3.60×10^{-10} [6.5 - 8 hr]*	1.89×10^{-9} [8.5 - 12.5 hr]	1.91×10^{-11} [13 - 24 hr]*
0/100	4.15×10^{-10} [0.5 - 1.5 hr]	8.87×10^{-13} [8 - 24 hr]*		
Oxidation	2.52×10^{-11} [0.5 - 1.5 hr]	6.42×10^{-15} [8 - 24 hr]*		

* The time interval of lower corrosion rate was observed from the kinetics in Fig. 11.

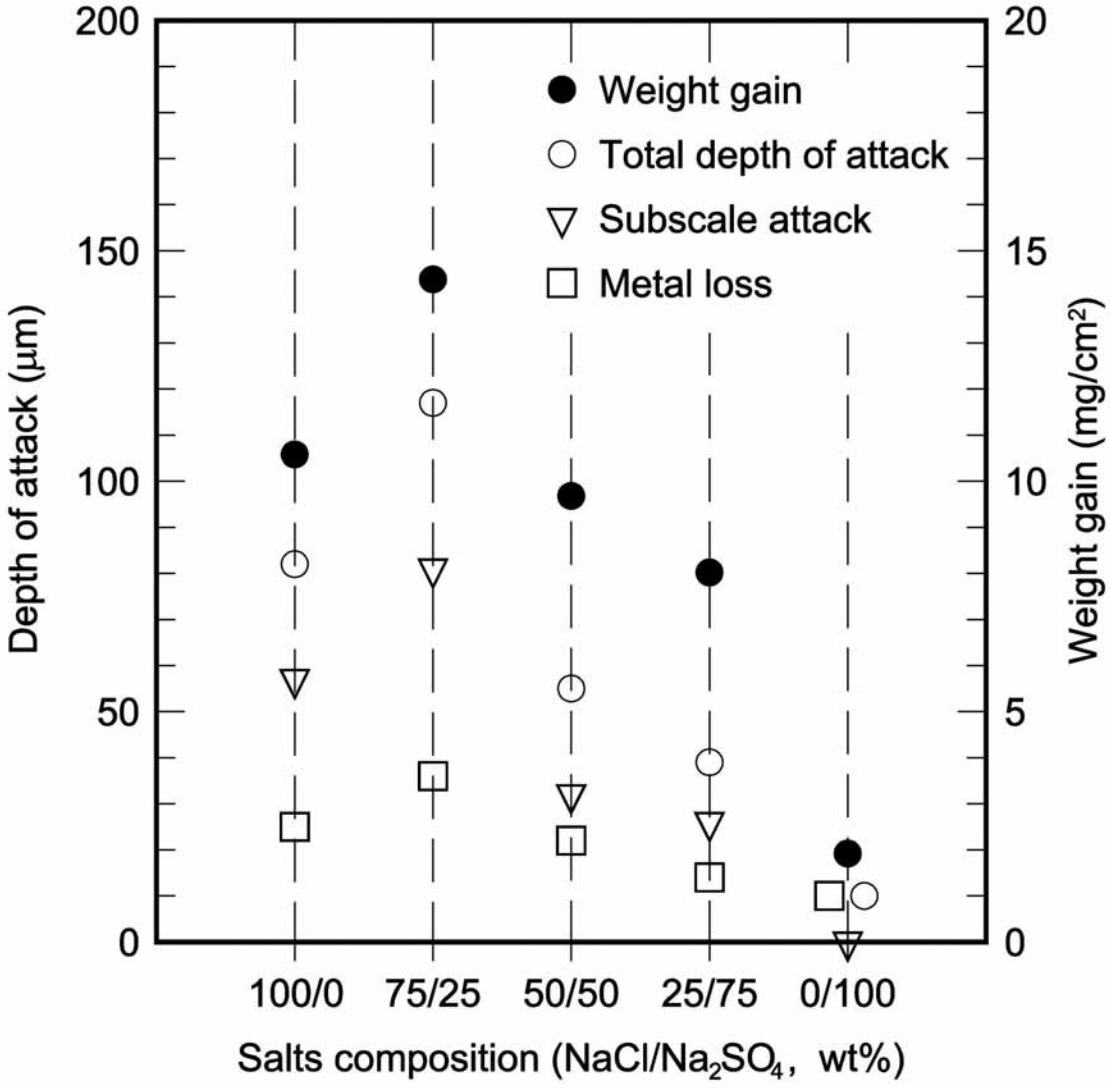

Fig. 12 Corrosion attack and weight gain of 310SS corroded for 24 hr. (correlation coefficient, r=0.96)

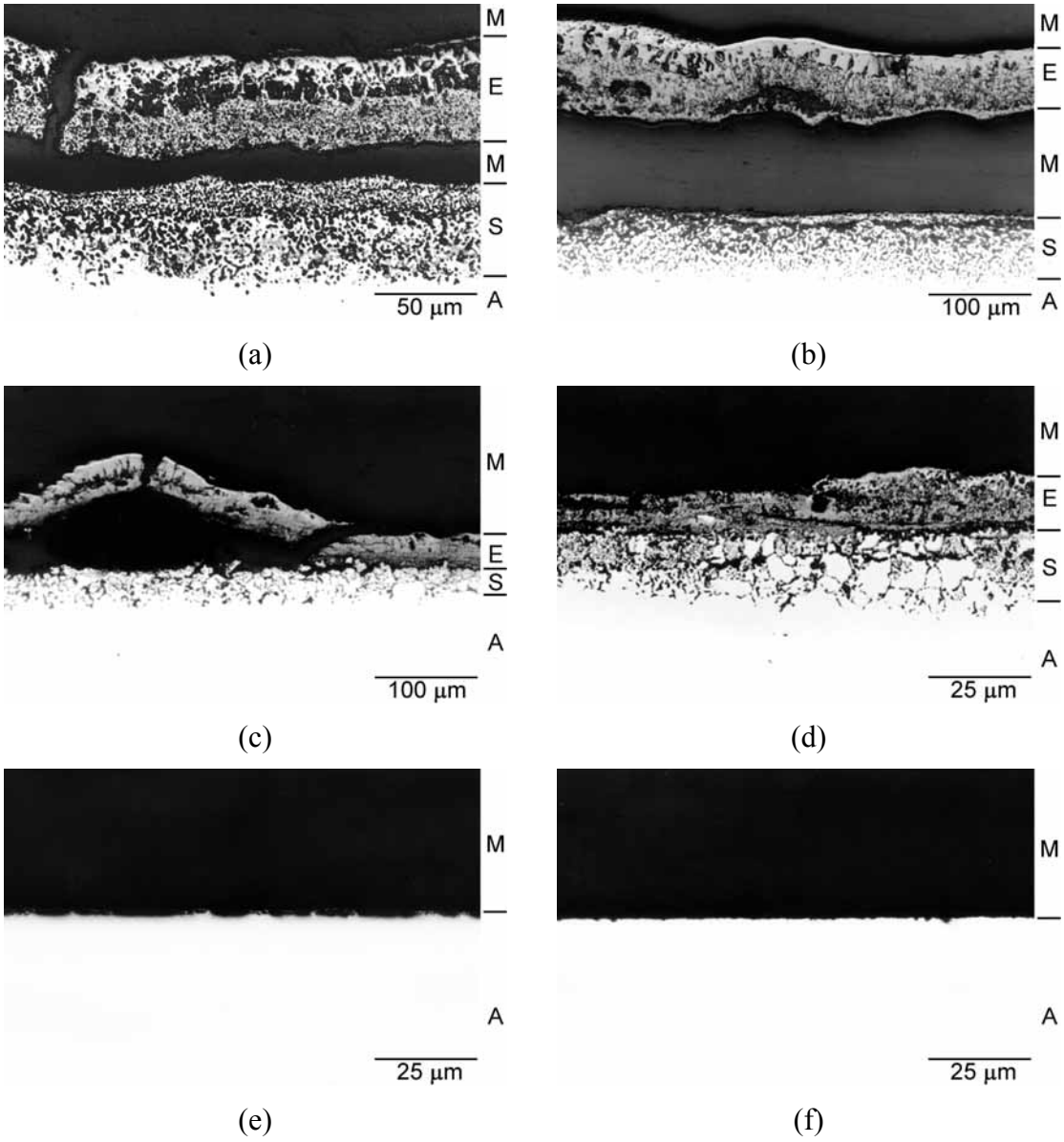

Fig. 13 Optical cross-sectional micrographs of 310SS corroded for 24 hr. (a)pre-coated $NaCl/Na_2SO_4$ mixtures with the ratio of 100/0, (b) 75/25, (c) 50/50, (d) 25/75, (e) 0/100, (f) simple oxidation in air. (Maker M: Mounting material, E: External scale, S: Subscale, A: Alloy.)

The results of EPMA examination of specimens corroded with 75% NaCl mixtures for 1 hr as shown in Fig. 14 is similar to that of specimens corroded with 100% NaCl. The outermost region of the external scale is rich in iron, and chromium is rich on the inner side. Due to the outward migration chemically, as shown in Fig. 14(c), chromium is nearly depleted in the subscale, while nickel is relatively concentrated as shown in Fig. 14(d). Some chlorides can be observed in the inner external scale and in the substrate. Some chlorides, as the big white particles in Fig. 14(f), were deliquesced and sucked out during EPMA examination. There are a little sulfurs reveal in the scale as well as in the subscale.

According to XRD identification, the corrosion products of specimens coated with 100% NaCl after exposure for 24 hr are similar to products with 75% and 50% NaCl mixtures. Typically, Fe_2O_3, $(Fe,Cr)_2O_3$, and Cr_2O_3 are the main corrosion products in the external scale, while minor spinels such as $FeCr_2O_4$ and $NiCr_2O_4$ are detected on the external scale-subscale interface. For the specimens with 75% Na_2SO_4 in the coatings, NiS, FeS, and chromium sulfides could be found as illustrated in Fig. 15. Combining XRD analyses by using sequential grinding technique with EPMA examination reveals elemental redistribution in all hot corrosion environments. Fig. 16 shows a schematic representation of the summary of corrosion products and their relative positions on 310SS after exposure for 24 hr. Metal sulfides become more apparent as Na_2SO_4 content increases to 50% in the salt mixtures.

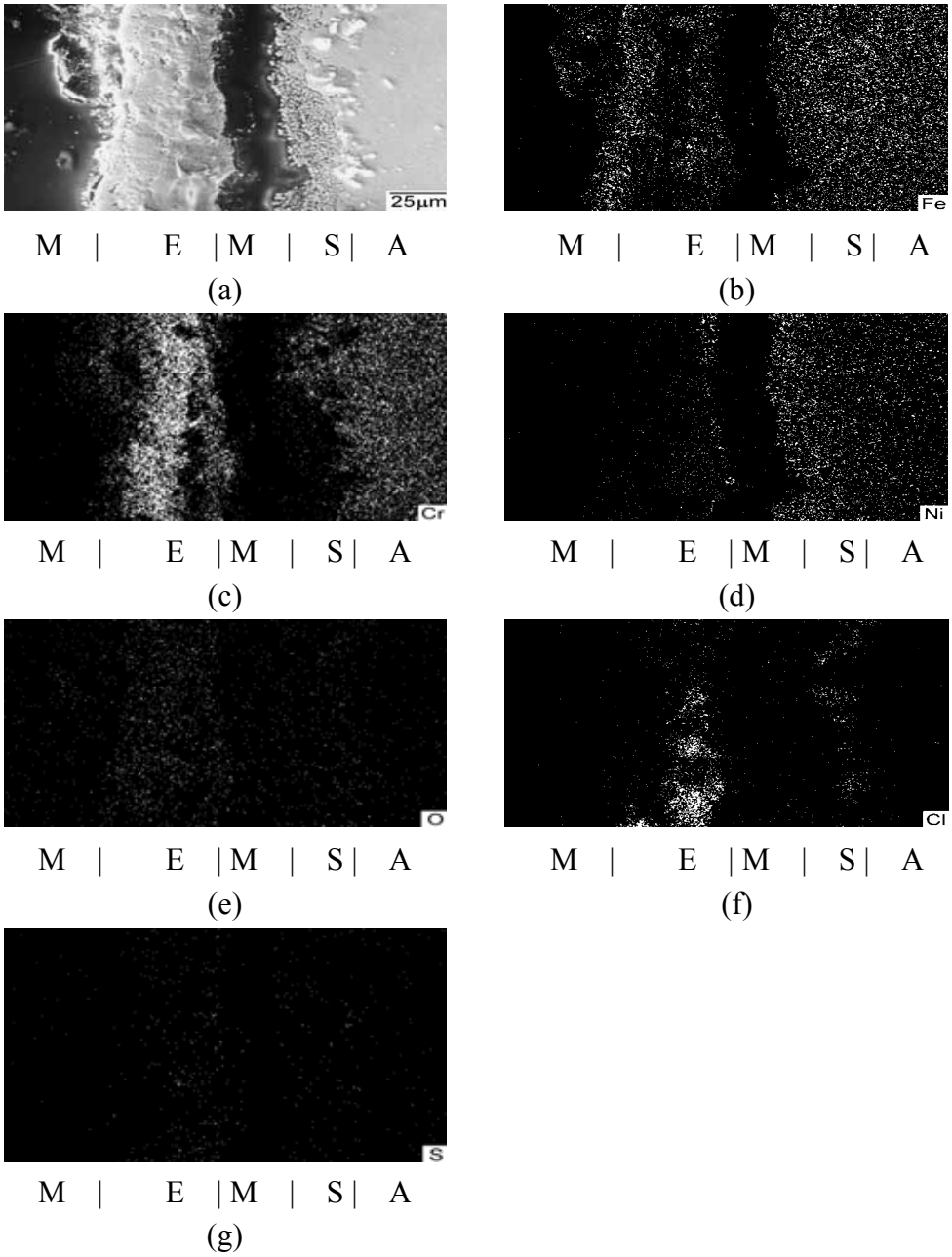

Fig. 14 (a) EPMA cross-sectional micrograph and X-ray maps of (b) Fe, (c) Cr, (d) Ni, (e) O, (f) Cl, (g) S of 310SS with 75% NaCl/25%Na_2SO_4 mixture corroded for 1 hr. (Maker M: Mounting material, E: External scale, S: Subscale, A: Alloy)

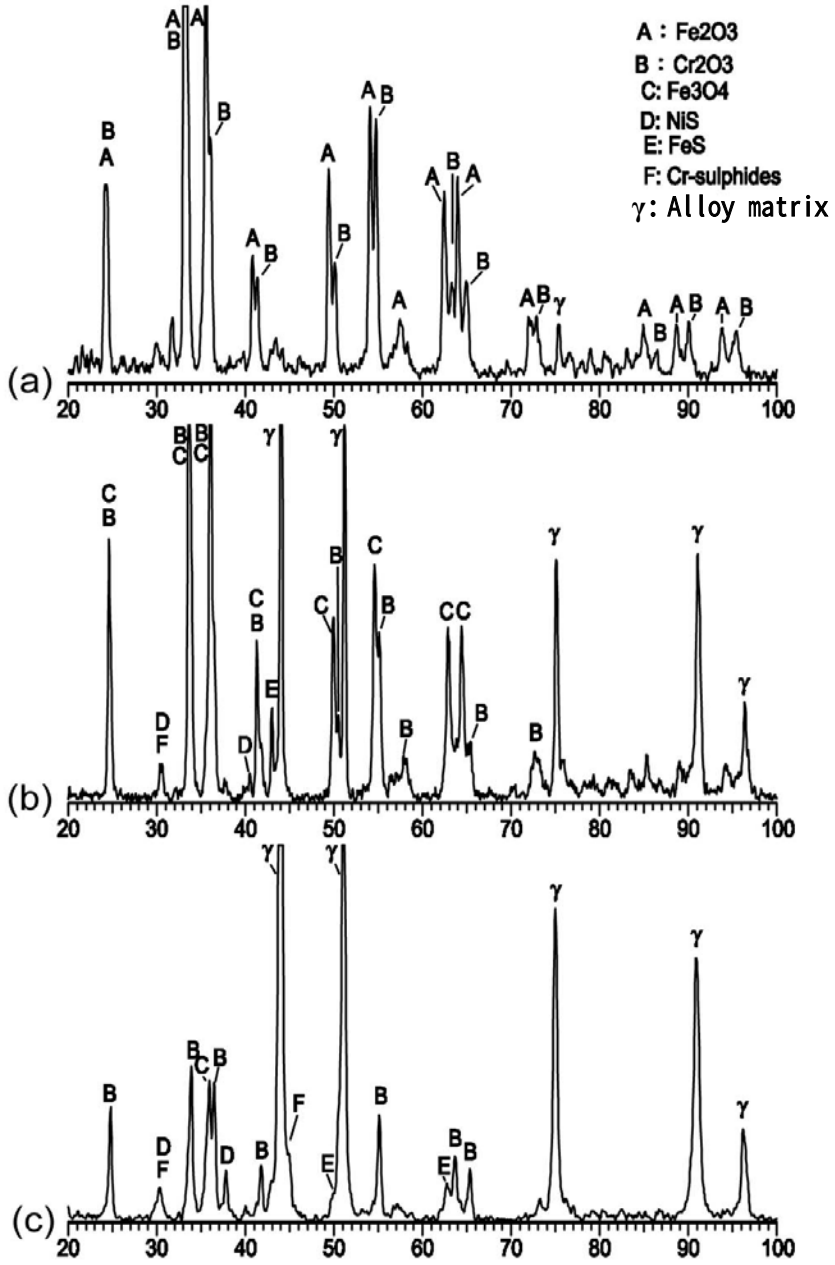

Fig. 15 XRD analyses of corrosion products formed on 310SS with 25%NaCl /75%Na_2SO_4 deposits exposed at 750°C for 24 hr detecting from (a) outer side of external scale, (b) inner side of external scale, (c) alloy substrate after light brushing of the external scale

100%NaCl

External scale									
Substrate Alloy matrix									
Phase	Fe_2O_3	$(Fe,Cr)_2O_3$	Fe_3O_4	Cr_2O_3	$FeCr_2O_4$	$NiCr_2O_4$			
Intensity	strong	middle	weak	strong	weak	possible			

75%NaCl / 25%Na_2SO_4

External scale									
Substrate Alloy matrix									
Phase	Fe_2O_3	$(Fe,Cr)_2O_3$	Fe_3O_4	Cr_2O_3	$FeCr_2O_4$	$NiCr_2O_4$			
Intensity	strong	middle	weak	strong	weak	weak			

50%NaCl / 50%Na_2SO_4

External scale									
Substrate Alloy matrix									
Phase	Fe_2O_3	$(Fe,Cr)_2O_3$	Fe_3O_4	Cr_2O_3	$FeCr_2O_4$	$NiCr_2O_4$	NiS	Cr_2S_3	
Intensity	strong	weak	weak	strong	weak	weak	possible	possible	

25%NaCl / 75%Na_2SO_4

External scale									
Substrate Alloy matrix									
Phase	Fe_2O_3	$(Fe,Cr)_2O_3$	Fe_3O_4	Cr_2O_3	$FeCr_2O_4$	$NiCr_2O_4$	NiS	$Fe_{1-x}S$	Cr_3S_4/Cr_2S_3
Intensity	strong	weak	weak	strong	weak	weak	weak	weak	weak

100%Na_2SO_4

External scale									
Substrate Alloy matrix									
Phase	Fe_2O_3	$(Fe,Cr)_2O_3$	Fe_3O_4	Cr_2O_3	$FeCr_2O_4$	$NiCr_2S_4$	NiS	$Fe_{1-x}S$	Cr_3S_4/Cr_2S_3
Intensity	strong	weak	(none)	strong	weak	weak	weak	weak	weak

Fig. 16 XRD analyses of 310SS corroded with different salts

D. Discussions

1. Hot corrosion with 100%NaCl

It is widely agreed that the hot corrosion loss of materials will be more severe when the temperature is higher than the melting point of deposits. Although the testing temperature in this study is lower than the melting point of NaCl (801°C), according to Table 1, the corrosion rate is at least four orders of magnitude higher than that of simple oxidation.

As can be seen in Fig. 13(a), the corrosion morphology shows the typical uniform subscale attack induced by NaCl as reported[71-73]. These imply that NaCl coating plays an important role in hot corrosion behavior, even at temperatures lower than 801°C. Hot corrosion requires a molten salt to be in contact with the specimen. If there are no molten phases, the corrosion rate will be low. It is possible that a molten phase is formed for the 100% NaCl salt. Many researchers have pointed out that the formation of sodium chromate, Na_2CrO_4, could result from oxychloridation in which chromium or chromium oxide reacts with NaCl and oxygen even when the temperature is lower than the melting point of NaCl[74-76]. As the Na_2CrO_4 is formed, the salt will wet the specimen surface due to the low-melting-eutectic NaCl-Na_2CrO_4 (577°C) as shown in Fig. 17 and lead to a mechanism of hot corrosion dominated by molten salt[77].

Oxychloridation, in which NaCl reacts with metal and the oxygen dissolved in molten salts to form metal oxides, sodium-containing oxides, and chlorine[74], is believed to be the initial reaction of NaCl-induced hot corrosion. There are three paths that chlorine may take toward further reaction in this study: (1)escape to atmosphere; (2)

dissolve into Cr_2O_3 lattice increasing the content of cation vacancies and accelerating the oxidation of alloy[66]; (3)react with the alloy substrate to form metal chlorides, which would be the catalyzing intermediate compounds of cyclic chloridation/oxidation reactions[76].

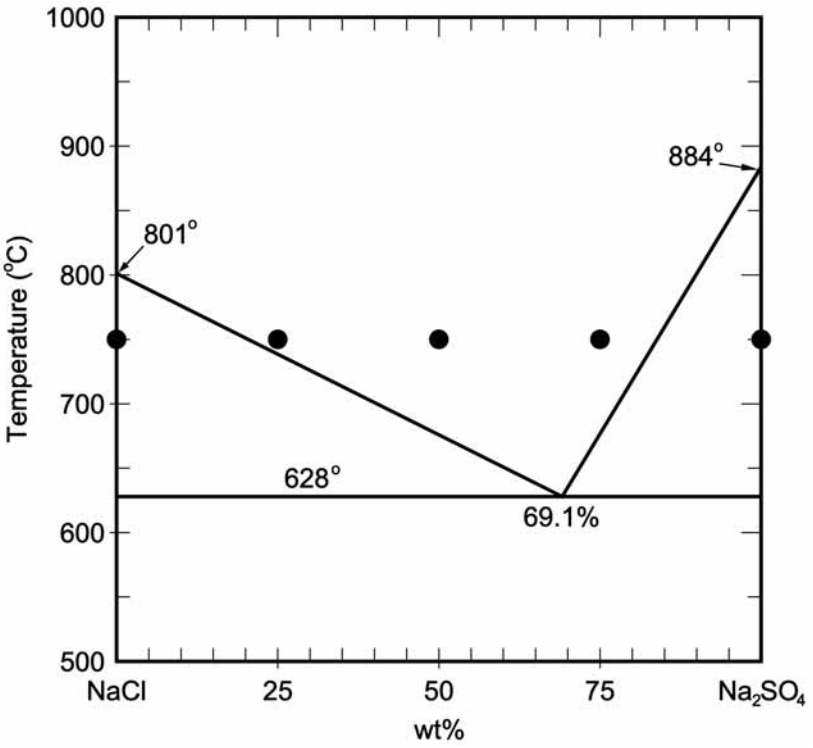

Fig. 17 The hypothetical phase diagram of the NaCl-Na_2SO_4 system[77]. Bullets stand for at experiment temperature 750°C with NaCl/Na_2SO_4 compositions

According to thermodynamics data[78], chromium has the greatest driving force to react with chlorine to form chloride, and nickel, with noble characteristics, has the least tendency to react with chlorine and will be left in the alloy substrate. The selective chloridation of chromium and iron in the initial stage leads to the outward migration

of these elements and the formation of voids in the alloy substrate, resulting in molten salts filling in voids by capillary action. In addition, iron and chromium can dissolve into the molten salt and volatilize or react with oxygen[71,72]. The chloridation products, metal chlorides, or metal ions dissolved in molten salt then evaporate or diffuse outward and react with oxygen to form non-protective duplex-layer scales, in which porous Cr_2O_3 scale is formed in the inner layer, while iron oxide is revealed on the outer side as can be seen in Fig. 14. This selective leaching of chromium and iron cause void formation and the molten salt fills in the voids, leading to the formation of a uniform interconnecting void-oxide network in the alloy substrate as shown in Fig. 13(a).

The accelerated oxidation or cyclic chloridation/oxidation reaction in hot corrosion behavior of 310SS is further presented by the breakaway kinetics as can be seen in Fig. 11. The fast growth of oxides indicates the breakaway of the external scale. The cracking of the external scale provides the path for the trapped-chlorine or chlorides formed in the initial stage to escape to the atmosphere. If this mechanism is occurring, it reduces the total amounts of chlorine in the subscale and further slows the accelerated oxidation of alloy. This interpretation is supported by our observation that $K_{p2} > K_{p4}$ in Table 1. This fact that corrosion rate slows down suggests that the external scale has healed.

2. Hot corrosion by 100%Na_2SO_4

The melting point of Na_2SO_4 is 884°C, which is much higher than the test temperature in this study. According to Fig. 10, Na_2SO_4 coating still remains on the specimen surface. These facts imply the hot corrosion caused by the fluxing of Na_2SO_4

could be neglected. Buscaglia et al.[79] have studied the hot corrosion behavior of pure iron with Na_2SO_4 coating oxidized at temperatures lower than the melting point of Na_2SO_4 by means of thermodynamics demonstration and morphological examination. The results indicated that the deposited sulfate particles will be incorporated into the oxides matrix for long-term reaction, and the salt decomposition will occur when the partial pressure of oxygen in the environment is locally lower than that in equilibrium with the Na_2O/Na_2SO_4. This suggests a hypothesis: the decomposition process will constitute a sulfur source for formation of trace amounts of chromium-, nickel-, and iron-sulfides directly in the scale, as indicated in Fig. 15 and Fig. 16.

It is known that solid-state diffusion of metal ions through its sulfide is faster than that through its oxide[77]. As can be seen in Table 1, the corrosion rate of the Na_2SO_4-induced hot corrosion is two orders of magnitude higher than that of simple oxidation. This is consistent with my hypothesis of fast migration through the metal sulfides formed in the scale-substrate interface. Nevertheless, the negligible attack and the lack of breakaway kinetics of 310SS coated with 100% Na_2SO_4 as shown in Figs. 3 and 5e indicate that alloy did not suffer intergranular corrosion during the 24 hour test period.

By comparing the corrosion rates tabulated in Table 1, the corrosion rate of 100% Na_2SO_4 coating is many orders of magnitude lower than that of 100% NaCl and its mixtures, revealing that the Na_2SO_4 is not as detrimental as NaCl to the corrosion resistance of 310SS during steady state exposure at 750°C for 24 hr.

3. Hot corrosion by $NaCl/Na_2SO_4$ mixtures

The phase diagram of the $NaCl/Na_2SO_4$ system is shown in Fig. 17[80]. The mixtures with compositions of 75%, 50% and 25% NaCl were all completely melted at 750°C, indicating that Na_2SO_4 acidic- and basic-fluxing mechanism which would induce accelerated oxidation of alloys possibly takes place. Johnson et al.[69] pointed out that the presence of NaCl in the mixtures of $NaCl/Na_2SO_4$ can initiate attack in high chromium content alloys. The addition of 10% NaCl in Na_2SO_4 coatings can easily cause the cracking of protective Cr_2O_3 layers and increase the amount of sulfur incorporated into the substrate, accelerating the corrosion of alloys. Hence, as shown in Fig. 11, the kinetics of hot corrosion with $NaCl/Na_2SO_4$ mixtures containing 25% NaCl or more show unstable weight change growth rate and much more severe hot corrosion than is observed with simple oxidation or with 100% Na_2SO_4.

Competition between chloridation, sulfidation and oxidation reactions in the initial stages of our corrosion tests eventually lead to one of the reactions dominating. Even if the oxidation reaction occurs first, NaCl appears to cause cracking of oxide scales at a later stage followed by penetration toward the substrate and reaction with metals to form metal chlorides. In a mixed salt environment, sulfur was incorporated into scale and proceeded to a sulfide formation the alloy substrate.

Therefore, as the formation of protective oxide scale was inhibited by the presence of NaCl, chlorides and sulfides tend to form in the alloy substrate as indicated in Fig. 14(f) and Fig. 14(g), leading to the propagation of hot corrosion. Meanwhile, as shown in Fig. 13(a-d), NaCl was responsible for the subscale attack of 310SS, the depth of in-

ternal attack increased with increasing NaCl content in salt mixtures.

Although the salt mixtures exist in a completely liquid phase at 750°C, the fast evaporation characteristics of NaCl led to a residue of solid Na_2SO_4 on the specimen surface, as shown in Fig. 10 and Fig. 17. The mixtures of 75% NaCl contained the most NaCl and low-melting-eutectic NaCl/Na_2SO_4 action time on the alloy is the longest, resulting in generating the highest rate of corrosion. Thus, the fact that mixtures with 75% NaCl showed the most severe corrosion of all, is consistent with my hypothesis of molten eutectic salt and capillary transport.

With respect to the high volatility of chlorides, Fe-, Ni-, and Cr-sulfides would remain in the alloy substrate once they were formed. Nevertheless, sulfides have more crystal defects and higher free energy than metal oxides[81]. The crystal defects in sulfides would promote ion diffusion and the sulfides could be oxidized into oxides as the partial pressure of oxygen increases. In the field of corrosion morphology, research reports indicate that in a low sulfur partial pressure, low-temperature sulfidation environment, or a Na_2SO_4-containing environment with high oxygen potential[82], the alloys will usually be attacked along grain boundaries. My data, as shown in Fig. 13 and 8, are consistent with this view. In my experiments, feature of intergranular attack is more pronounced and metal sulfides become more apparent as the content of Na_2SO_4 in the mixtures is increased.

E. Summary of 310SS hot corrosion with NaCl/Na_2SO_4

1. NaCl is the main corrosion catalytic specie in high-temperature corrosion involving mixtures of NaCl/Na_2SO_4. The presence of NaCl in deposits inhibits the formation

of protective oxide scale in the initial stage, leading to the propagation of hot corrosion of 310SS. This is supported by our observation that depth of internal attack increased with increasing NaCl content in salt mixtures.

2. The mixtures of 75% NaCl contained the most NaCl and low-melting-eutectic $NaCl/Na_2SO_4$ action time on the alloy is the longest, resulting in generating the highest rate of corrosion. The fact that mixtures with 75% NaCl showed the most severe corrosion of all, is consistent with my hypothesis of molten eutectic salt and capillary transport.
3. Fe_2O_3, $(Fe,Cr)_2O_3$, and Cr_2O_3 are main corrosion products in the external scale. Minor spinels such as $FeCr_2O_4$ and $NiCr_2O_4$ are formed on the external scale-subscale interface. Sulfides such as NiS, FeS, and chromium sulfides are found with increasing Na_2SO_4 content in the coating layer.
4. The hot corrosion morphology of the alloy induced by 100% NaCl coating shows a typical uniform internal attack, while the feature of intergranular attack is more pronounced as the content of Na_2SO_4 in the mixtures is increased.
5. The corrosion caused by 100% Na_2SO_4 coating shows incubation period characteristics. The corrosion rate of 100% Na_2SO_4 coating is many orders of magnitude lower than that of 100% NaCl and its mixtures over the 24 hour period of exposure in this report. We conclude that the Na_2SO_4 is not as detrimental as NaCl to the corrosion resistance of 310SS during exposure at 750°C for 24 hr.

CHAPTER IV

THE EFFECT OF NaCl DEPOSIT AND THERMAL CYCLE ON AN ALUMINIDE LAYER COATED ON 310 STAINLESS STEEL

A. Introduction

The low-grade fuel with sulfur, alkali salts, or vanadium are mainly used for firing in industrial processes, such as gas turbine, oil- and coal-fired power generation, and the boilers of off-shore industrial rigs. Hot corrosion occurs when the sodium chloride from the ocean breeze mixes with Na_2SO_4 from the combustion process and deposits on metallic hot-section components, leading to severe attack of the alloy substrate. The hot corrosion is commonly accompanied by the formation of a porous and non-protective oxide scale, which has been mostly attributed to the condensation of salts that attacks the protective oxide scale[83,84].

Materials for high temperature service need excellent mechanical properties, including high temperature strength, good creep resistance, microstructure stability, and strong corrosion resistance is required. These requirements sometimes cannot be achieved by alloy development alone. An alternative approach, which mechanical strength is accomplished by alloy development and corrosion resistance by surface coating or surface treatment is often used[7]. Al_2O_3 and Cr_2O_3 are known as the most effective oxide scale forming surface treatments used to prevent accelerated oxidation of alloys at high temperature. Several studies report that Al_2O_3-forming alloys show better corrosion resistance than Cr_2O_3-forming alloys in chlorine-containing environments

including Cl_2-Ar, Cl_2-O_2-Ar, HCl-O_2 and NaCl[8-12]. Due to the superior high temperature corrosion resistance of Al_2O_3-forming alloys and FeAl intermetallics[12], aluminum coated on alloys surface are often chosen for industrial process. Aluminum coating processes such as hot dipping, thermal spray, pack cementation, slurry, cladding, electroplating, etc., are the most common methods used for iron base materials[13]. In the selection of aluminum coating process, critical issues include size and shape of workpiece, thickness of coating required, accuracy, cost, and the available work places are considered.

On the basis of cost and feasibility, hot-dip aluminizing (HDA) process is the most common surface treatment for alloys. Previous studies[11,14] pointed out that alloys with hot-dip aluminum coating reveal excellent corrosion resistance. A thin, slow-going alumina scale acts as a corrosion barrier and allows long term exposure at high temperature. However, the dependability of hot-dip aluminum alloy against chloride-induced degradation is seldom investigated. The purpose of this study was to investigate the effects of hot-dip aluminum with added 7%silicon against NaCl-induced accelerated oxidation in a thermal cycling environment.

B. Experimental procedure

Commercial cold rolled alloy plates of AISI 310SS were used as experimental materials in this study. The chemical composition of the alloy is Fe-25.57%Cr-20.04%Ni-1.77%Mn -0.58%Si-0.02%C (wt.%) via ICP (inductively coupled plasma atomic emission spectrometry) analysis. Rectangular specimens were cut to the dimensions of 15×10×2mm by a water-cooled cutting machine. Specimens for

further hot-dip treatment were hung by stainless steel wires and coated with uniform weld flux. Specimens were dried and immersed in a 700°C aluminum-silicon (Al-7%Si-0.3%Mg-0.2%Fe-0.2%Cu in wt.%) molten bath for 16 seconds. The up and down speed was 18cm/min. The hot-dipped specimens were cleaned by a mixed aqueous solution of nitric acid, phosphoric acid, and water in 1:1:1 volume fraction at 60°C. Thickness of the external aluminum coating and aluminized layer was approximately of 25μm after hot-dip treatment.

Prior to thermal cycling test, specimens with and without hot-dip treatment (uncoated 310) were deposited with NaCl until a total depositing weight of 2 mg/cm^2 was reached. The salt depositing procedures started with weighing (±0.1mg) and measuring (±0.01mm) each specimen, and then heating to 110°C on a hot plate. An air gun was used to spray saturated aqueous-salt solutions to produce coat of fine salt particles on the specimen surface after the water evaporated. The process was repeated until the dry salt particles were deposited up to the designed value. The cyclic depositing-heating test was performed. Specimens with an NaCl deposit were exposed in a furnace with static air at 850°C for 20 hr and then air-cooled. After cooling to room temperature, corroded specimens were re-sprayed with NaCl and heated to an elevated temperature. The cyclic heat pattern was repeated a maximum of 10 times. In order to compare the effect of deposited salt and thermal stress on the coated and uncoated 310 alloy, control specimens with no salt deposit were employed in thermal-cycling tests. The depths of corrosion attacks after test were measured according to ASTM G54[70].

A sequential grinding technique was adopted to investigate the distribution of the

different phases present in the scale and the alloy substrate. The corrosion products were analyzed by X-ray diffraction (XRD) using monochromatic Cu-Kα radiation operated at 40 KV and 100 mA. Characterization of the cross-sectional scales was carried out with optical microscopy (OM), scanning electron microscopy (SEM) and electron probe microanalysis (EPMA) with X-ray wavelength-dispersive spectrometry (WDS).

C. Results

1. Corrosion of 310 without HDA treatment

After corrosion at 850°C for the first cycle, a black scale about 5μm is formed on the alloy surface, and it cracks and peels off during air-cooling. Light brown with some green products can be observed at the alloy substrate side of the scale/substrate interface. EDS analysis reveals that the light brown species consist of mainly SiO_2, while the green product consists primarily of Cr_2O_3. The corrosion morphologies remain stable through each cycle up to the eighth cycle of test. After the ninth cycle, corrosion scale penetrates the entire 2mm thickness of specimen.

Fig. 18 shows the cross-sectional micrographs of alloy tested for four and ten cycles. It can be seen that scales spall severely and interconnecting void networks appear in the subscale. The quantitative analyses of the EPMA in the bulk alloy substrate after cyclic tests are shown in Table 2. In the second cycle, the concentration of chromium has declined rapidly from 25.6wt% at matrix to 0.4wt% at the outer substrate near the scale/substrate interface. After six test cycles, iron is depleted severely in the outer substrate and chromium outward diffusion occurs from alloy matrix to outer side, while nickel content is relatively high in the outer part of substrate.

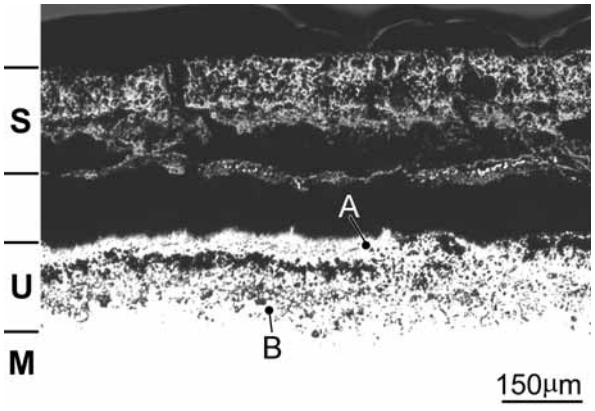

(a)

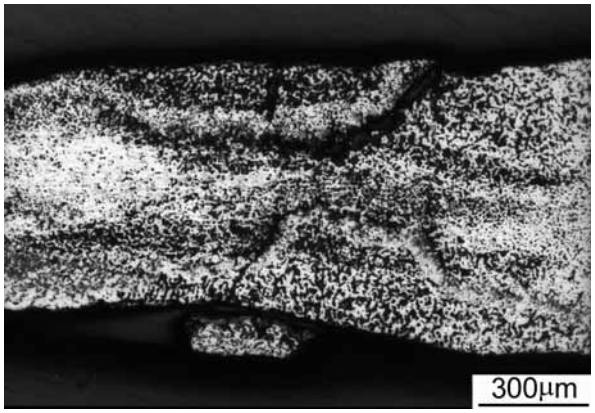

(b)

Fig. 18 Cross sections of uncoated 310SS deposited with NaCl. (a) four cycles, (b) ten cycles (Maker S: scale; U: subscale; M: matrix)

According to XRD identification, the outer scales consist of mainly Fe_2O_3 and Fe_3O_4, while the inner scales consist of Fe_3O_4, Cr_2O_3 with a trace of SiO_2. The total depths of attack versus number of cycles are illustrated in Fig. 19. The total depth of attack increases with increasing cycles, so that specimens have been fully penetrated after nine test cycles.

Table 2 The quantitative analyses in the bulk alloy substrate between the voids after cyclic test (wt%)

Number of cycles	Position	Fe	Ni	Cr
2	Point A: at outermost subscale as shown in Fig. 18	43.3	56.3	0.4
	Point B: at innermost subscale as shown in Fig. 18	56.2	20.6	23.2
6	As point A	19.7	80.0	0.3
	As point B	68.0	28.1	3.9

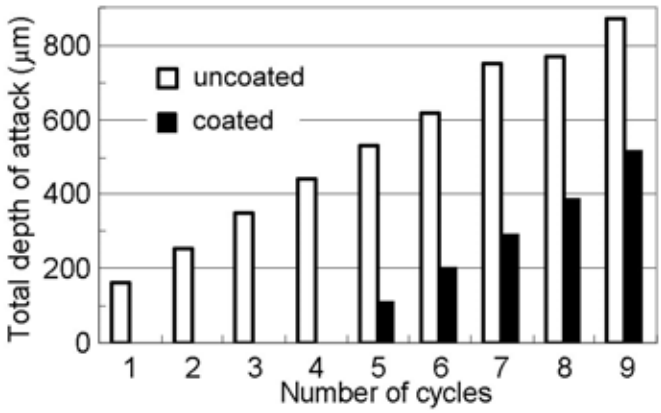

Fig. 19 The total depths of attack of uncoated and coated 310SS deposited with NaCl in each cycle

2. Corrosion of 310 with hot-dip aluminum-7%silicon coating

For hot-dipped specimens without an NaCl deposit, some small voids appear in the outer aluminized layer and the coating layer is unbroken after seven cycles of testing as shown in Fig. 20. Five distinct layers can be observed in the as-exposed coupon: void zone, Fe-Al, Ni-Al, ferrite and the matrix austenite, respectively.

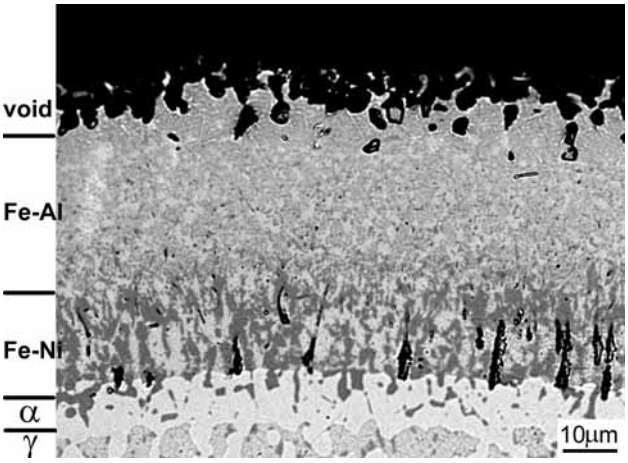

Fig. 20 Optical cross-sectional micrograph of coated 310SS without NaCl deposit exposed at 850°C for seven cycles, at elevated temperature for 20 hr and air-cooling for ten min

For the coated specimens with repeated NaCl deposits, the aluminized layers are adherent on the specimens during the first four heating-cooling test, while voids form in the aluminized layer. A typical cross-sectional BEI micrograph of coated 310 alloy with 2 mg/cm^2 NaCl deposit treated at 850°C for 20 hr and the corresponding X-ray maps are shown in Fig. 21. A thin aluminum oxide forms on the surface, while internal voids filled with oxides appear in the outer aluminized layer which is similar to that without NaCl deposit. XRD analyses (Fig. 22(a)) show that the aluminized layer consists of mainly Al_2O_3, Fe_2Al_5, $FeAl_3Si_3$, and FeAl. After four cycles of testing, a thick alumina oxide scale forms on the outer aluminized layer and interconnecting void networks have been spread over the aluminized layer as shown in Fig. 23. XRD analyses (Fig. 22(b)) of the scale formed on the surface and the aluminized layer show that Al_2O_3,

NiO, ferrite, and AlNi are the main phases present. The quantitative analysis of the EDS in the aluminized layer (Fig. 24) reveals the position of the formed phases. After testing for five cycles as shown in Fig. 25, a thick external scale in the vicinity of 175 μm thickness forms and chlorides have penetrated toward the alloy matrix, while iron concentrates in the outer scale and chromium is richest on the inner side of scale, corresponding to the formation of the outer-scale layer of Fe_2O_3 and the inner-scale layer of Cr_2O_3. In addition, chromium is the element depleted most severely in the subscale attack region, while nickel content is relatively high in this region. After the fifth test cycle, scales peel off entirely after cooling, and light brown with part green corrosion products can be observed at the alloy substrate side of the scale/substrate interface. Once the coatings lose their protection function during testing, the corrosion morphology of the underlying alloy is similar to that seen in tests without coatings. From the above observation, the NaCl deposition leads to accelerated-degradation of hot-dip aluminum-7%silicon coatings on the alloy substrate. XRD analyses show that scales scales consist of Fe_2O_3, Fe_3O_4 and Cr_2O_3, NiO, and Al_2O_3 after five cycles of test, the point in time when the aluminized layer breaks down.

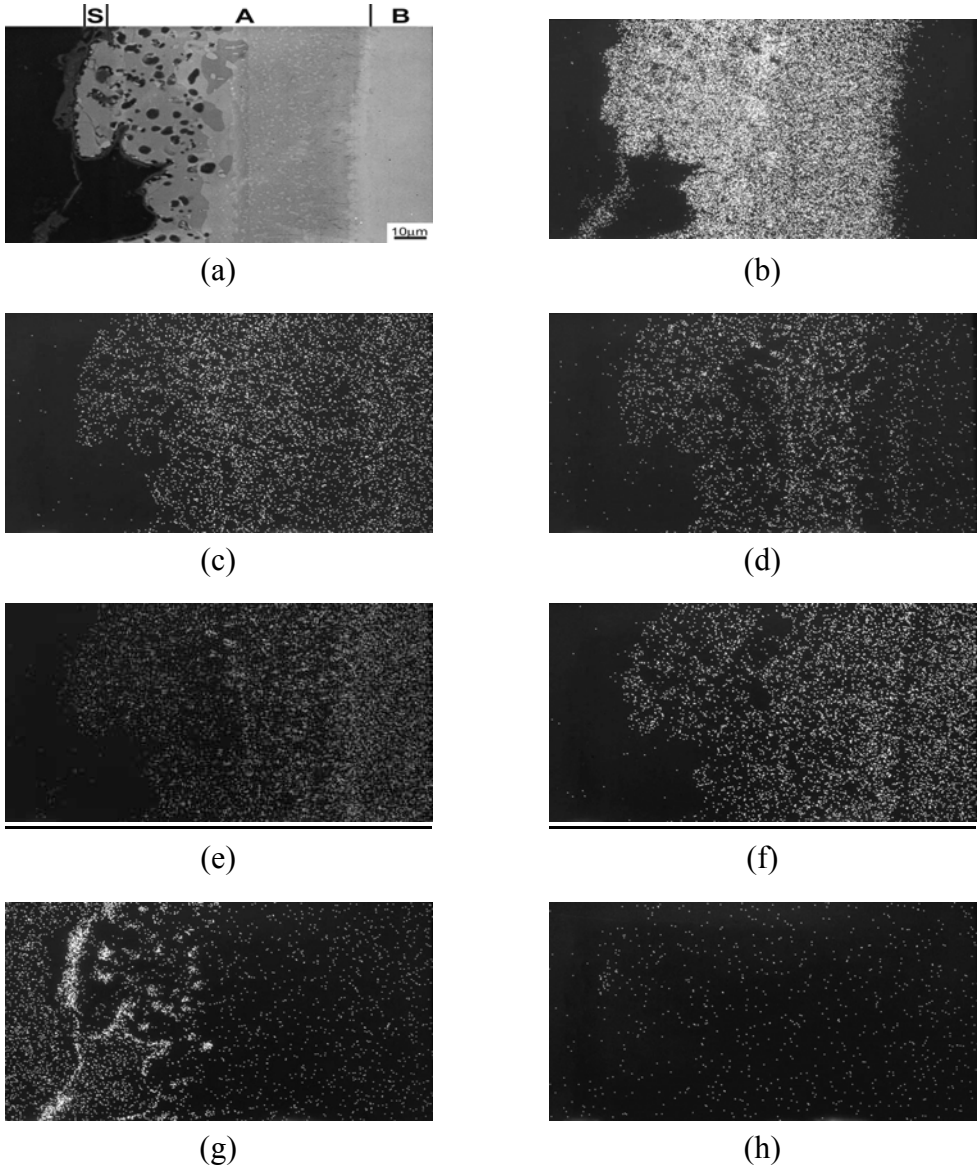

Fig. 21 (a) Cross-sectional BEI micrograph of Al-coated 310SS with 2 mg/cm^2 NaCl deposit treated at 850°C for 20 hr, and X-ray maps of (b) Al, (c) Fe , (d) Si, (e) Cr, (f) Ni, (g) O, (h) Cl of (a). (Maker S: scale; A: aluminized layer with voids filled with internal oxides in the outer layer; B: the alloy substrate)

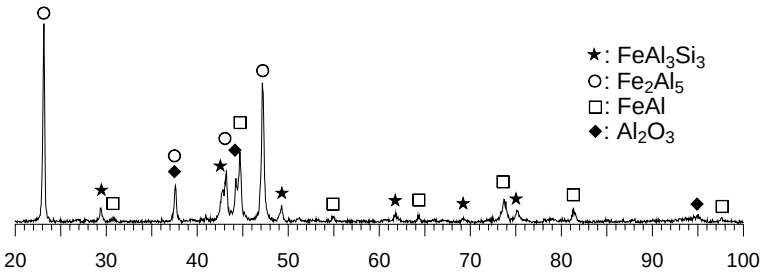

(a)

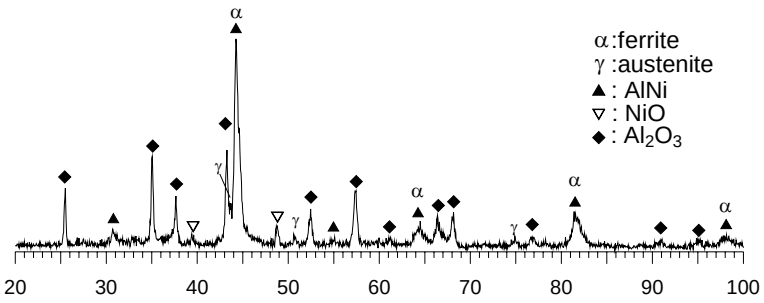

(b)

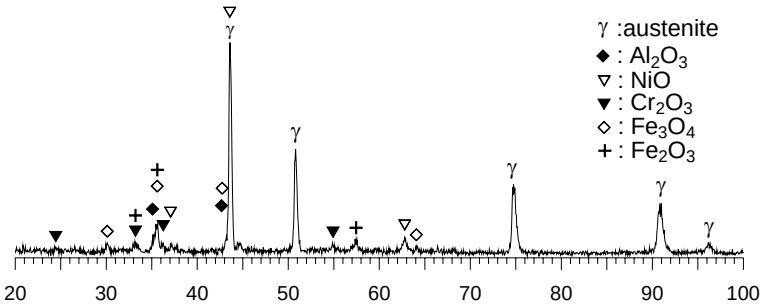

(c)

Fig. 22 XRD analysis of aluminized coated 310SS with repeated NaCl depositing exposed at 850°C for (a) one cycle, (b) four cycles (c) five cycles

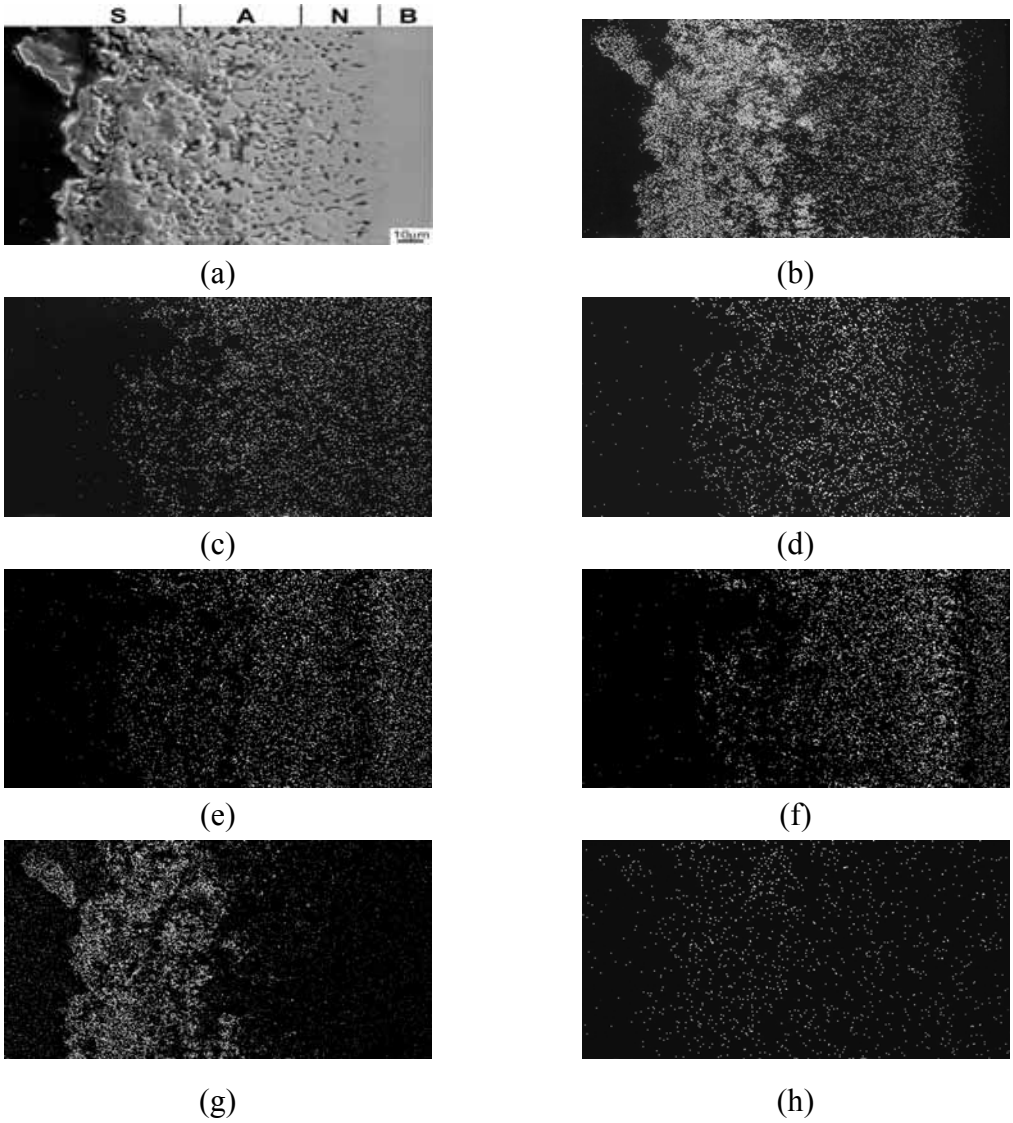

Fig. 23 (a) Cross-sectional SEI micrograph of Al-coated 310SS with repeated NaCl deposit treated at 850°C for four thermal cycles, and X-ray maps of (b) Al, (c) Fe , (d) Si, (e) Cr, (f) Ni, (g) O, (h) Cl of (a). (Maker S: scale; A: aluminized layer with voids filled with internal oxides; N: Ni-Al layer; B: the alloy substrate)

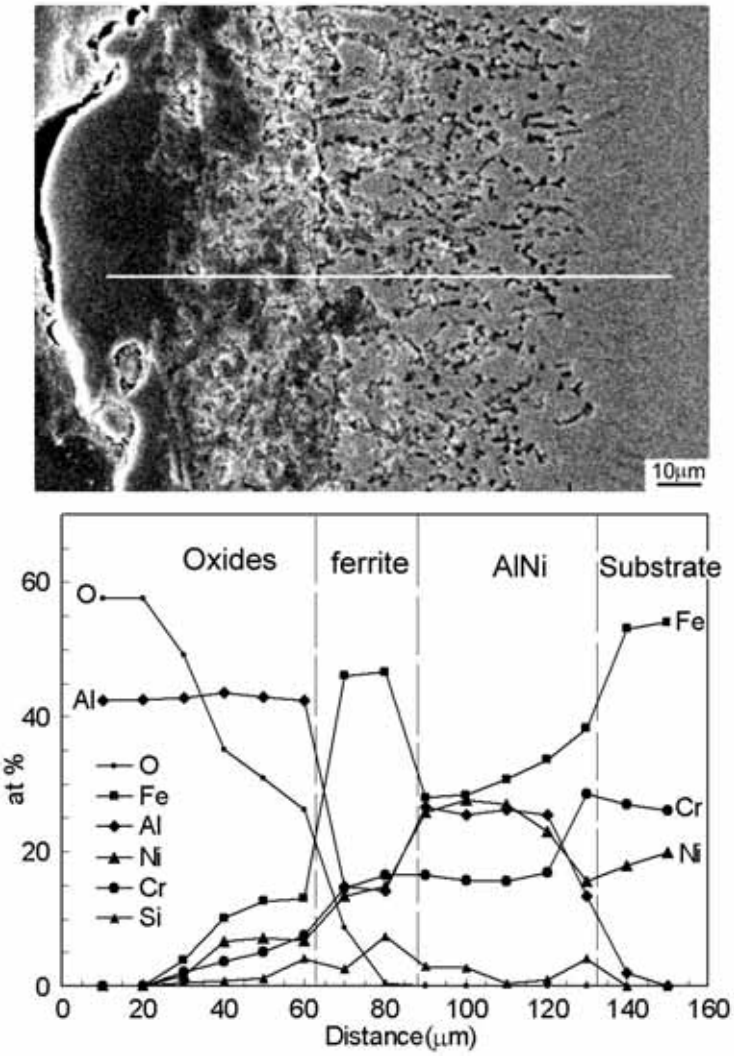

Fig. 24 EDS results showing the concentration variations of Al, Fe, Si, Cr, Ni, and O elements near the surface of the aluminized 310 stainless steel with repeated NaCl depositing exposed at 850°C for four thermal cycles

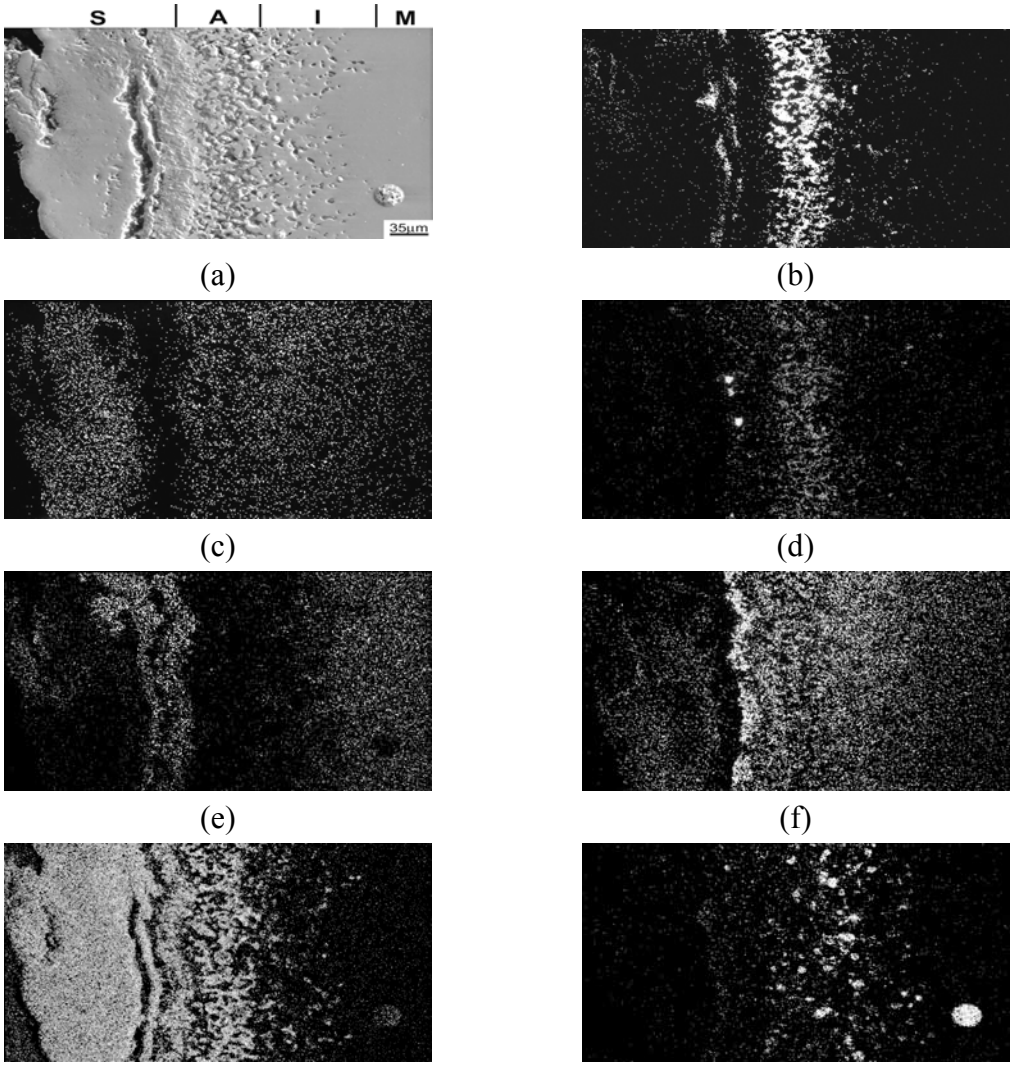

Fig. 25 (a) Cross-sectional SEI micrograph of Al-coated 310SS with repeated NaCl deposit treated at 850°C for five thermal cycles, and X-ray maps of (b) Al, (c) Fe , (d) Si, (e) Cr, (f) Ni, (g) O, (h) Cl of (a). (Maker S: scale; A: aluminized layer with voids filled with internal oxides; I: internal void zone in the alloy substrate; M: matrix)

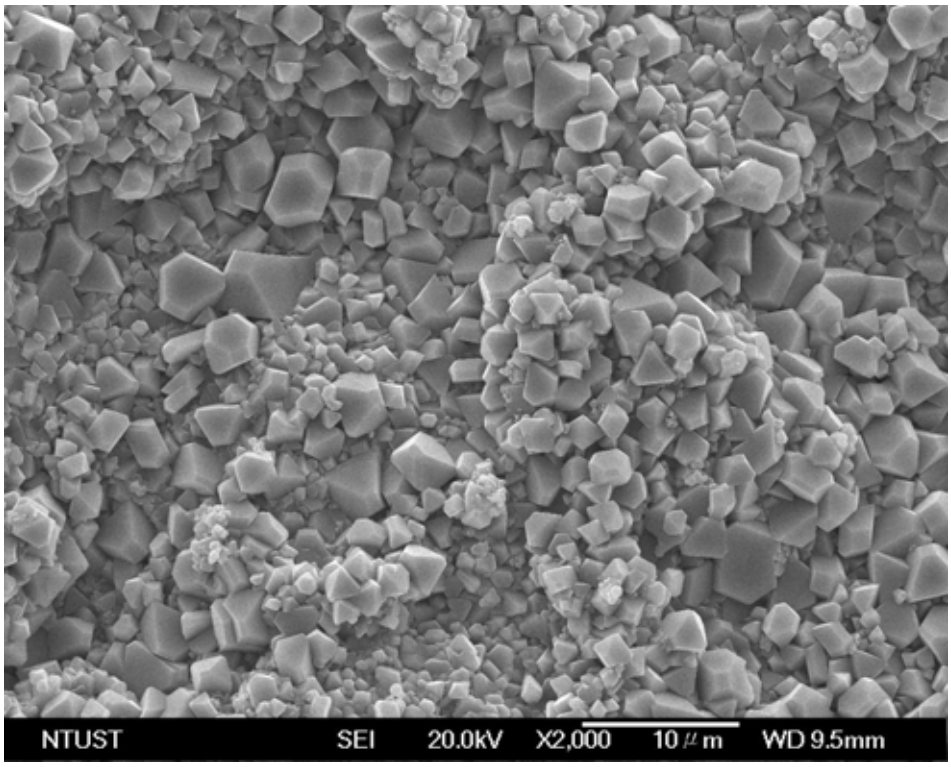

Fig. 26 Surface morphology of 310SS at 850°C for 9 cycles withtout coating and depositing

D. Discussion

The high-temperature corrosion behavior and kinetics evolution of austenitic Fe-Cr-Ni alloys coated with NaCl have been studied previously[74]. When 310 stainless steel is oxidized at either 750°C or 850°C without NaCl coating, only a slight weight gain is typically observed and no internal attack can be found. Protection is attributed to the formation of a compact chromic oxide, which acts as a protective barrier as shown in Fig. 26. When 310 stainless steel with a NaCl deposit is exposed at elevated temperature in static air, the alloy experiences severe corrosion loss and internal attack produces voids. The oxidation of the alloy is accelerated by NaCl deposition and

the weight gains at 850°C are larger than those at 750°C. In NaCl-induced accelerated oxidation, the reaction is generally believed to be initialized by oxychloridation, the reaction between metals, NaCl, and oxygen, to form metal oxides and release chlorine[85,86]. The corrosion mechanism can be explained as follows.

Table 3 The thermal properties of various chlorides at 850°C[87]

Chlorides	$FeCl_2$	$FeCl_3$	$CrCl_2$	$CrCl_3$	$NiCl_2$
Dissociation pressure (atm)	1.7×10^{-10}	7.3×10^{-8}	1.4×10^{-12}	3.2×10^{-10}	2.8×10^{-8}
Vapor pressure (atm)	1.8×10^{-1}	9.8×10^{-4}	1.5×10^{-3}	1.25×10^{-1}	9.6×10^{-2}

Since the melting point of NaCl is 801°C, it can be expected that the specimens will be corroded in a state of molten salt within a short-term stage. The corrosion was mainly due to an oxidation of metal by the oxygen or water vapor in molten salt, which was then followed by dissolution of metal oxides in the melt[3,p169] as shown in Eq. (11). The Cl_2 produced from oxychloridation would attack metals to form metal chlorides via Eq. (12). Due to the low melting point and high vapor pressure as shown in Table 3[87], the metal chlorides would volatilize outward to the places with higher oxygen partial pressure, which would then cause the substitution of oxidation as indicated in Eq. (13). The Cl_2 released from the reaction again. Therefore, chlorine can catalyze the oxidation in a way of cyclic reaction[88].

Oxychloridation: $M + NaCl + O_2 \rightarrow$ M-oxide + Na-oxide + Cl_2 (11)

Chloridation: $M + Cl_2 \rightarrow$ M-Chloride (12)

Oxidation: M-Chloride + $O_2 \rightarrow$ M-oxide + Cl_2 (13)

In the case of oxychloridation, the chromium would react with oxygen and NaCl to form Na_2CrO_4 as shown in Eq. (14). The mixture of NaCl and Na_2CrO_4 formed a eutectic system with a lower melting point of 577°C. The role of Na_2CrO_4 can be considered an intermediate compound to supply adequate oxygen from the gas phase to the metal across the melt[75-76]. The Cr_2O_3 would gradually be formed through the intermediate compound as shown in Eq. (15).

$$Cr + 2O_2 + 2NaCl_{(g,l)} = Na_2CrO_4 + Cl_2 \quad (14)$$

$$\Delta G_{850°C(g)} = -431KJ,\ \Delta G_{850°C(l)} = -311KJ$$

$$4Cr + 3O_2 + NaCl \rightarrow \text{intermediate compound} \rightarrow 2Cr_2O_3 + NaCl \quad (15)$$

$$\Delta G_{850°C} = -1690KJ$$

Similarly, during the initial oxychloridation, iron may also react with both oxygen and NaCl as Eqs. (16) and (17).

$$2Fe + 2O_2 + 2NaCl = 2NaFeO_2 + Cl_2 \quad (16)$$

$$\Delta G_{850°C} = -255KJ$$

$$2Fe + 2O_2 + 2NaCl = Fe_2O_3 + Na_2O + Cl_2 \quad (17)$$

$$\Delta G_{850°C} = -184KJ$$

Regarding the chloridation, it is possible that the Cl_2 produced from oxychloridation would react with iron, chromium and nickel as Eq. (18).

$$x(Fe,Cr,Ni) + yCl_2 = x(Fe,Cr,Ni)\text{-chlorides} \quad (18)$$

$$\Delta G_{850°C} < 0$$

Oxide is the ultimate stable phase in the metal-oxygen-chlorine system. The oxygen partial pressure in the atmosphere side is relative high as (Fe, Cr)-chlorides are gradually formed and consumed the chlorine. It results in an oxidation occurred as Eq. (19).

The reaction free energy of Eq. (20) is positive since the free energy of formation of NiO and $NiCl_2$ are very close. $NiCl_2$ would not be oxidized into NiO unless the oxygen partial pressure in the environment is much greater than the chlorine partial pressure. In other words, the oxidation of the nickel chloride refers to the corrosion stage. When the molten salt is still remained on the surface of the specimens, $NiCl_2$ will not be oxidized. In the latter stage of high-temperature corrosion, if the oxygen partial pressure is much greater than the chlorine partial pressure, Eq. (20) may possibly occur.

$$x(Fe,Cr)\text{-chlorides} + yO_2 = x(Fe,Cr)\text{-oxide} + zCl_2 \quad (19)$$

$$\Delta G_{850^\circ C} < 0$$

$$NiCl_2 + \frac{1}{2}O_2 = NiO + Cl_2 \quad (20)$$

$$\Delta G_{850^\circ C} = +46.74 \text{ KJ}$$

Along with the oxychloridation process, some of the chlorine attacks the alloy to produce chloridation and that facilitates oxidation of metal chlorides to metal oxides. The metal oxides arising from metal chlorides tend to be individual particles[89], and are responsible for the formation of non-continuous oxide scale.

In this study, the scales formed on the alloy consist of mainly Fe_2O_3, Fe_3O_4 and

Cr_2O_3 and show their non-protective character in each thermal cyclic test. The initial oxychloridation retards the formation of protective oxide scale, and the produced chlorine may further attack the alloy substrate and react with chromium, exhibits high reactivity with chlorine as indicated in Table 3, and quickly forms $CrCl_3$ or $CrCl_2$ [90-92].

As shown in Table 3, the vapor pressure of $CrCl_3$ and $CrCl_2$ at 850°C are 1.25×10^{-1} atm and 1.54×10^{-3} atm, respectively[87]. Once $CrCl_2$ or $CrCl_3$ is formed, the metal chloride volatizes outward. The metal chloride with low melting points and high vapor pressures appear to volatilize outwardly to a region where an appropriate partial pressure of oxygen enables the onset of oxidation. Oxidation of metal chlorides seems to occur there. The chloridation/oxidation cyclic reactions in the alloy substrate suffice to explain the consumption of chromium in the alloy substrate. From the quantitative analyses of the bulk alloy substrate after cyclic test as shown in Table 2, the concentration of chromium declines rapidly, followed by declining iron concentration when the number of cycles increases. The depletion of chromium leads to the higher content of iron and nickel in the alloy substrate. Iron is the second element consumed due to its high reactivity with chlorine. This process leads to the formation of interconnecting void networks. Therefore, with the leakage of chromium from the alloy substrate, the repeated NaCl deposition results in severe corrosion loss as well as internal voids during every cycle as shown in Fig. 18. Specimens are penetrated within ten cycles of test.

Compare Fig. 18, 19, and 20. The alloy coated with hot-dip aluminum-7%silicon layer with an initial NaCl deposit shows much better corrosion resistance than that without HDA treatment. With the formation of alumina scale on the surface, the coat-

ing layer is beneficial for corrosion resistance of alloy at 850^{o}C in the NaCl deposit environments. When a protective oxide scale forms at the beginning of the reaction readily, the alloy substrate can be separated from the contact of NaCl. Thus, the oxychloridation in the initial stage can be inhibited to some extent, and the prevention of chloridation/oxidation cyclic reactions in the alloy substrate is achieved.

For the thermal-cycling corrosion of hot-dipped 310 alloy with NaCl deposit in each cycle, a schematic representation of corrosion processes is proposed in this study as shown in Fig. 27. During the first cycle as indicated in Fig. 21, Fig. 27(a) and (b), only some voids filled with oxides formed near the surface of aluminized layer, which is similar to that without NaCl deposit. The phases present in the aluminized layer are mostly aluminum-rich phases, such as Fe_2Al_5, $FeAl_3Si_3$, and FeAl. The only difference is that the void zone formed on the coating with NaCl deposit is thicker than that without NaCl. That means the formation of voids result from Al element inward diffusion through the aluminized layer, which leads to the coalescence of vacancies to form voids beneath the scale. The chlorine produced by the oxychloridation may pass along the voids and attack the aluminized layer to react with aluminum, forming aluminum chloride gas (such as $AlCl_{3(g)}$). The Gibbs free energy change of the reaction of chloridation of aluminum is negative at 850^{o}C and therefore possible[93].

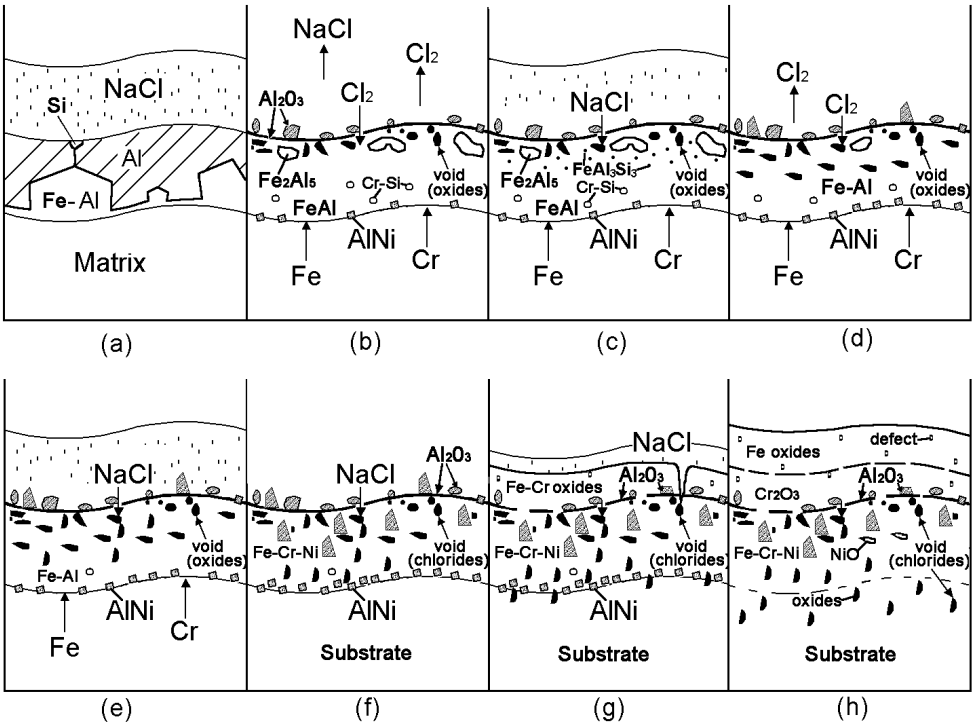

Fig. 27 Schematic illustration of corrosion processes on coated 310SS with NaCl deposit in each thermal cycle test. (a) NaCl deposit, (b) oxides form on the surface of the aluminized layer and voids form in the outer aluminized layer, (c) NaCl penetrates through voids and cracks, (d) growth of voids in the aluminized layer, (e) NaCl inward penetration, (f) occurrence of internal attack, (g) NaCl penetrates into the alloy substrate, (h) the aluminized layer breaks away

The boiling points of $AlCl_{3(g)}$ is only 182°C. When the chloride is formed from the above reaction, the chlorides volatilize, leading to catalytic actions of chloride or chlorine as mentioned above. Thus, the existence of NaCl is responsible for the formation of thicker void zone in the outer aluminized layer.

With the additional thermal cycles, aluminum-rich phases, such as Fe_2Al_5 and

FeAl disappear eventually. Nevertheless, during the first four cycles of testing the aluminized layer has still enough aluminum to heal alumina scale and resist the attack caused by NaCl. Besides, the outward diffusion of iron and chromium from the matrix toward the aluminized layer leads to the gradual pilling up of nickel at the interface between the aluminized layer and the alloy substrate. Ni-Al intermetallic compounds, such as AlNi form at the aluminized layer side near the substrate/the aluminized layer interface.

As shown in Fig. 27(c), the deposited NaCl penetrates along the voids into the aluminized layer and attacks the aluminized layer as shown in Fig. 23 and Fig. 27(d). As the aluminized layer becomes porous and non-protective, the deposited NaCl penetrates this layer into the alloy substrate and proceeds by means of oxychloridation as well as chloridation/oxidation cyclic reactions, leading to void formation in the alloy substrate (Fig. 24 and Fig. 27(e~h)). The catalytic actions of chlorides and chlorine result in the formation of oxides and metal chlorides in the internal voids. With increasing numbers of cycle, the aluminum in the aluminized layer is consumed. The alloy substrate then experiences corrosion morphology of alloy as if it had not been coated. Clearly, the repeated NaCl deposition result in accelerated degradation of hot-dip aluminum-7%silicon coatings on the alloy substrate.

In this study, the repeated NaCl deposit causes the breakdown of the protective coating layer first, and then attacks the alloy substrate, leading to the formation of internal voids filled with metal oxides chlorides and in the alloy substrate. Moreover, the formation of voids and porosity in the aluminized layer is beneficial to reducing total

stress accumulated during heating and cooling processes[94]. Therefore, the degradation of coated alloy is dominated by the repeated NaCl deposition and the effect of thermal cycle in the aluminized layer plays a supporting role.

E. Summary for hot-dipped aluminizing 310SS

1. For 310SS alloy without hot-dip aluminum-7%silicon coatings, the repeated NaCl deposition leads to severe corrosion loss as well as internal void formation, and oxide scale spalled during every thermal cycle test. The total depth of attack increases rapidly with increasing cycles.
2. The hot-dipped alloy with repeated NaCl deposits shows much better corrosion resistance than that without aluminum coating in thermal cycling test. However, the repeated NaCl deposit causes the breakdown of the coated layer after five cycles. When the protective coatings break down, the corrosion behavior of 310SS alloy is similar to that observed in uncoated control specimens.
3. The degradation of the aluminized layer on alloy is dominated by the repeated NaCl deposition, and the effect of thermal stress in the coating layer plays a supporting role in this study.

CHAPTER V

THE HIGH-TEMPERATURE OXIDATION BEHAVIOR OF AN ALUMINIDE COATING ON 9Cr-1Mo STEEL

A. Introduction

9Cr-1Mo alloy is widely used as tubes for heat exchangers, and offers good oxidation good corrosion resistance with good high-temperature strength for operating temperatures up to 650°C. To improve oxidation resistance above 650°C, a surface coating or modification to produce a more corrosion resistant surface layer is commonly used. Steels coated with aluminum apply generally in the electric power plants, petrochemical industries and other energy conversion systems due to their low cost, good thermal conductivity and oxidation resistance performance. Many research activities have focused on it elsewhere[95-99]. There are variety of aluminum-coating processes, including hot dipping, thermal spray, pack cementation, slurry, cladding, electroplating, etc. On the basis of cost and feasibility in industrial processes, hot-dip aluminizing process, as a surface treatment of alloys, is used.

The performance and phase constitution of the Fe-Al alloying layer depend on the composition of raw materials, temperature, time history and other processing factors. However, the growth and formation mechanism of the Fe-Al alloying layer is seldom investigated systematically. In this investigation, the high temperature oxidation behavior of a 9Cr-1Mo alloy with hot-dip treatment was explored. The oxidation behavior was evaluated by employing thermal gravimetric analysis (TGA) in ambient air at

750 and 850^{O}C. After TGA, the chemical composition and microstructure of the oxides formed on the specimens were also examined.

B. Experimental procedure

A commercial cold rolled ASME SA213 T9 steel sheet was used as experimental materials in this study. The chemical composition of the alloy is Fe-0.09%C -0.36%Si-0.40%Mn-0.02%P-8.25%Cr-0.04%Ni-0.93%Mo-0.01%Cu-0.225%V in wt.%) via ICP (inductively coupled plasma atomic emission spectrometry) analysis. Rectangular specimens were cut to the dimensions of 15×10×2mm by a water-cooled cutting machine. Specimens for further hot-dip treatment were hung by stainless steel wires and coated with uniform weld flux. Then specimens were dried and immersed into a molten bath of 700°C aluminum-silicon (Al-7%Si-0.3%Mg-0.2%Fe-0.2%Cu in wt.%) for 16 seconds. Silicon was added into the aluminum liquid in order to make the surface of the Fe-Al alloy layer smooth and enhance the interfacial bonding strength[100]. The up and down speed was 18cm/min. Then the hot-dipped specimens were cleaned by a mixed aqueous solution of nitric acid, phosphoric acid, and water in 1:1:1 volume fraction at 60°C. Thickness of the external aluminum coating and aluminized layer was approximately of 25μm after hot-dip treatment.

After hot-dip treated, specimens were exposed in a furnace with static air at 750 and 850°C for 10min, 20min, 30min, 1hr, 8hr, 24hr and 56hr respectively, and then air-cooled to room temperature. The oxidation products were analyzed by X-ray diffraction (XRD) using monochromatic Cu-Kα radiation operated at 40 KV and 100 mA. A sequential grinding technique was adopted to investigate the distribution of the dif-

ferent phases present in the scale and the alloy substrate. Characterization of the cross-sectional scales was carried out with optical microscopy (OM), scanning electron microscopy (SEM), a JOEL-JSM 6500F Field Emission SEM with energy dispersive spectroscopy (EDS), and electron probe microanalysis (EPMA) with X-ray wave-length-dispersive spectrometry (WDS).

C. Results

1. Corrosion kinetics

The corrosion kinetics of the Al layer on the 9Cr-1Mo steel as function of time is plotted in Fig. 28. The corrosion kinetics of the specimens follows a parabolic law as shown in Fig. 29. It indicates that the weight gain kinetics follows a steady state parabolic rate law up to 50 hr at 750 and 850°C, while specimens follow parabolic oxidation rate law only to about 25 hr under 950°C. It shows that the alloy oxidation rate increase with increasing temperature.

2. Morphology and scale constitution

The cross section micrograph of the hot dip aluminide 9Cr-1Mo steel is shown in Fig. 30. Two distinguishing layers are visible in the aluminide layer: an aluminum topcoat and an inner layer composed of Fe-Al intermetallic compounds with dissolved Si and trace Cr. The overall thickness of the coating layer is about 25μm. The Fe-Al intermetallic compounds were dominated by Fe_2Al_5 phase with trace of $FeAl_3$ phases and $FeAl_2$ exist between the Al and Fe_2Al_5 phases by SEM and EDS analysis as shown in Fig. 31.

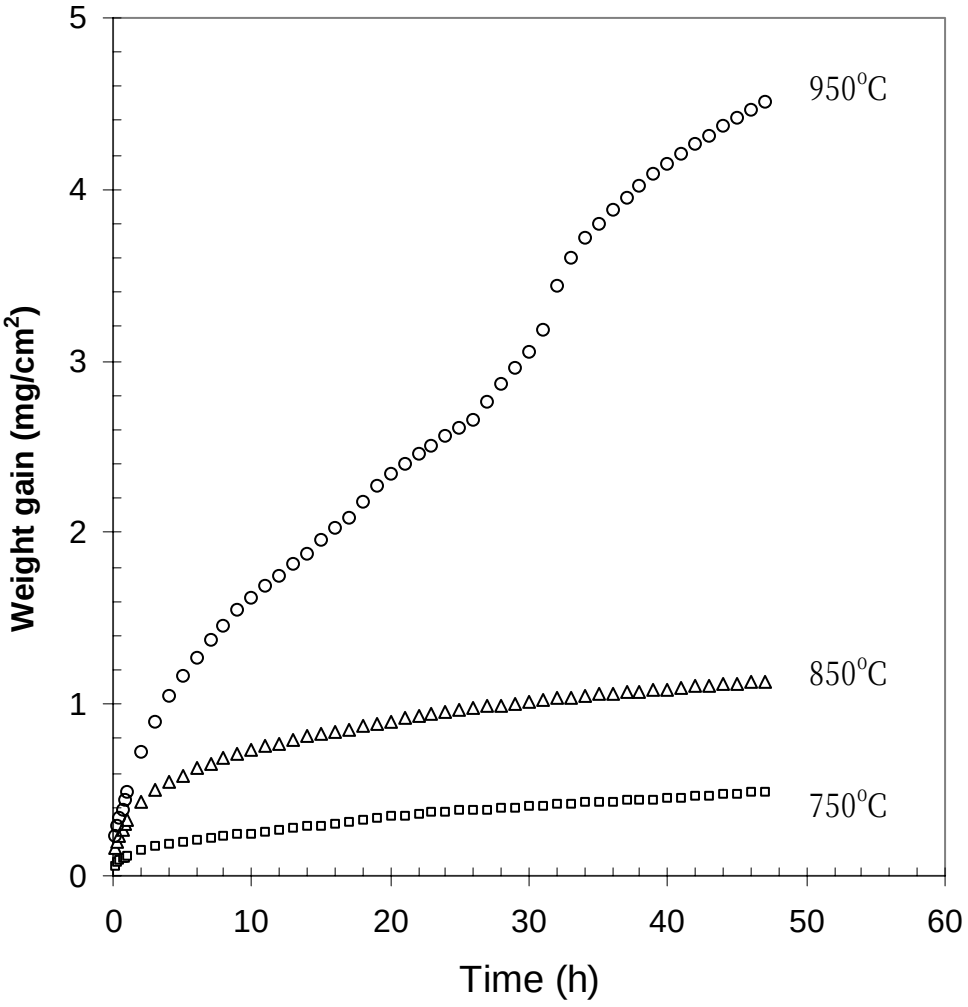

Fig. 28 Corrosion kinetics of 9Cr-1Mo steel as function of time at temperature = 950, 850 and 750°C

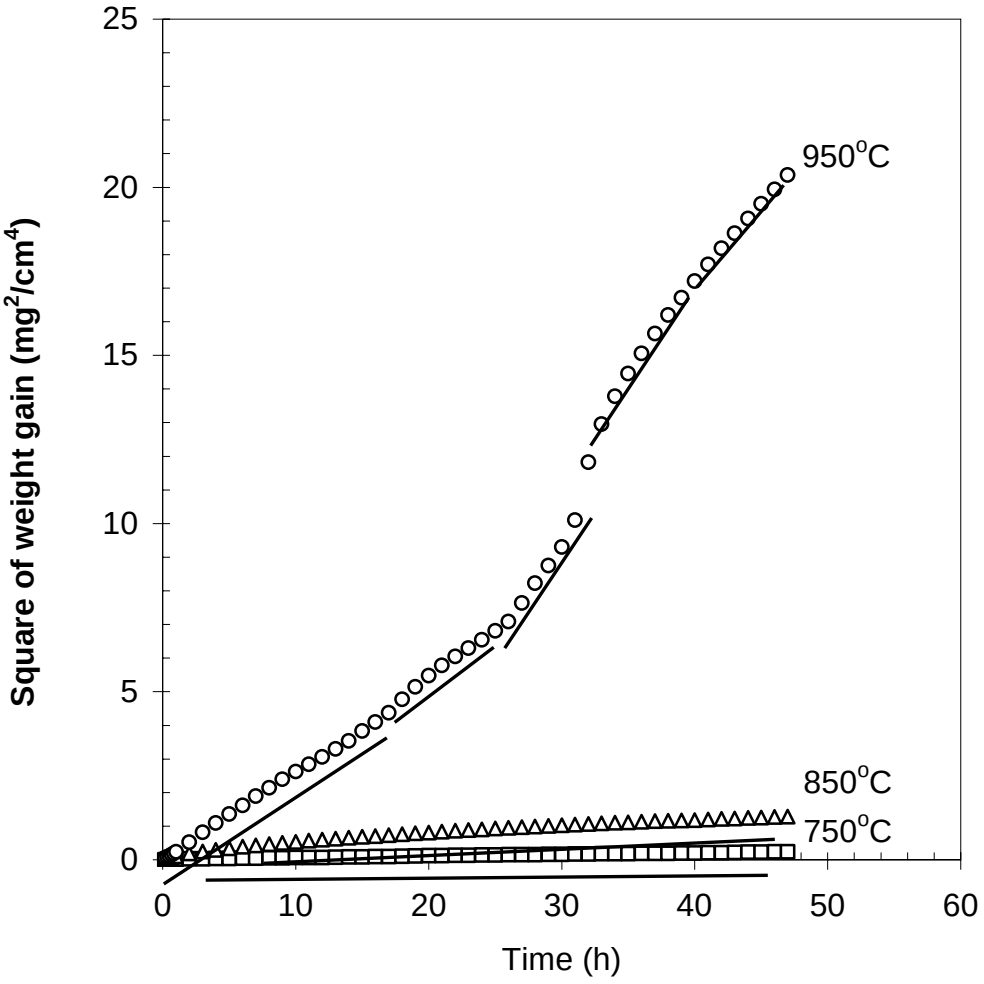

Fig. 29 Corrosion kinetics of 9Cr-1Mo steel (square of weight gaining) as function of time at temperature = 950, 850 and 750°C

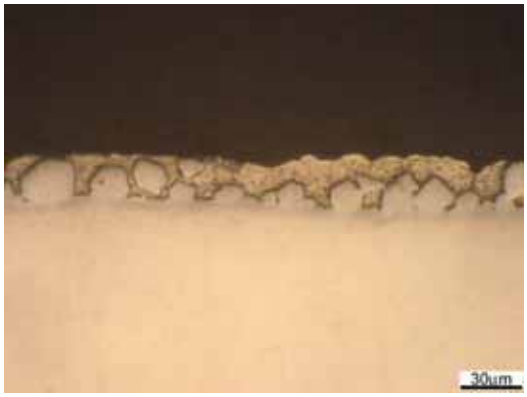

(a)

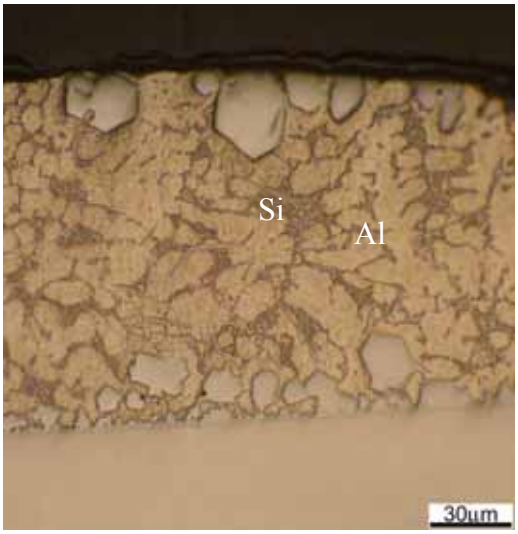

(b)

Fig. 30 Optical cross-sectional micrograph of 9Cr-1Mo steel as coated aluminum

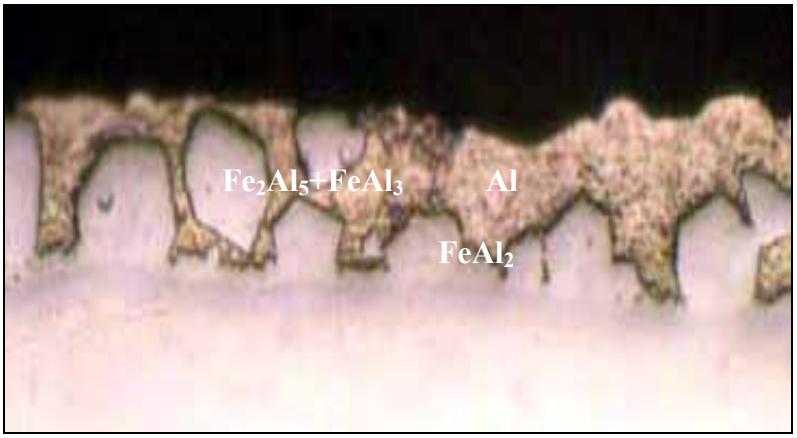

Fig. 31 The phases distribution of Fe-Al intermetallic compound of 9Cr-1Mo steel as coated aluminum

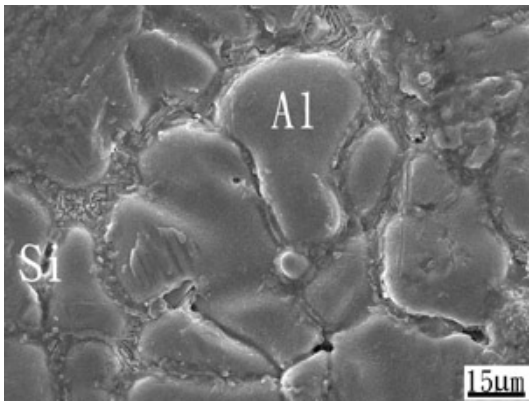

Fig. 32 Optical surface micrograph of 9Cr-1Mo steel as coated aluminum

Optical surface micrograph shows two phases were formed on the hot dip aluminide 9Cr-1Mo steel surface as shown Fig. 32. X ray analysis identifies the two phases are Si phase surrounds Al phase.

Fig. 33 shows typical cross-sectional micrographs of the specimens after oxidation for various time at 850°C and 750°C separatively. At 850°C, the thickness of coating layer increases readily with increasing exposure time within twenty minutes. A few microcracks formed after four minutes. Some cracks opened after ten minutes of exposure. The number of cracks doubled between ten and twenty minutes of exposure. The voids increased, coarsened, and deepen into the interface with time and temperature increasing. There are some cracks penetrating into the substrate surface and voids condense along the interface between intermetallic compound and alloy matrix. The corresponding SEI cross-sectional micrographs of alloys exposed for 8hr and 24hr at 850°C is shown in Fig. 34 and Fig. 35. Fig. 34 reveals that the outer layer under the scale consist of coarse voids, while the inner layer has scattered light gray spots on it. The light gray layer between the previous two layer has some larger coarse voids on it. Fig. 35 shows that the middle light gray layer has vanished and converted into a dark layer after 24hr at 850°C.

A cross-sectional SEI micrograph and the corresponding concentration profiles of Fe, Al, Cr, and Si of specimen exposed at 850°C for 8hr in conjunction with XRD analysis are depicted in Fig. 34 and Fig. 35. Five distinct layers from external scale to matrix are observed: Al_2O_3+FeAl, FeAl, Fe_2Al+Fe_2Al_5, FeAl, and the steel substrate, respectively. A relatively high Al content is detected in the Fe_2Al+Fe_2Al_5 layer.

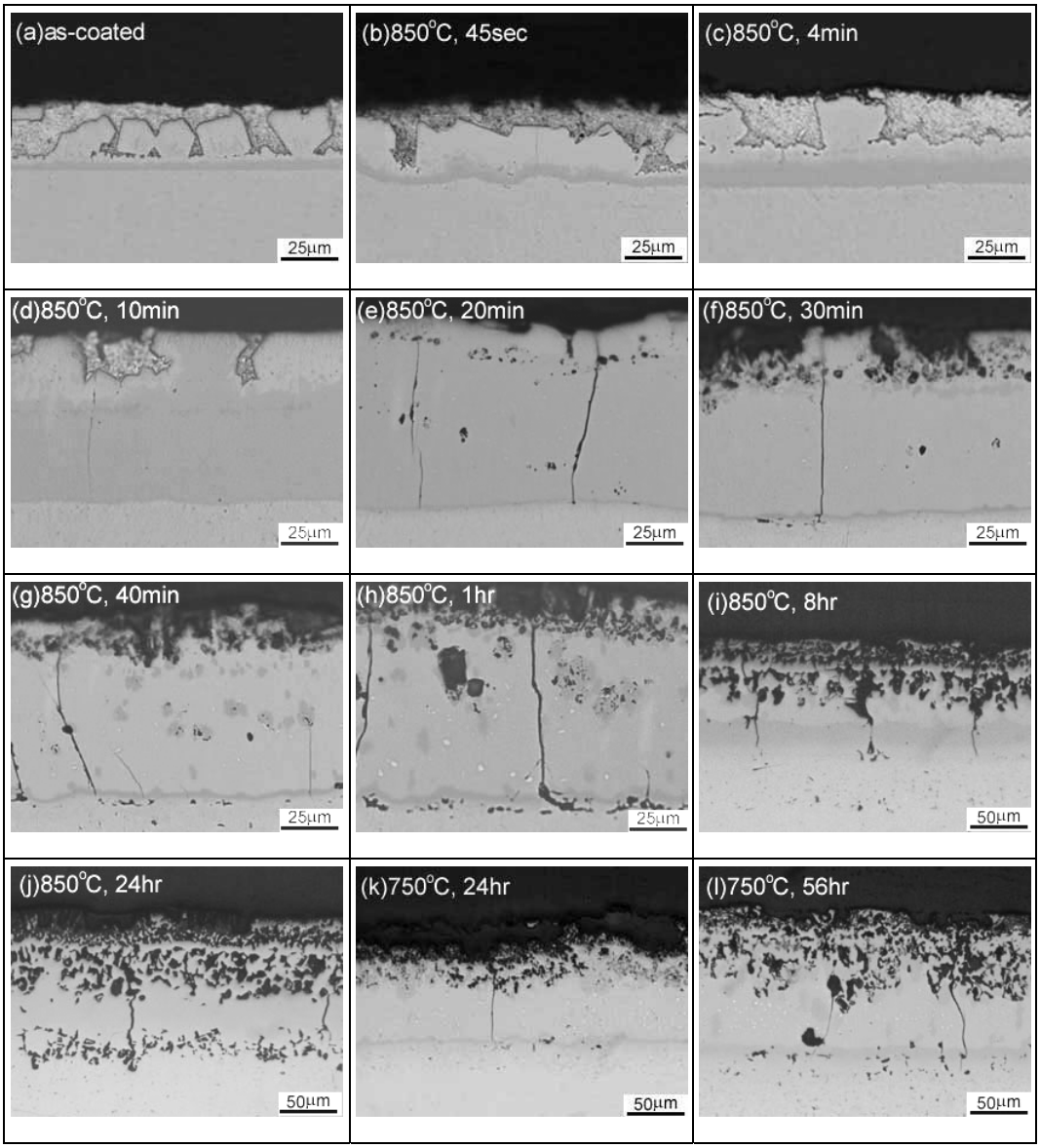

Fig. 33 Optical cross-sectional micrographs of 9Cr-1Mo steel corroded from 45 sec to 56 hr at 750 and 850°C

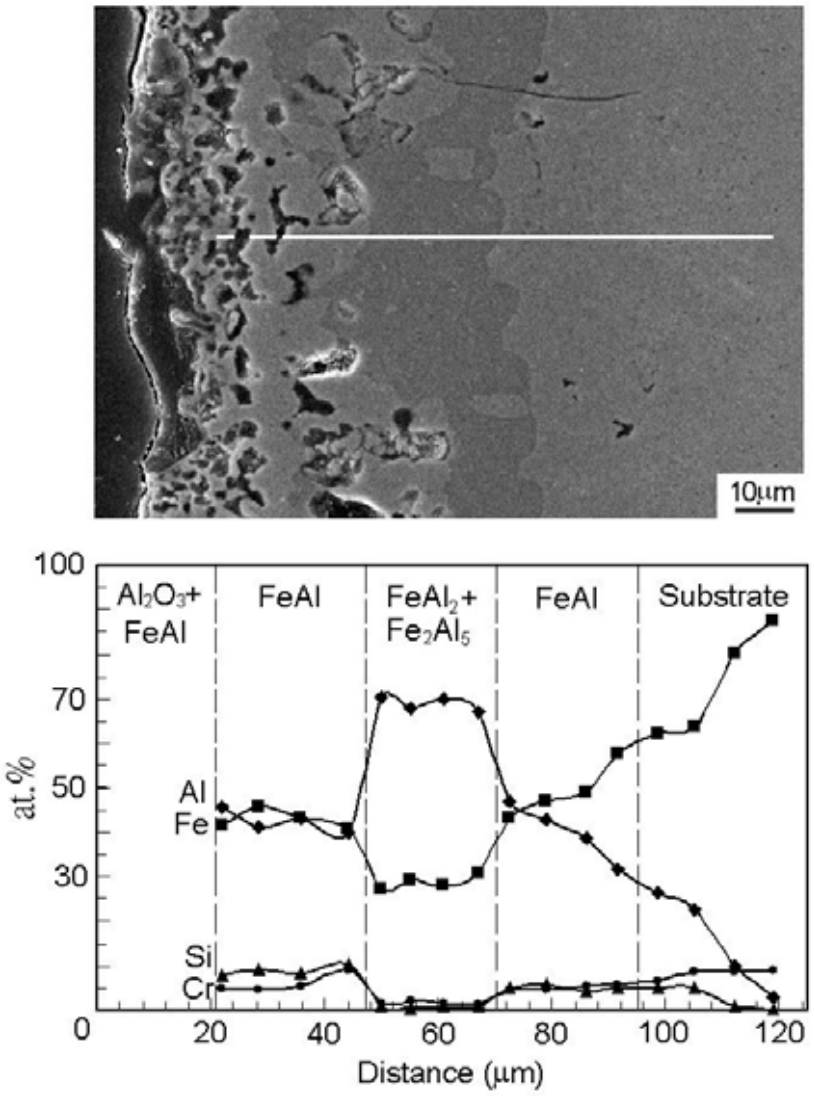

Fig. 34 SEI cross-sectional micrographs of 9Cr-1Mo alloy exposed for 8hr at 850 ^{o}C

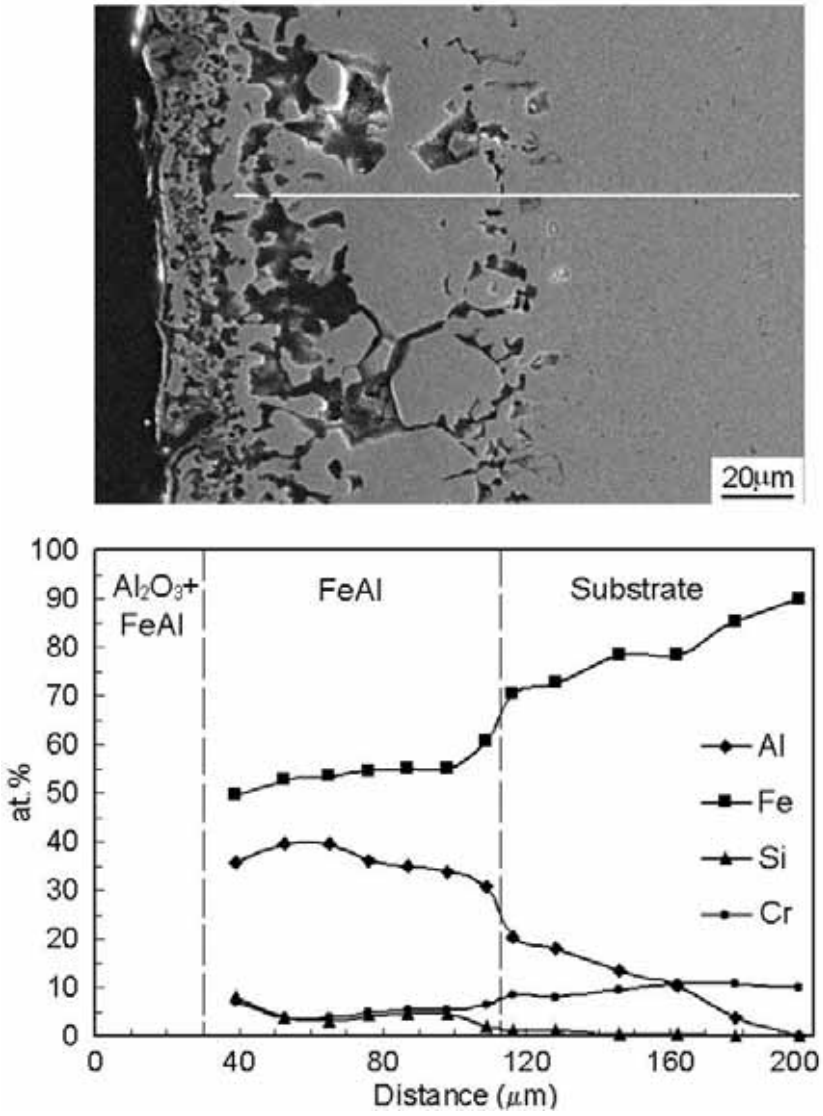

Fig. 35 SEI cross-sectional micrograph of 9Cr-1Mo alloy exposed for 24hr at 850 °C

Typical results of the EPMA examination of specimens exposed for 10min, 30min, 1hr, 8hr and 24hr at 850°C are shown in Fig. 36 and Fig. 37. Comparing with the SEI cross-sectional micrographs, the X-ray mapping of the 9Cr-1Mo steel specimen showed the light gray phase and coarse voids is rich in Si and Cr, and aluminum is dominant on the dark gray phase. Oxygen appeared in the larger coarse voids and it can be observed throughout the external scale. Mo was almost nil in the scale and in the intermetallic compounds.

XRD analyses of the aluminide layer after 9Cr-1Mo steel oxidized at 750 and 850°C for various time is shown in Fig. 38 and Fig. 39. For ten minutes oxidation at 850°C, phases present in the aluminide layer as if it was observed on the as-coated specimen. The phases consist of Al, Si, $FeAl_3$, Fe_2Al_5, and $FeAl_2$. The phases of Fe_2Al_5, $FeAl_2$ and FeAl can be detected as the oxidation duration is increased. The aluminide layer is dominated by FeAl intermetallic after 24hr exposure. For oxidation at 750°C for 24hr, the phases present in the aluminide layer are similar to that of specimen oxidized at 850°C for 8hr. They consist of Fe_2Al_5, $FeAl_2$, and FeAl.

D. Discussion

1. Corrosion kinetics

9Cr-1Mo steel is used as a corrosion resistant alloy in pressurized water reactors and heat exchanger tubes. The boiler code allows it to be used in thermal environments with temperatures up to 650°C. Based on this research, the aluminide coated 9Cr-1Mo steel can resist oxidation effectively up to 850°C as shown in Fig. 28.

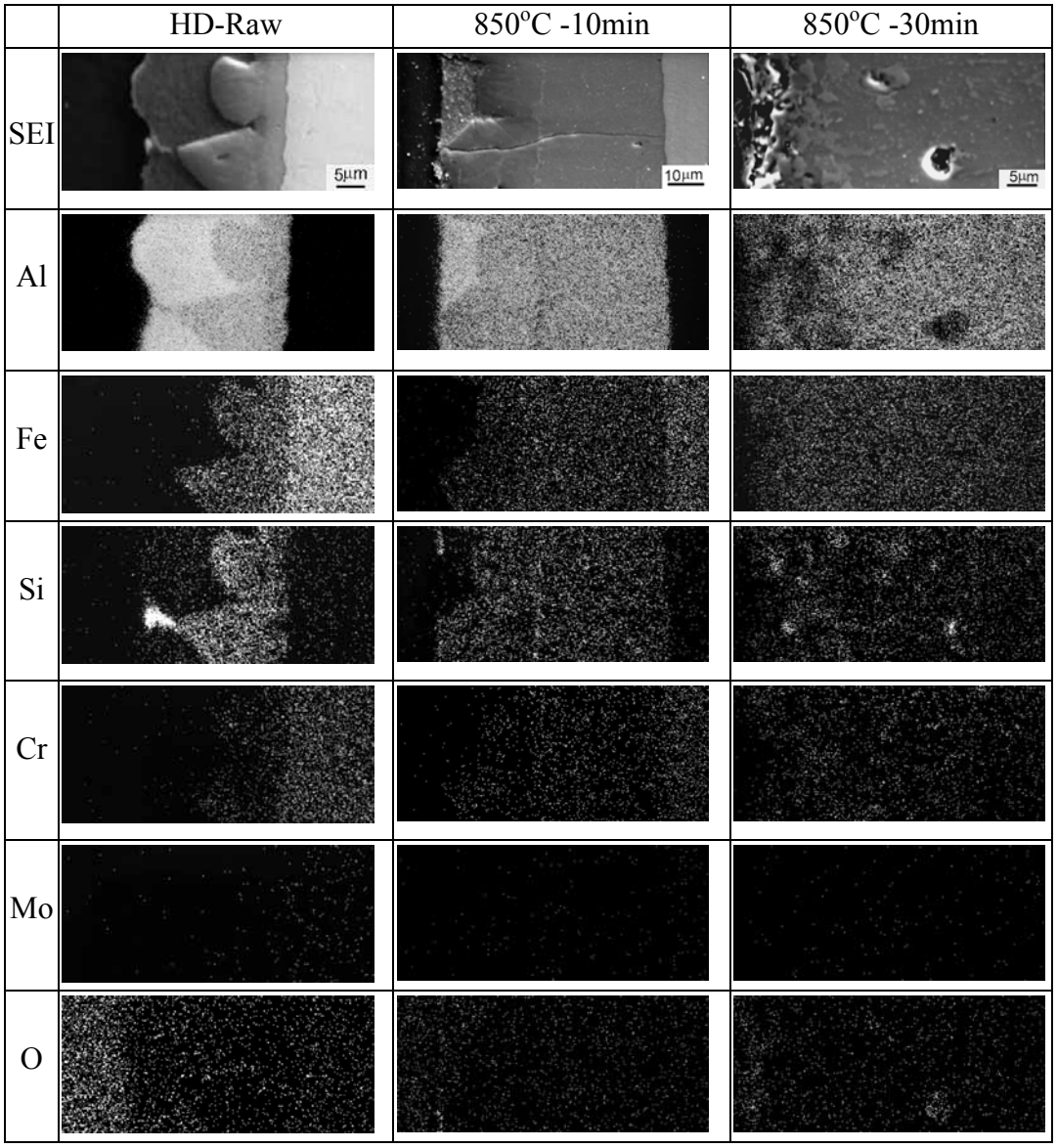

Fig. 36 EPMA examination of 9Cr-1Mo steel specimens for raw material, exposed for 10min and 30min

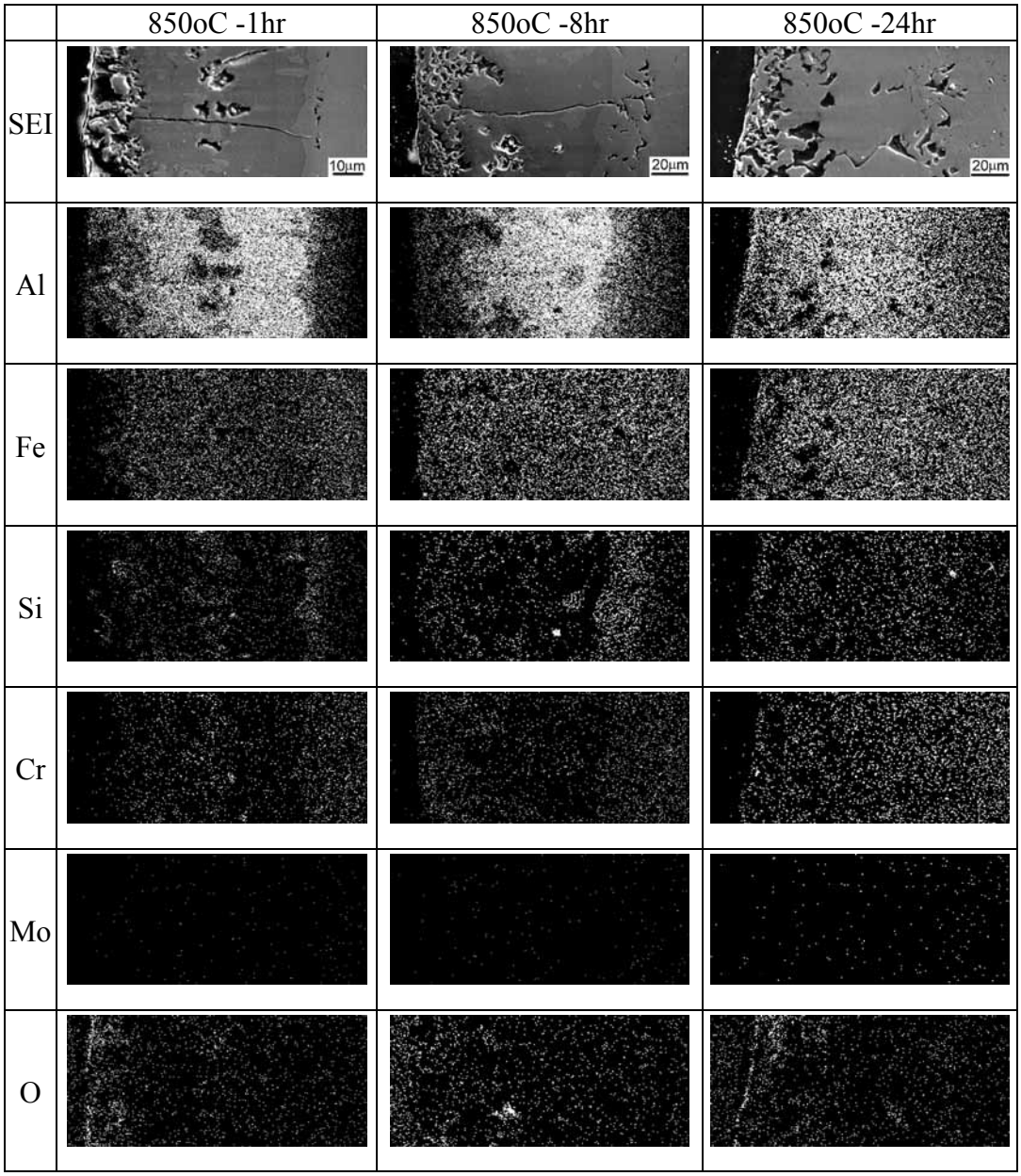

Fig. 37 EPMA examination of 9Cr-1Mo steel specimens for exposed for 1hr, 8hr and 24hr

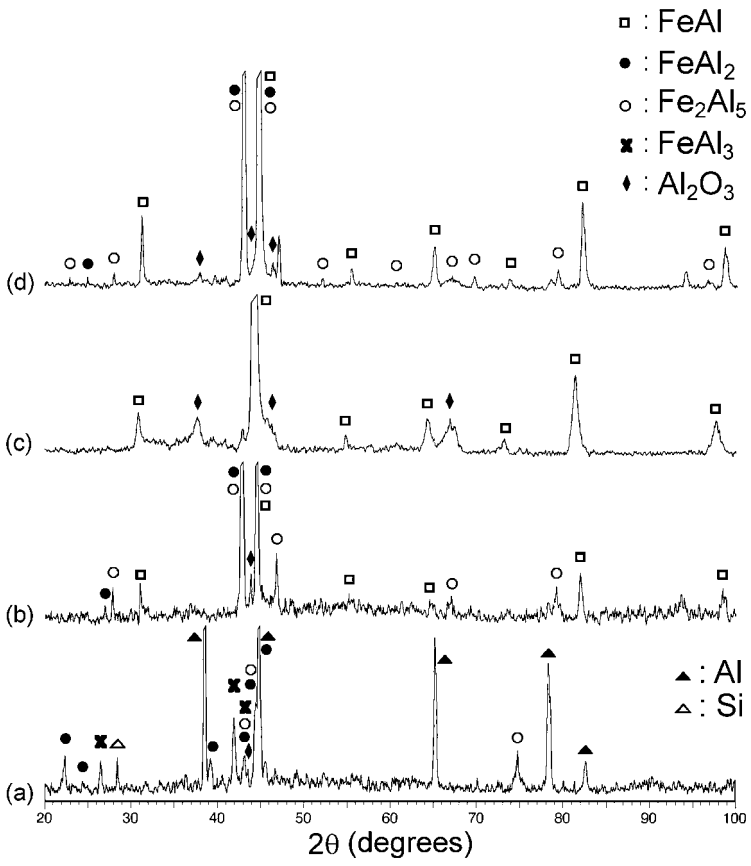

Fig. 38 9Cr-1Mo steel oxide surface phase spectrums. (a) 850°C-10min; (b) 850°C -60min; (c)850°C-24hr; (d)750°C-8hr, where 850°C-10min is similar to HD-raw; 750°C-8hr is similar to750°C-24hr

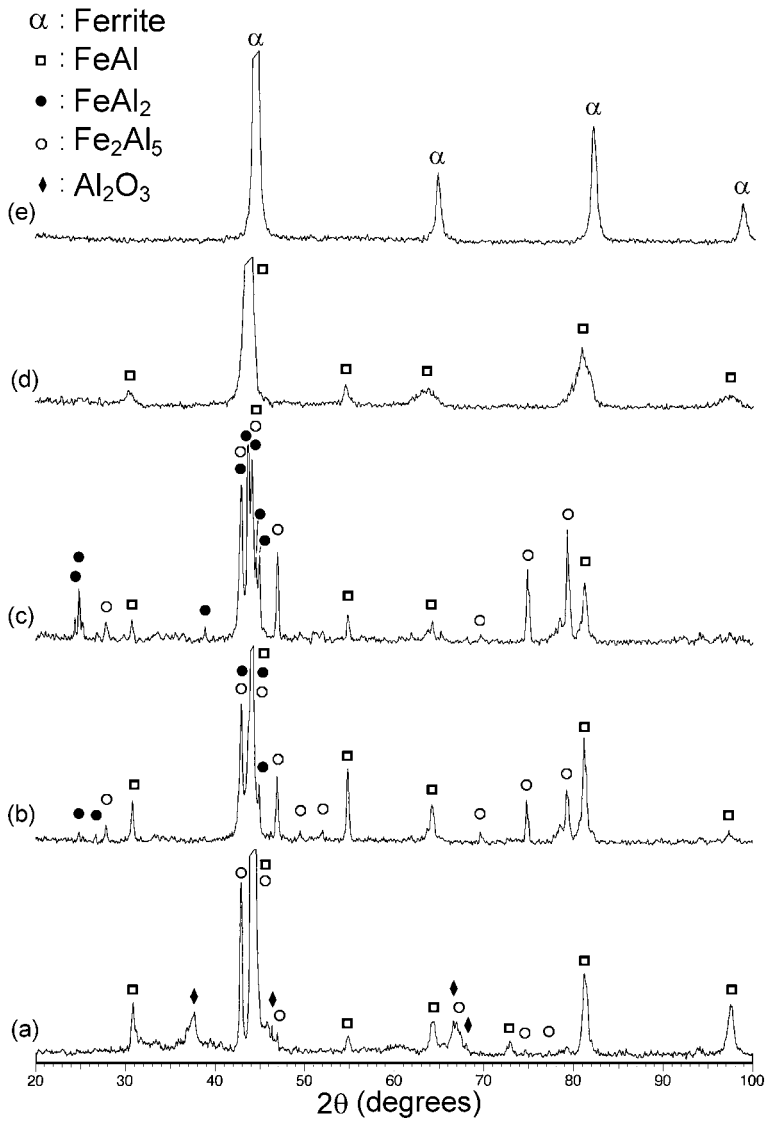

Fig. 39 9Cr-1Mo steel phases spectrums at 850°C for 8hr from (a)surface to (e)substrate

The weight change as function of exposure time for aluminide steel oxidized at various temperature is shown in Fig. 30. The result shows that the oxidation rate increased with increasing temperature. In the initial oxidation stage, the oxidation rate was controlled by the air/coating interface reaction, presenting a rapid increase of the weight gain. The controlling step gradually changed to diffusion when a protective Al_2O_3 scale was formed. The oxidation rate followed the parabolic law. The oxidation process changed from the original direct reaction between aluminum and air into the diffusion reaction of outward metal cations and inward oxygen anions through the oxides. In addition, the oxide scale became more and more compact due to its lateral growth. Hence, the oxidation rate was very low and the weight gain almost remaining constant as shown in Fig. 29 at 750°C and 850°C.

However, oxide scale failed at 950°C. The higher temperature of 950°C improved the Fe/Al inter-diffusion, increased the scale growth rate, resulted in scale lateral growth and the fast growth of the aluminide layer. The Fe-Al intermetallic compound of the aluminide layer changed to Al content ferrite readily within 8hr of exposure. The expansion coefficient differences during the heating process between the aluminide layer and the oxide scale caused a high stress accumulation, leading to the formation of scale cracks. Thus, increase of mass gain following a quasi-linear rate law is a result of the breakdown of the protective oxide scale. The oxidation kinetics are quasi-linear because of repeated cracking, subsequent oxidation of the free metal surface and healing as shown in Fig. 29. This coincides with the hypothesis that the oxide layer partly cracked and the metal surface was oxidized forming oxide leading to additional mass

gain. The aluminide steel has highest weight gain at 950°C respect to exposed temperature 750, 850 and 950°C.

2. Intermetallic compounds and voids

Voids and cavities are formed along the grain boundary and beneath the oxide scale as Fig. 33, Fig. 34 and Fig. 35 due to oxidation consumption and inward diffusion of Al. The cavities lead to decreased oxide adherence and increased spall of the scale. When formed at grain boundaries, the cavities and channels may allow intergranular oxidation. Severe internal oxidation is observed if no protective scale is formed due to impurities from the atmosphere.

In addition, many vacancies formed and gradually condensed together along the scale-alloy interface as shown in Fig. 40(j) and Fig. 40(l) while 9Cr-1Mo steel exposed for 24 hr at 850^{o}C and 56 hr at 750^{o}C. This phenomenon is even more obvious as exposed over 56 hr. The mechanism of void formation was attributed essentially to the Kirkendall effect[101] where the different Fe and Al diffusion rates can cause a net flux of vacancy to the scale-alloy interface, which condenses out into voids.

Based on the results of chemical, microstructure and XRD analyses, a schematic configuration for the stages of growth of the aluminized layer and internal void with oxides during oxidation at high temperature is depicted as shown in Fig. 41. In the initial 10 minutes, the as-coated steel composed of two layers as Al and Fe-Al intermetallic compounds. The Fe-Al intermetallic compounds consist of $FeAl_3$, Fe_2Al_5, and $FeAl_2$. The $FeAl_3$ layer is initially formed at the interface between the aluminum and steel substrate by iron atoms diffused into the aluminum layer, and the Fe_2Al_5 layer is then

formed at the interface between the $FeAl_3$ layer and steel substrate. The aluminide layer was dominated by Fe_2Al_5, and $FeAl_2$ after the topcoat aluminum disappeared.

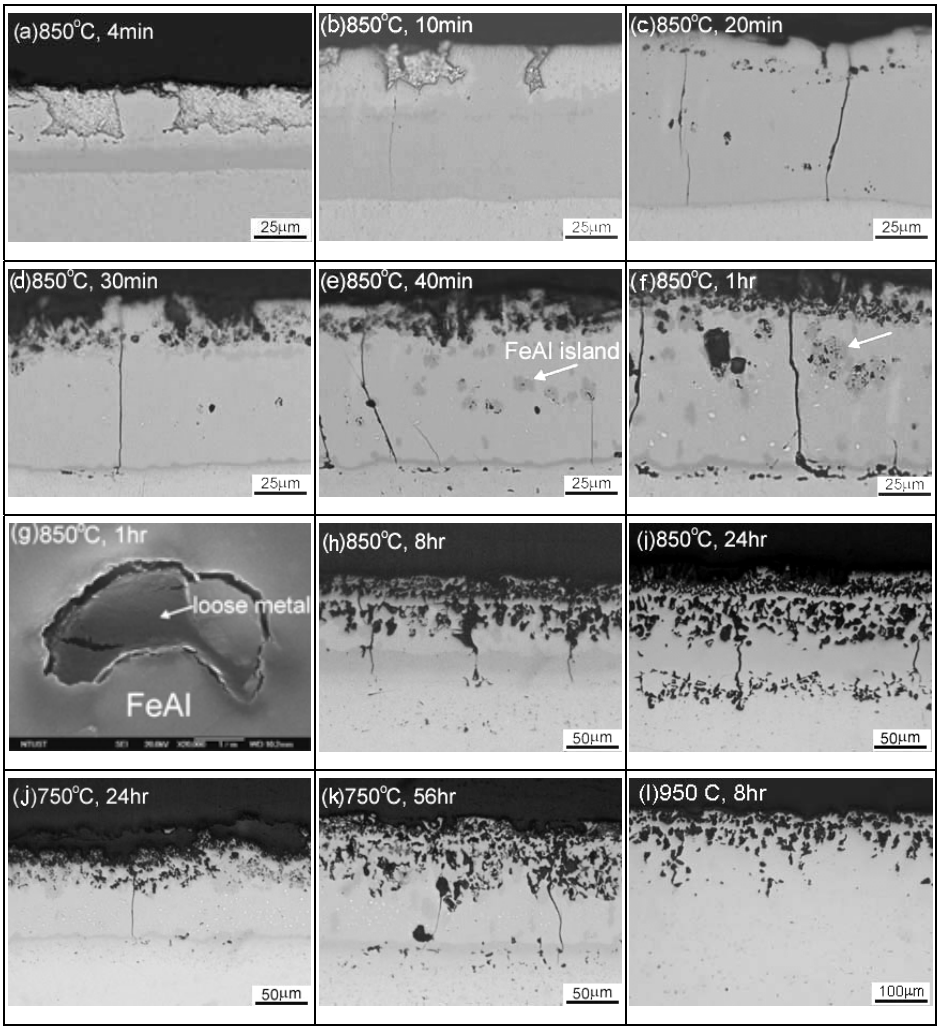

Fig. 40 Optical cross-sectional micrographs except g (g: SEI cross- sectional micrograph, high magnification of FeAl island) of 9Cr-1Mo steel corroded from 4min to 56 hr at 750, 850, and 950°C

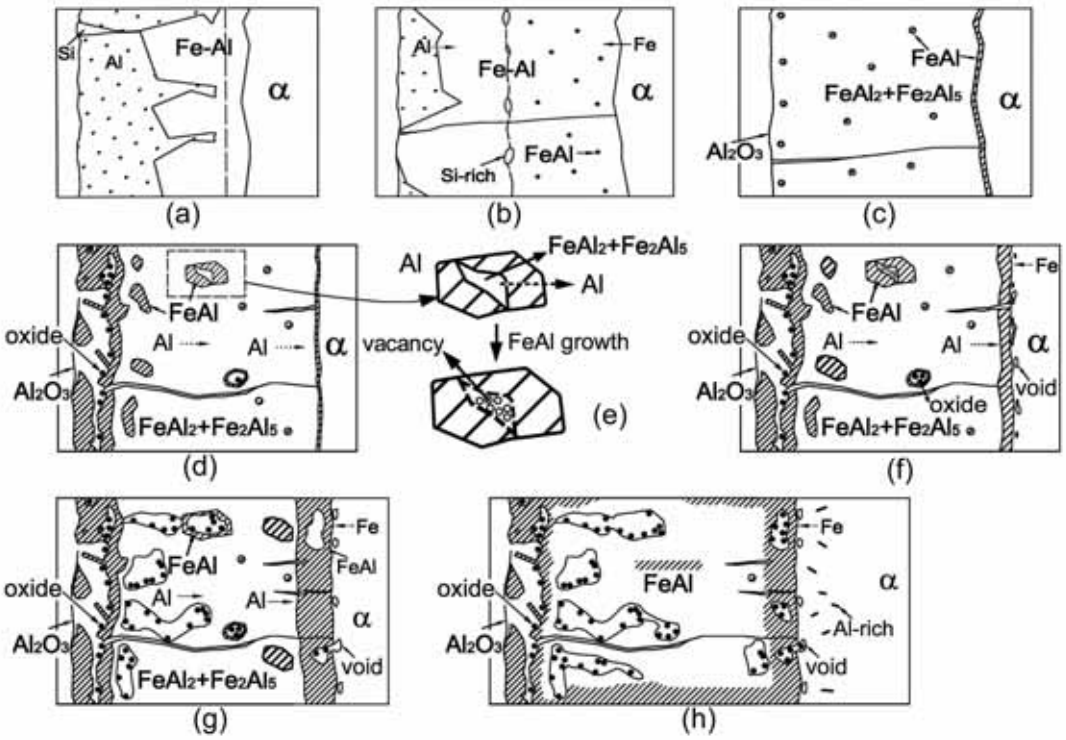

Fig. 41 Schematic configuration for the stages of growth of aluminized layer and internal voids during oxidation at high temperature. (a) as-coated steel, where Fe-Al consists of $FeAl_3$, Fe_2Al_5, and $FeAl_2$ (1 to 10 min). (b) the growth of the aluminized layer and crack formation (~10 to 30 min). (c) the growth of $FeAl_2$+Fe_2Al_5.(0.3 to 8 hr) (d) the growth of the FeAl phase (0.5 to 56 hr). (e) vacancies formation in $FeAl_2$+Fe_2Al_5. (f) internal voids and oxides formation. (g) the growth of voids and FeAl in the inner layer. (h) the growth of the FeAl phase through the entire aluminized

The aluminized layer grows and some cracks is appear during the 10 to 30 minute period. The growth of $FeAl_2$ and Fe_2Al_5 is widespread due to Al diffusion inward and Fe diffusion outward after the 8 hr. Eventually, the growth of the Fe_xAl_y phase is

dominant and all Fe-Al phases convert into the equimolar FeAl phase. This is consistent with the Fe-Al phase diagram as shown in Fig. 42.

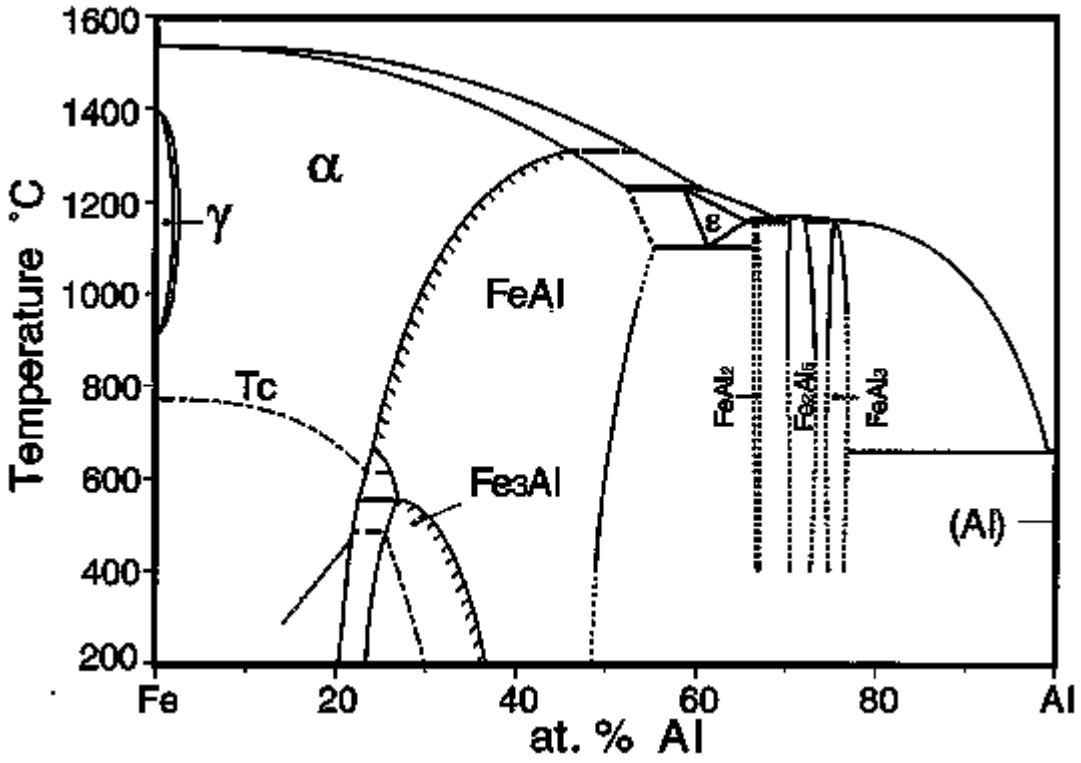

Fig. 42 The Fe-Al phase diagram

On the other hand, the crack formed in the intermetallic compounds due to the expansion coefficients different as shown in Fig. 40. The thermal expansion mismatch at the interface between the brittle Fe_2Al_5 + $FeAl_2$ layer and the steel substrate causes a tensile stress to be generated in the Fe_2Al_5 + $FeAl_2$ layer during heating and cooling, leading to the formation of cracks. Thus, when the aluminide layer was composed of Fe_2Al_5 and $FeAl_2$, the number of cracks in the aluminide layer increased rapidly. As the oxidation time is increased, voids and cavities formed beneath the Al_2O_3 scale as

shown in Fig. 40(e) and Fig. 41(d) due to oxidation consumption of Al and inward diffusion of Al.

On the other hand, the outward Fe diffusion caused unstable Fe_2Al_5 + $FeAl_2$ phases, leading to the precipitation of FeAl(Cr,Si), scattering in the intermetallic layer as shown in Fig. 40(f) and Fig. 41(d). The FeAl layer growth with increasing time also can be found at the intermetallic/substrare interface. When the FeAl island in the Fe_2Al_5 + $FeAl_2$ layer became larger gradually, some loose metals with similar composition to surrounded FeAl are observed on it as shown in Fig. 40(e-g) and Fig. 41(e), while some voids condense along the interface between FeAl intermetallic compound and the steel substrate as shown in Fig. 40(f) and Fig. 43.

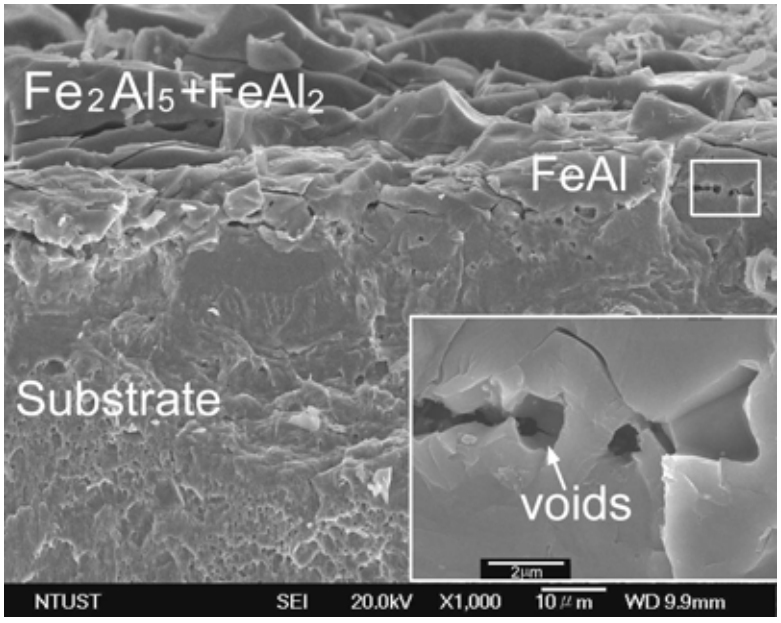

Fig. 43 SEI fractograph of the impact-fractured 9Cr-1Mo steel specimen after exposure for 1hr at 850°C

The formation of loose metals in the FeAl island can be explained as follows. Fe_2Al_5 + $FeAl_2$ surrounding by precipitated FeAl. Fe_2Al_5 + $FeAl_2$ transfers into FeAl along with some vacancies generated in the this area due to Al in the Fe_2Al_5 + $FeAl_2$ diffusing outward into FeAl phase. The metal surrounded by the coalesced vacancies became loose as Fig. 40(e) and evidenced as Fig. 40(g). Thus, after specimen grinding and polishing, the loose metals fell and a hollow feature could be observed in the FeAl island locally through cross sectional morphology.

After long-term exposure such as oxidation for 24hr at 850°C, the FeAl phase was dominant. All Fe-Al phases convert into FeAl phase, voids coalesce, oxygen penetrates into aluminide layer through cracks and voids, and internal oxides were formed as shown in Fig. 33(g). The combined results of EPMA examination (Fig. 37) and XRD analysis (Fig. 38) show that the oxides exist on the outer surface and in some internal voids. The elements Fe, Al, Cr, and Si spread over the aluminide layer uniformly.

The cross-sectional morphologies and phase constitutions of aluminide layer oxidized for 24hr and 56hr at 750°C (Fig. 33(j-k)) were analogous with that seen in the 8hr at 850°C. Similarly, the cross-sectional morphology and phase constitutions of aluminide layer oxidized for 8hr at 950°C were analogous with that seen in 56hr at 850°C, where the dominant phase is an Al content ferrite and the Fe-Al intermetallic was hardly detected by XRD analyses. We suggest that the higher temperature increases the Fe/Al inter-diffusion rates and the intermetallic phase transformations.

E. Summary of HDA on 9Cr-1Mo Steel

The aluminide coated 9Cr-1Mo steel shows good oxidation resistance up to 850°C

while the alloy traditional only can be used under 650°C. The thickness of the aluminide layer increased readily with increasing oxidation duration, regardless of temperature. The higher temperature increases the Fe/Al inter-diffusion rate and intermetallic phase transformation. At 950°C, the fast growing aluminide layer has a different expansion coefficient than oxide scale, leading to scale cracking, oxygen penetration, and internal oxidized, evidenced by a rapid mass gain.

Immediately after hot-dip Al-Si treatment of 9Cr-1Mo steel, the typical phase constitution was an aluminum topcoat and Fe_xAl_y intermetallic compounds with dissolved Si and Cr on the steel substrate. At elevated temperatures, the aluminide layer was converted to Fe_2Al_5 and $FeAl_2$. The number of cracks in this layer increased rapidly overtime. As the duration increased further, Fe_2Al_5 + $FeAl_2$ changed to FeAl and voids formed in the aluminide layer and at the FeAl/substrate interface.

The iron aluminum compounds $FeAl_3$, Fe_2Al_5, and $FeAl_2$ were initially formed between the coating layer and the substrate. At 850°C, the Fe_xAl_y layer thickness increases dramatically during the first 20min. Fe_2Al_5 mixed with $FeAl_2$ became the main phases in the coating layer. After 24hr, at 850°C, all $FeAl_2$ + Fe_2Al_5 transformed to FeAl, while $FeAl_2$ + Fe_2Al_5 still existed at 750°C after 56hr. The oxidation kinetics followed a parabolic law at both temperatures. Some cracks formed after 10 min exposure due to the growth of brittle $FeAl_2$ and Fe_2Al_5. After 30 minutes, internal voids with oxides were present which I speculate due to the Kirkendall effect.

CHAPTER VI

THE EFFECT OF NaCl DEPOSIT AND THERMAL CYCLE ON AN ALUMINIDE LAYER COATED ON 9Cr-1Mo STEEL

A. Introduction

9Cr-1Mo steel is widely used as tubes for heat exchanger. The low-grade fuels with sulfur, alkali salts, or vanadium are mainly used for firing in industrial process, such as oil- and coal-fired power generation and the boilers of off-shore industrial rigs. Metals undergo hot corrosion when the sodium chloride from the ocean breeze mixes with Na_2SO_4 from the combustion process and deposits on hot-section components, leading to severe attack of the alloy substrate. The hot corrosion is commonly accompanied with the formation of a porous and non-protective oxide scale, which has been mostly attributed to the condensation of salts that attacks the protective oxide scale.

To improve corrosion resistance, surface coating or modification to produce a surface layer with more corrosion resistant is commonly used. Studies reported that Al_2O_3-forming alloys showed better corrosion resistance than Cr_2O_3-forming alloys in chlorine-containing environments such as Cl_2-Ar, Cl_2-O_2-Ar, HCl-O_2 and NaCl deposits. Moreover, the aluminide steel applies generally to the electric power, petrochemical industry and other energy conversion system due to the low cost and good performance, and many research activities have focused on it. There are many different aluminum-coating processes including hot dipping, thermal spray, pack cementation, slurry, cladding, electroplating, etc. On the basis of cost and feasibility in industrial processes, hot-dip aluminizing process (HDA), as surface treatment of alloys, is used.

Pervious studies pointed out that alloys with hot-dip aluminum coating reveal excellent corrosion resistance and the formation of a thin, slow-going alumina scale acting as a barrier is beneficial to long term exposure at high temperature. However, the dependability of hot-dip aluminum against chloride-induced degradation is rarely investigated. The purpose of this study was to investigate the effects of hot-dip aluminum with added 7%silicon against NaCl-induced accelerated oxidation in a thermal cycling environment.

B. Experimental procedure

A commercial cold rolled ASME SA213 T9 steel sheet was used as experimental materials in this study. The chemical composition of the alloy is Fe-0.09C-0.36Si-0.40Mn-0.02P-8.25Cr-0.93Mo-0.04Ni-0.01Cu-0.225V(wt.%). Rectangular specimens were cut to the dimensions of 15×10×2mm by water-cooled cutting machine. Specimens for further hot-dip treatment were hung by stainless steel wires and coated with uniform weld flux. Specimens were dried and immersed in a aluminum-silicon (Al-7%Si-0.3%Mg-0.2%Fe-0.2%Cu in wt.%) molten bath at 700°C for 16 seconds. Silicon was added into the aluminum liquid in order to make the surface of the Fe-Al alloy layer smooth and enhance the interfacial bonding strength. The up and down speed was 18cm/min. Then the hot-dipped specimens were cleaned by a mixed aqueous solution of nitric acid, phosphoric acid, and water in 1:1:1 volume fraction at 60°C. The thickness of external aluminum coating and aluminized layer was 25μm after hot-dip treatment.

Prior to thermal cycling test, specimens with and without hot-dip treatment (un-

coated steel) were deposited with NaCl until a total depositing weight of 2 mg/cm^2 was reached. The specimens were weighed and measured first, and then placed on a hot plate heated to 110°C. An air gun sprayed saturated aqueous-salt solutions in an air mist, and a coat of fine salt particles formed on the specimen surface after the mist settled and the water evaporated. The process was repeated until the dry particles were deposited up to 2mg/cm^2. Cyclic depositing-heating test was performed. Specimens with a NaCl deposit was exposed in a furnace with static air at 750 and 850°C for 8 hr and then air-cooled. After cooling to room temperature, corroded specimens were re-sprayed with NaCl and heated to elevated temperature. The heat pattern was repeated for a maximum of 7 times. In order to compare the effect of deposited salt and thermal stress on the coated and uncoated steel, specimens with no salt deposit were employed in thermal-cycling test.

The corrosion products were analyzed by X-ray diffraction (XRD) using monochromatic Cu-Kα radiation operated at 40 KV and 100 mA. A sequential grinding technique was adopted to investigate the distribution of the different phases present in the scale and the alloy substrate. Characterization of the cross-sectional scales was carried out with optical microscopy (OM), scanning electron microscopy (SEM) and electron probe microanalysis (EPMA) with X-ray wavelength-dispersive spectrometry (WDS).

C. Results

1. 9Cr-1Mo Steel without HDA treatment

Fig. 44 show the typical microstructure of 9Cr-1Mo steel after polishing and etch-

ing. Fig. 44(b) shows the uncoated steel oxidized at 850°C for 7 thermal cycles without NaCl deposition. The scale, adherent on the steel surface for each cyclic test, consisted of Fe_2O_3, Fe_3O_4 and trace of FeO. The micrograph reveals that 9Cr-1Mo steel has a ferritic structure with a dispersion of carbide particles in a matrix. XRD analyses of the scales formed on the steel oxidized at 750 and 850°C for 1 cycle are shown in Fig. 45(a,b). It reveals that the scale formed on the steel consisted of mostly Fe_2O_3 and Fe_3O_4 at both temperatures. Surface topographies of the steels oxidized at 750 and 850°C for 1 cycle are shown in Fig. 46(a,b). At 750°C some prominent crystals, Fe_2O_3 with dissolved Cr and Mn, could be observed on Fe_2O_3 scale, and plate-like chromium oxides with dissolved Fe generated among the crystal-like Fe_2O_3 (dissolved Cr and minor Mn) at 850°C. Fig. 44(b) shows the uncoated steel oxidized at 850°C for 7 thermal cycles without repeated NaCl deposition. The scale formed on steel was adherent and no scale spalling occurred during each cyclic test. For the NaCl deposition tests, a thick scale was generated on the surface. Fig. 44(c) shows a typical cross-sectional micrograph of steel with NaCl deposit exposed at 850°C for 8hr. The results of XRD analyses (Fig. 45(c,d)) reveal that the outermost scale consisted of Fe_2O_3 and the inner scale consisted of Fe_3O_4 (dissolved Cr) and FeO. Surface topographies of steel corroded at 750 and 850°C for 1 cycle are shown in Fig. 46(c,d). Fe_2O_3 was the main phase presenting on the scales' surface, where grain-like Fe_2O_3 appeared at 850°C and pompon-like Fe_2O_3 formed at 750°C. The scales formed on the steel with NaCl deposition can be removed easily after each thermal cycle test.

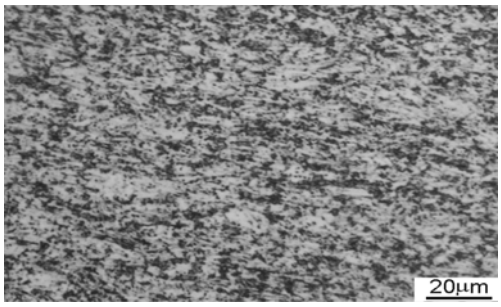

(a)

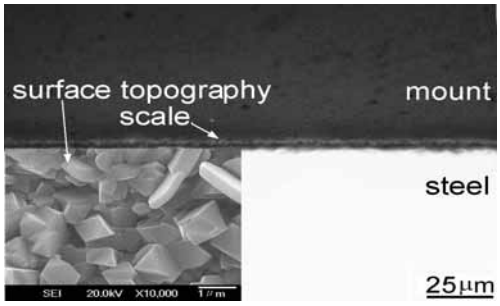

(b)

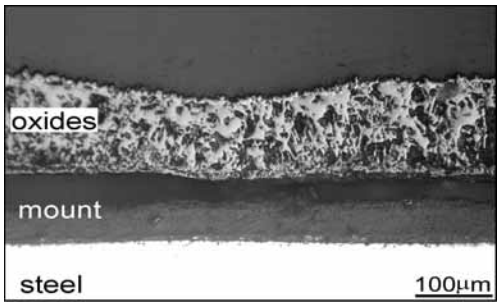

(c)

Fig. 44 (a)Microstructure of annealed 9Cr-1Mo steel, (b) 9Cr-1Mo steel with neither HDA nor NaCl deposit oxidized at 850°C for 7 thermal cycles, (c) uncoated 9Cr-1Mo steel with 2mg/cm^2 NaCl deposit exposed at 850°C for 8 hr

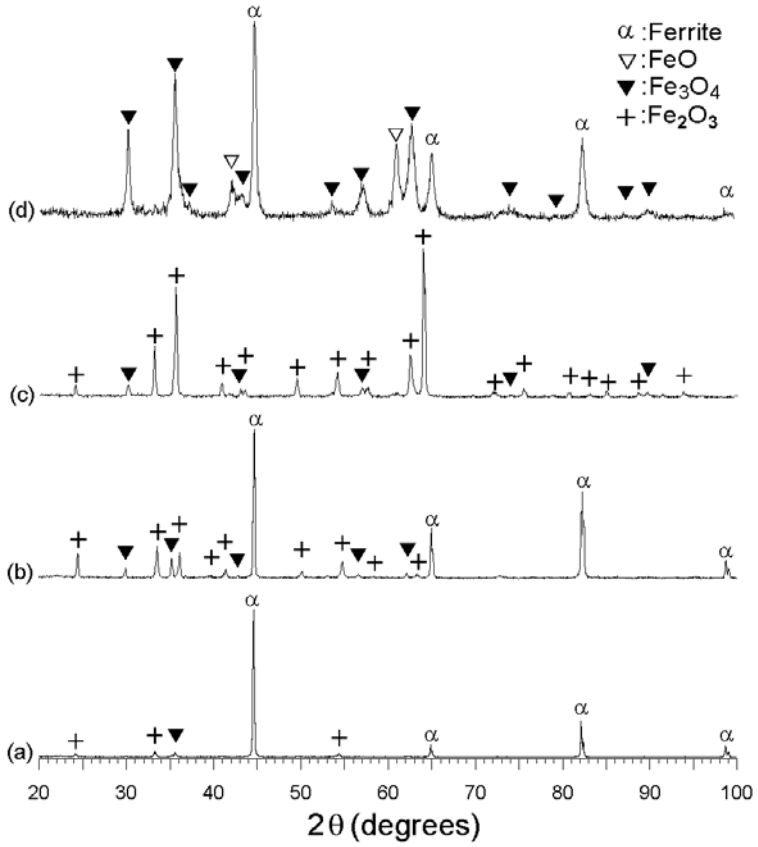

Fig. 45 XRD analysis of uncoated 9Cr-1Mo steel exposure for 8 hr. (a) without NaCl deposit at 750°C; (b) without NaCl deposit at 850°C; (c) outer surface of steel with NaCl deposit at 850°C; (d) same as (c) after careful grinding for removing the external layer

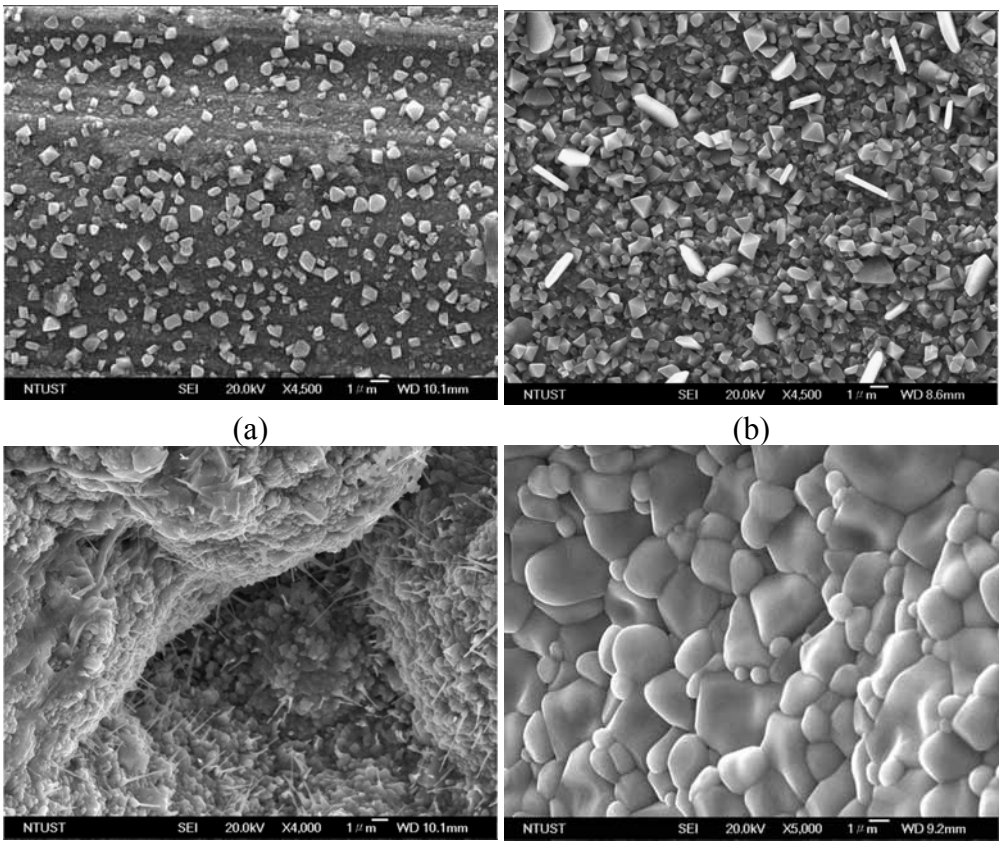

Fig. 46 SEI surface topographies of 9Cr-1Mo steel without Al-Si coating exposed for 8 hr. (a) at 750°C without NaCl deposit, (b) at 850°C without NaCl deposit, (c) at 750°C with NaCl deposit, (d) at 850°C with NaCl deposit

2. Oxidation of 9Cr-1Mo steel with hot-dip Al-7%Si coating

The Surface topographies of coated steel oxidized at 750 and 850°C for 1 cycle without NaCl deposit are shown in Fig. 47(a,b). Thin Al_2O_3 scale formed on the surface of the aluminide layer at both temperatures. Fig. 48 shows typical cross-sectional micrographs of the specimens after exposure for various thermal cycles at 750 and 850°C, separately.

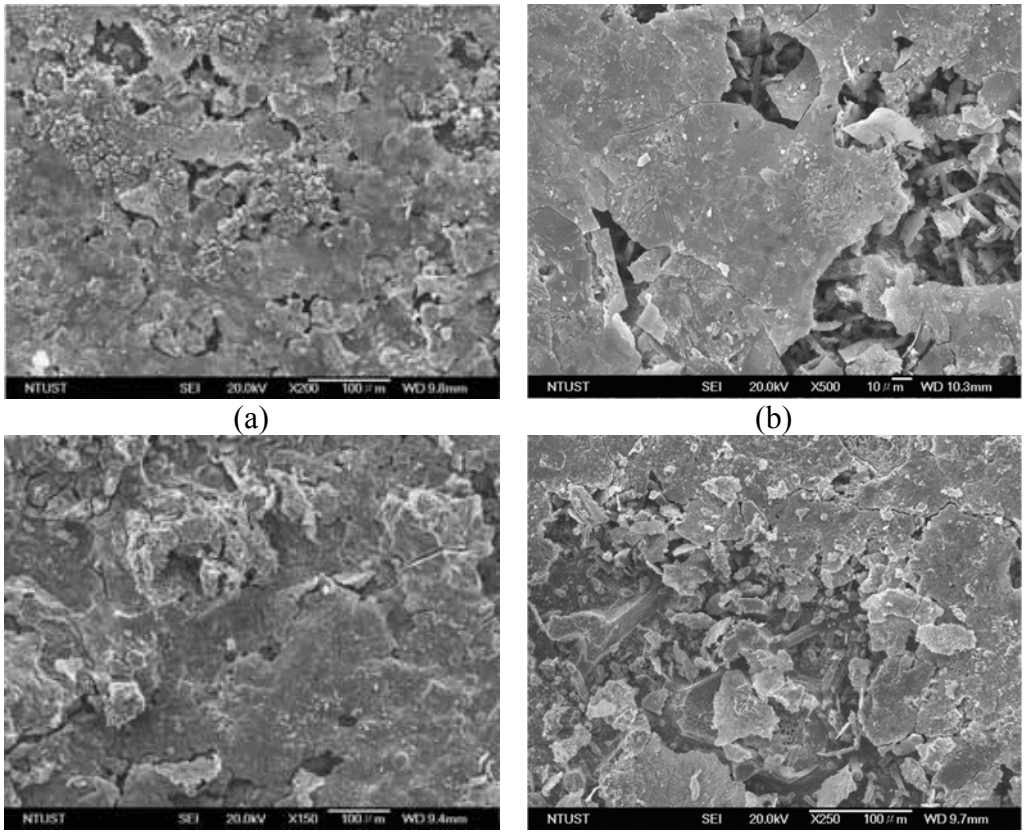

Fig. 47 SEI surface topographies of 9Cr-1Mo steel with Al-Si coating exposed for 8 hr. (a) at 750°C without NaCl deposit, (b) at 850°C without NaCl deposit, (c) at 750°C with NaCl deposit, (d) at 850°C with NaCl deposit

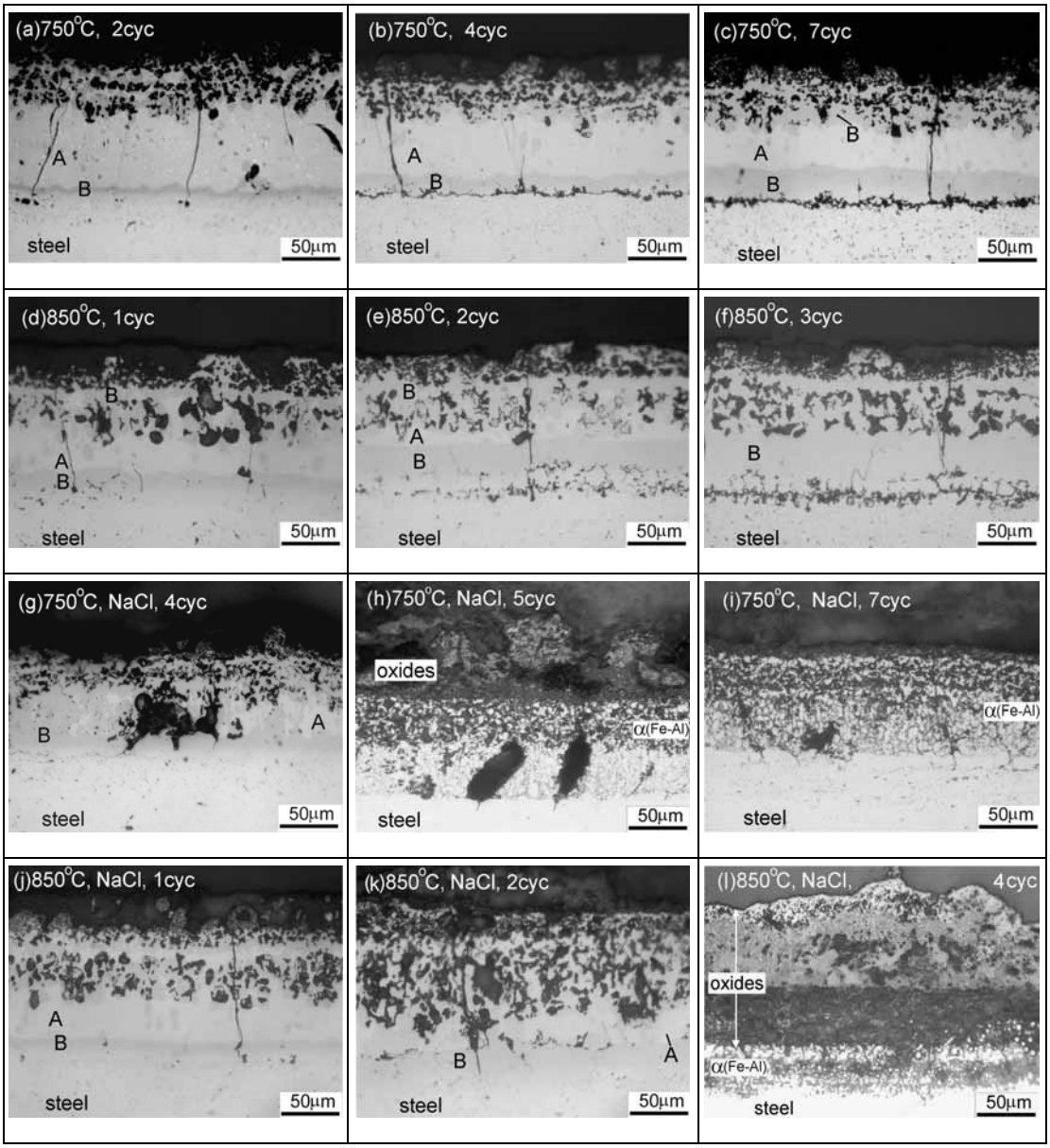

Fig. 48 Optical cross-sectional micrographs of coated 9Cr-1Mo steel exposure from 1 to 7 cycles at 750 and 850°C, where A represents $FeAl_2$+Fe_2Al_5; B represents FeAl. ((a)~(f): steel coated with Al-Si without NaCl deposit; (g)~(l): steel coated with Al-Si and deposited with NaCl)

For oxidation tests without NaCl deposition, the thickness of aluminide layer remained constant and cracks formed in the aluminide layer in all cases, regardless of temperature and thermal cyclic times. The intermetallic compound layers in the aluminide were denoted by A and B. Fig. 49 shows the results of XRD analyses of a specimen without NaCl deposit tested at 850°C for 1 cycle.

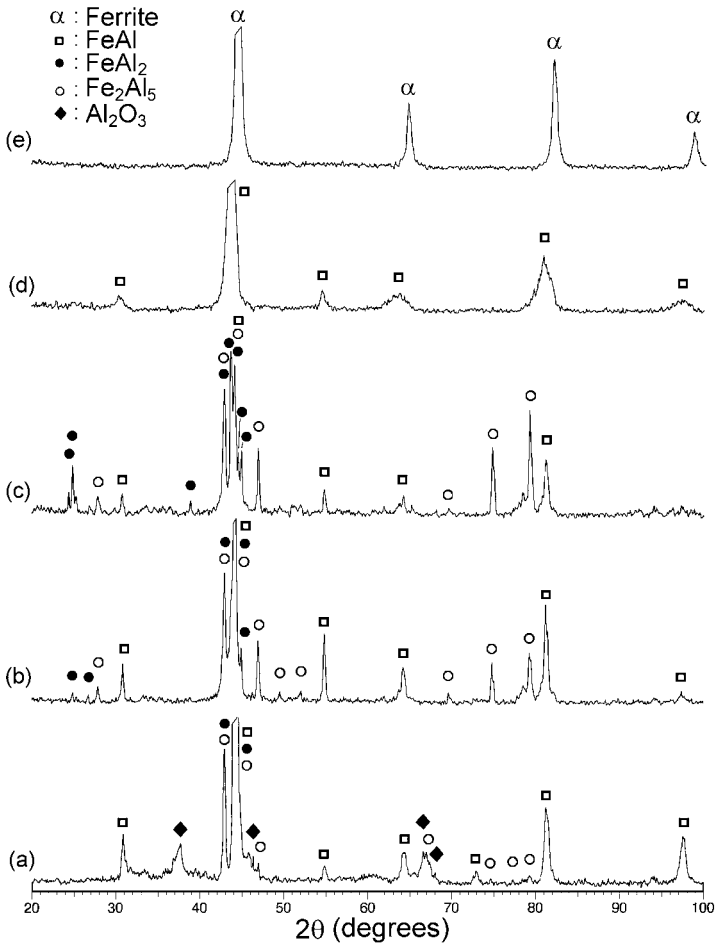

Fig. 49 XRD analysis of Al-Si coated 9Cr-1Mo steel without NaCl deposit tested for 1 cycle at 850°C, detecting from (a)surface to (e)the steel substrate

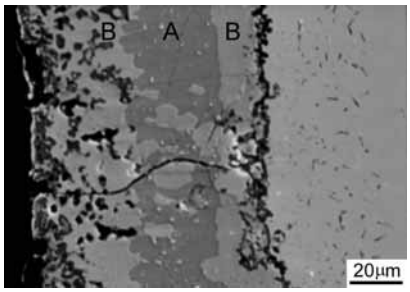

(a) SEI

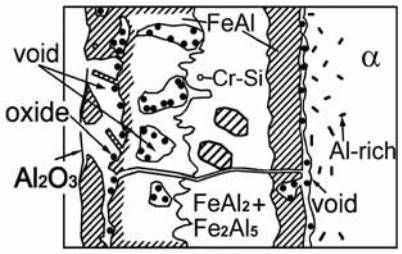

(b)

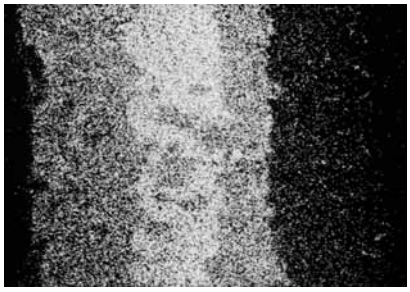

(c) Al

(d) Fe

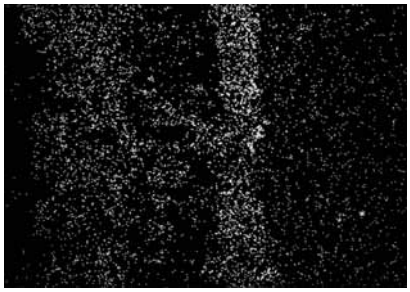

(e) Si

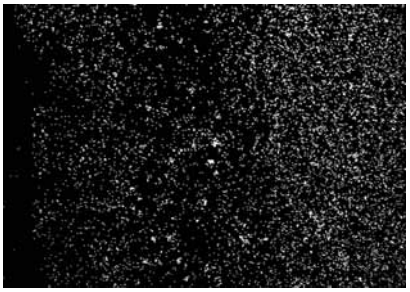

(f) Cr

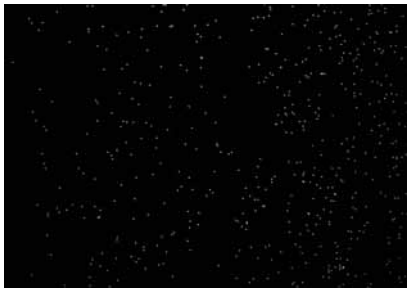

(g) Mo

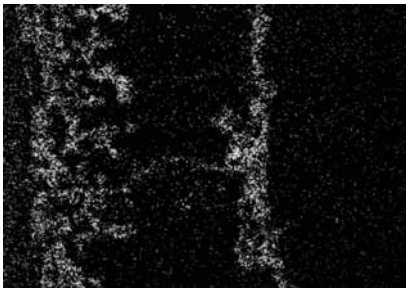

(h) O

Fig. 50 EPMA examination and the corresponding schematic configuration of Al-Si coated 9Cr-1Mo steel without NaCl deposit tested for 7 cycles at 750°C

Layer A exhibited an intense peak attributable to $FeAl_2$+Fe_2Al_5, while layer B showed a peak associated with FeAl. At both temperatures, the FeAl layer thickness increased and the internal voids near the aluminide layer/substrate interface grew readily with increasing cyclic times. The $FeAl_2$+Fe_2Al_5 phase decreased gradually with increasing cycles. At 750°C the $FeAl_2$+Fe_2Al_5 (layer A) could be observed till 7 cycles, while layer A disappeared entirely after 3 cycles at 850°C.

A typical cross-sectional SEI micrograph of coated specimen exposed at 750°C for 7 cycles and the corresponding X-ray maps as well as schematic configuration are shown in Fig. 50. The external oxide scale is thin. The distribution of layers A and B with dissolved Si and minor Cr could be obviously distinguished, and the cracks and the internal voids in the aluminide layer were filled with oxides. Al-rich phases precipitated in the steel substrate, while some Cr-Si phases generated in the layer A.

2. Corrosion of 9Cr-1Mo with hot-dip Al-7%Si coating

Fig. 47(c,d) shows surface topographies of Al-Si coated steel with an NaCl deposit after exposure at 750 and 850°C for 1 cycle. When compared to those without NaCl deposit, Al_2O_3 scale formed on the surface of the aluminide layer was thicker; the Al_2O_3 could be easily detected at both temperatures by XRD and EDS. The cross-sectional corrosion morphologies of the first cycle were similar to that without NaCl deposit at both temperatures.

However, the deposition of NaCl accelerated the void formation toward the steel substrate, especially at 850°C. The degradation of the aluminide layer occurred after 5

cycles at 750°C and 4 cycles at 850°C, where layer A and B disappeared and iron oxides formed on the surface. XRD analyses (Fig. 51) of the scale formed on the surface of the aluminized layer show that Fe_2O_3, Al_2O_3, NaCl, and ferrite are the main phases present on specimens.

A typical cross-sectional SEI micrograph of coated steel with NaCl deposit treated at 750°C for 2 cycles and the corresponding X-ray maps as well as concentration variations of Al, Fe, Cr, Si and O elements are shown in Fig. 52. There are five distinct layers that can be observed in the as-exposed coupon, scale, FeAl with voids, $FeAl_2$+Fe_2Al_5, FeAl, and ferrite, respectively. In addition, internal voids filled with oxides generated through cracks toward the steel substrate, and a loose alumina scale formed, where chlorides were detected in it.

With increasing numbers of cycles, Fig. 48(g-i) shows that $FeAl_2$+Fe_2Al_5 disappeared after 5 cycles. After 7 cycles the aluminized layers were replaced by ferrite, iron with dissolved Al at 750°C.

At 850°C $FeAl_2$+Fe_2Al_5 disappeared after 3 cycles and a thick external scale formed on the specimen after 4 cycles (Fig. 48(l)). EDS quantitative analysis of the scale and the aluminized layer (Fig. 53) after a 4 cycle test at 850°C reveals that the outermost scale consists of iron oxides and the rest consists of a large quantity of alumina oxides, where chlorides were detected inside the scale. The aluminized layer almost disappeared, where Al content in this layer is 8(at)%.

From the above observation, the NaCl deposition leads to accelerated-degradation of hot-dip aluminum-7%silicon coatings on the steel substrate, especially at 850°C.

Nevertheless, it was found that the aluminized layers were effective to improve the corrosion resistance in thermal cyclic environment.

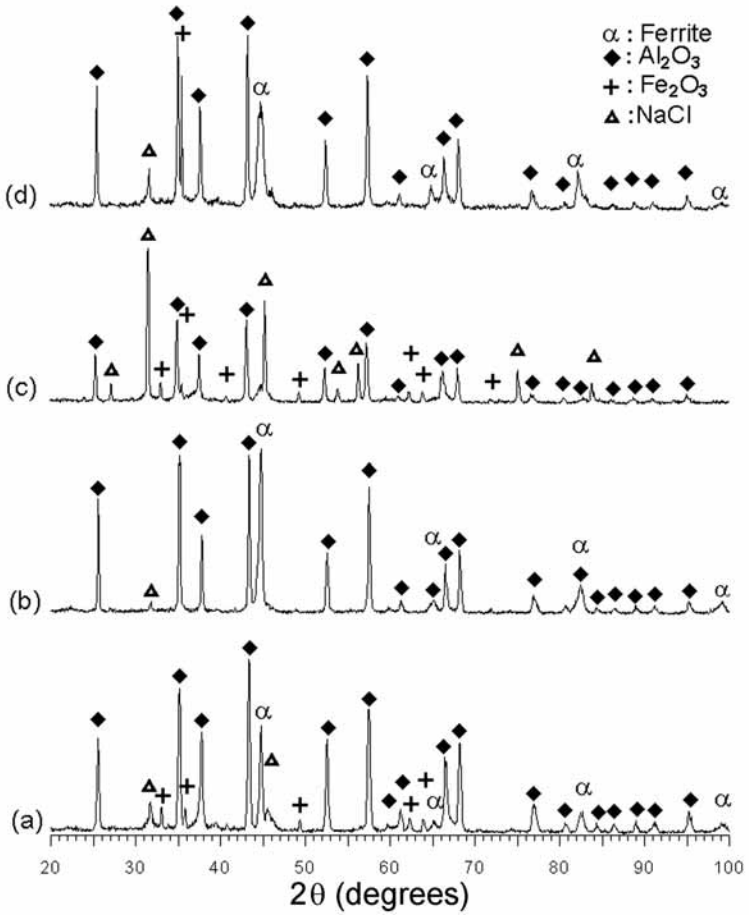

Fig. 51 XRD analysis of Al-Si coated 9Cr-1Mo steel with NaCl deposit, (a-b) tested for 4 cycles at 850°C; (c-d) tested for 5 cycles at 750°C, where (a)surface, (b)after scale partly removed, (c)surface, (d)after scale partly removed

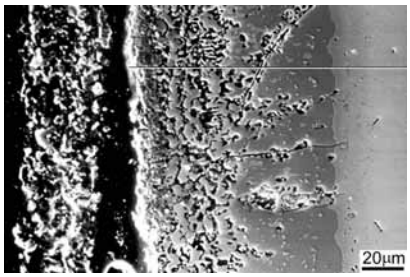

(a) 750°C-Air-2Cycle

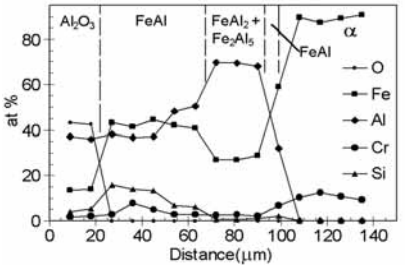

(b)

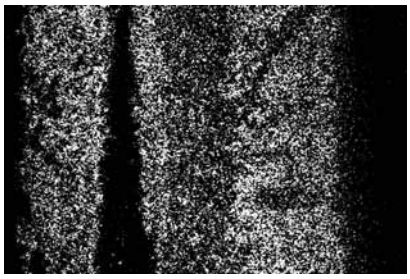

(c) Al

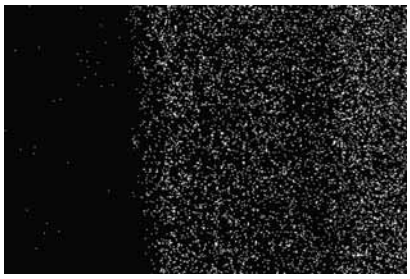

(d) Fe

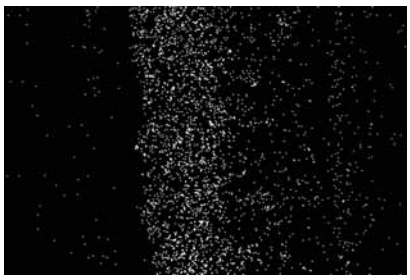

(e) Si

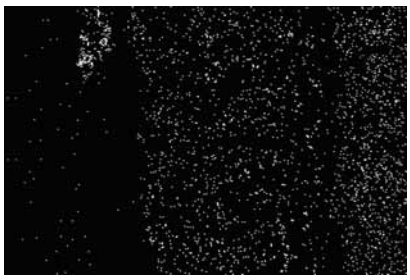

(f) Cr

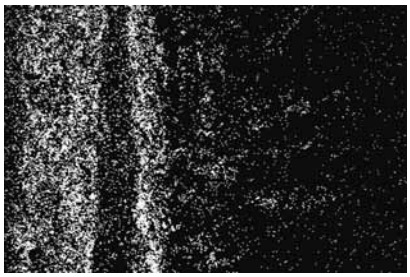

(g) O

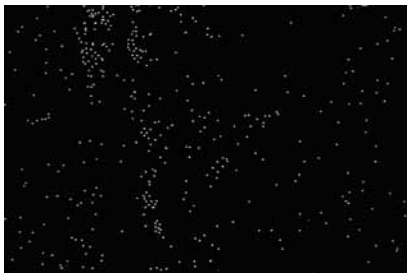

(h) Cl

Fig. 52 EPMA x-ray maps and the corresponding concentration variations of Al, Fe, Cr, Si and O elements of Al-Si coated 9Cr-1Mo steel with NaCl deposit tested for 2 cycles at 750°C

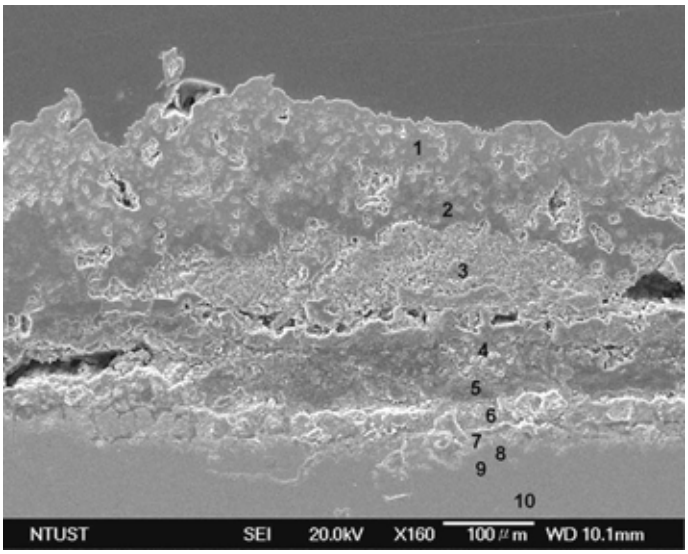

(a)

unit: at%

element / position	O	Al	Fe	Cr	Si	Cl	Na
1	45	-	55	-	-	-	-
2	44.2	42.6	5.6	7.6	-	-	-
3	34.4	30.7	4.6	-	-	25.2	5.1
4	59.1	29.4	7.	-	-	3.7	-
5	47.6	36.6	8.7	-	7.1	-	-
6	54.9	-	45.1	-	-	-	-
7	5.8	2.9	91.3	-	-	-	-
8	-	8.6	85.1	6.3	-	-	-
9	-	-	95.6	4.4	-	-	-
10	-	-	90.5	9.5	-	-	-

(b)

Fig. 53 (a) SEM micrograph showing the Al-Si coated 9Cr-1Mo steel specimen with repeated NaCl depositing exposed at 850°C for four thermal cycles, (b) EDS results of the concentration (at.%) of O, Al, Fe, Cr, Si, Cl and Na at positions 1~10

D. Discussion

Both Fe and Cr are easy reacting with O_2 to form oxides. When Cr concentration lower than N^*_{Cr} (approximately 12-Cr%), the critical solute concentration for the transition from internal to external oxidation, Cr_2O_3 can not be formed on the surface as shown in Fig. 26, which Cr concentration is about 25% over N^*_{Cr}. At low Cr content, iron oxides form on the top chromium-rich oxides as shown in Fig. 4(a). Some Cr will enter solution in the FeO phase but, due to the stability of spinel, the solubility is limited as in the case of Ni-Cr alloys. On increasing the Cr content, Fe^{2+} ions are progressively blocked by the $FeCr_2O_4$ islands and the FeO layer correspondingly becomes thinner relative to the Fe_3O_4 layer thickness. When Cr content is increased further, a scale of mixed spinel $Fe(Fe,Cr)_2O_4$ is produced. Apparently, iron ions are much more mobile in this oxide than Cr^{3+} ions since iron oxide can be found at the outer surface of the scale as shown in Fig. 54. It shows the comb-like Fe_2O_3 growths on the crystal-like Cr_2O_3. When the Cr concentration exceeds the critical concentration N^*_{Cr} (~12wt% or more), an initial outer layer of pure chromia is formed. However, to sustain the chromia layer over a long exposure time, a substantially larger amount of chromium is required.

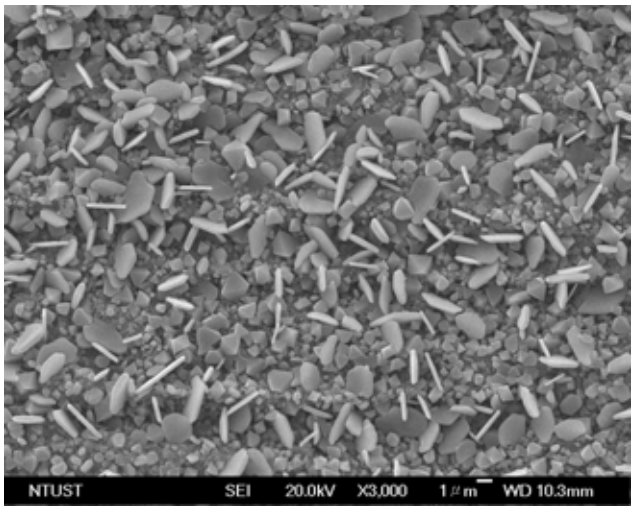

Fig. 54 SEI micrographs of scales formed on 9Cr-1Mo steel without Al-Si coating and NaCl deposit oxidized at 850°C for 1 cycles

Fig. 48(l) shows the typical cross-sectional micrograph of 9Cr1Mo steel with a NaCl deposit exposed at 850°C for 4 cycles. Here, the outermost scale consisted of Fe_2O_3 and the inner scale consisted of Fe_3O_4 and $FeCr_2O_4$. The scales formed on the steel with repeated NaCl deposition spalled away during each thermal cycle test. It shows NaCl accelerated the hot corrosion process. There are two kinds of mechanisms in the hot corrosion process with the limited thickness of NaCl deposition as shown in Figs. 55 and 56. The initial stage was predominated by the oxychloridation reaction when the NaCl still existed. The second stage, or the propagation stage, was predominated by the chloridation and reoxidation cyclic reactions when the NaCl was depleted. In the case of oxychloridation, the iron, aluminum or chromium would react with oxygen and NaCl to form metal oxide, sodium oxide and chlorine. Then the Cl_2 produced from the oxychloridation would react with iron, chromium and aluminum to form gas phase

metal-chloride. The metal-chloride evaporates, diffuses out and oxidizes with solute oxygen to form metal-oxide and chlorine. The released chlorine is returned back to the process again. Hence, during the cyclic reaction process, the chlorine acts as catalyst to accelerate corrosion.

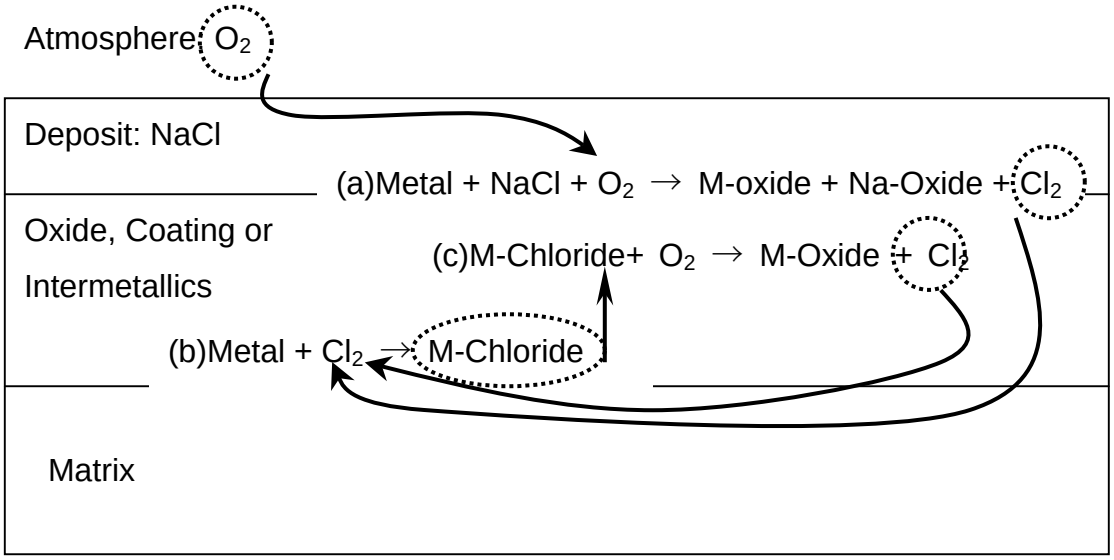

Fig. 55 A schematic illustration circulation of chlorine in active oxidation mechanism. Where (a) is oxychloridation process, (b) is chloridation process, and (c) is re-oxidation process

For specimens with the hot-dipped aluminum coating, the compact, protective Al_2O_3 layer separated the metal from molten salt. This inhibited the formation of chlorine from the oxychloridation reactions during the initial stage. Therefore, the reaction rate during the propagation stage was also reduced for the lack of chlorine. As a result, the aluminum coating improved the hot corrosion resistance for 9Cr1Mo steel. However, the post pre-oxidation of aluminum coating caused the dilution of aluminum con-

tent and the over growth of the alloying layer by means of Al/Fe interdiffusion. The post preoxidation of the aluminum coating showed a detrimental effect on the NaCl-induced hot corrosion.

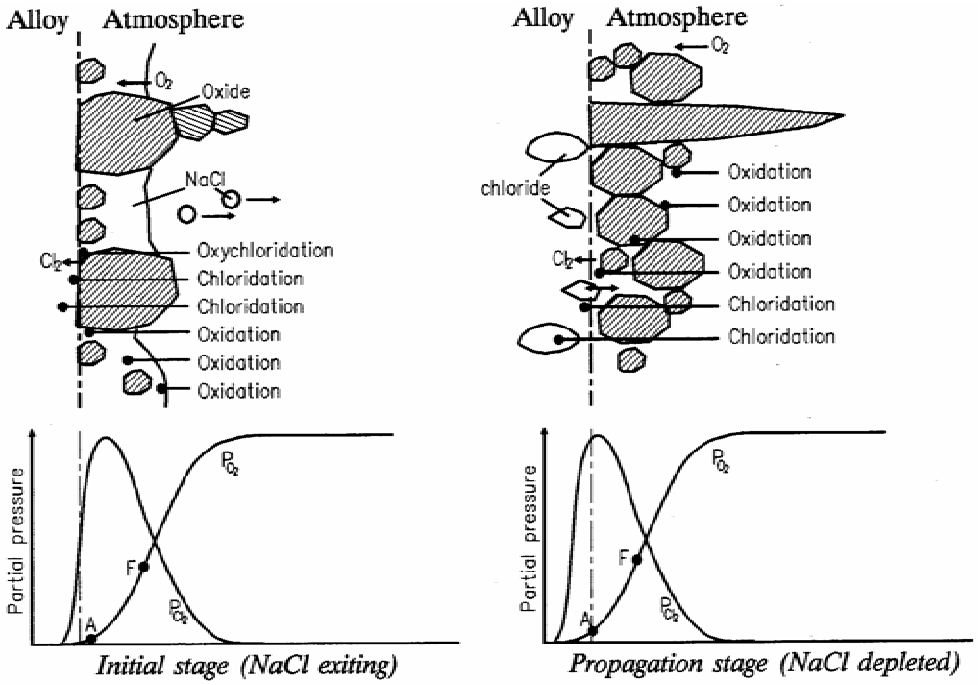

Fig. 56 Mechanism of aluminum coating protection

Microcracks were formed in the brittle alloying layer during the cyclic heating/cooling process. The microcracks provided opportunity for deposition and short cut diffusion paths for the molten salt, the metals and metal chlorides. The microcracks formed during the first cycle and grew rapidly during repeated cooling and heating process as shown in Fig. 48.

The formation mechanisms for cracks, voids and cavities are same as explained in chapter V. The cracks formed in the intermetallic compounds due to the expansion co-

efficients different as shown in Fig. 48. The thermal expansion mismatch at the interface between the brittle Fe_2Al_5 + $FeAl_2$ layer and the steel substrate caused a tensile stress to be generated in the Fe_2Al_5 + $FeAl_2$ layer during heating and cooling, leading to cracks.

Voids and cavities are formed along the grain boundary and beneath the oxide scale, as Fig. 48, due to oxidation consumption and inward diffusion of Al. The cavities lead to decreased oxide adherence and result in spall off the scale. The rate of spall increases with increasing number of thermal cycles.

On the other hand, the oxides at the voids condensed at the interface between intermetallic compounds and the matrix obstruct the aluminide layer growth. The oxides were formed by oxygen reacting with the Al, Fe, or Cr through cracks connecting with the voids. It is noticed that the aluminide layer almost keep the same thickness when voids condensed together as shown in Fig. 48(b) and (c).

E. Summary of HDA on 9Cr-1Mo steel with thermal cyclic process

1. There are two kinds of mechanisms in the hot corrosion process with thin NaCl deposition. The initial stage was predominated by the oxychloridation reaction when the NaCl still existed. The second stage, or the propagation stage, was predominated by the chloridation and reoxidation cyclic reactions when the NaCl was depleted.
2. For specimens with the hot-dipped aluminum coating, the compact, protective Al_2O_3 layer separated the metal from molten salt. This inhibited the formation of chlorine from the oxychloridation reactions during the initial stage. Therefore, the reaction

rate during the propagation stage was also reduced for the lack of chlorine. As a result, the aluminum coating improved the hot corrosion resistance for low 9Cr1Mo steel.

3. The thermal cyclic process will increase the microcracks formed due to repeat cooling and heating. The microcracks provide a deposition position and diffusion paths for the molten salt and the metals. These increase the hot corrosion rate.

CHAPTER VII

CONCLUSIONS

The summary of study discovery is shown in Tables 4 and 5. My hypotheses that the corrosion rate of 310SS will increase with increasing NaCl concentration and temperature were supported by my experiment results. The high density Al-Si depositing on the surface of 310SS showed an increased corrosion resistance due to formation of protective Al_2O_3 oxide scale, and the internal voids at the intermetallics and interface are due to the phase transformation and Kirkendall effect.

The mechanism of NaCl induced corrosion is the oxy-chloridation, chloridation and re-oxidation process. There are two stages in the hot corrosion process with NaCl deposition. The first stage is predominated by the oxychloridation reaction as NaCl deposited on the alloy surface. When the NaCl was depleted, the process transfers to propagation stage, which is predominated by the chloridation and reoxidation cyclic reactions. The NaCl plays as a catalyst accelerating the corrosion reaction.

The mechanism of hot-dipped aluminum coating is due the formation of a compact, protective Al_2O_3 layer, which separated the contact of metal from molten salt and thus inhibited the formation of chlorine from the oxychloridation reactions during the initial stage. As a result, the aluminum coating improved the hot corrosion resistance. However, when the protective coatings break down, the corrosion behavior is similar to that observed in uncoated control specimens.

Thermal cyclic process increases the formation of microcracks due to repeat cool-

ing and heating. The microcracks provided deposition position and short cut diffusion paths the molten salt and the metals. Consequently, it leads to increase hot corrosion rate.

The corrosion caused by 100% Na_2SO_4 coating shows incubation period characteristics. The corrosion rate of 100% Na_2SO_4 coating is many orders of magnitude lower than that of 100% NaCl and its mixtures over the 24 hour period of exposure in this study. I concluded that the Na_2SO_4 is not as detrimental as NaCl to the corrosion resistance.

The aluminide coated 9Cr-1Mo steel shows good oxidation resistance up to 850°C while the alloy traditional only can be used under 650°C. At 950°C, the fast growing aluminide layer has a different expansion coefficient than oxide scale, leading to scale cracking, oxygen penetration, and internal oxidized, evidenced by a rapid mass gain. Based on these data, it is recommended that hot dipped aluminde 9Cr-Mo steel be restricted to temperatures below 850°C if NaCl is not in contact with it.

Table 4 Summary of 310SS hot corrosion research discovery

Test items	**Key notes**
simple oxidation	The weight-gain kinetics is a parabolic rate law after 3hr.
Mixed-salt corrosion	● The weight-gain kinetics is a multi-stage growth rate involved in the steady and after breakaway state corrosion. ● Corrosion attack increases as the NaCl content increases in mixtures ranging from 25% to 75% NaCl, and alloy deposited with 75% NaCl mixture experiences the most severe attack. ● NaCl induces hot corrosion results in the formation of uniform internal attack. The depth of internal attack increases with increasing NaCl content. ● The corrosion rate of NaCl deposition is at least four orders of magnitude higher than that of simple oxidation. ● The corrosion rate with 100% Na_2SO_4 deposition is two orders of magnitude higher than that of simple oxidation.
morphalogy	● Corrosion products of specimens coated with 100% NaCl after exposure for 24 hr are similar to products with 75% and 50% NaCl mixtures. Fe_2O_3, $(Fe,Cr)_2O_3$, and Cr_2O_3 are the main corrosion products in the external scale, and minor spinels such as $FeCr_2O_4$ and $NiCr_2O_4$ exist on the external scale-subscale interface. ● NiS, FeS, and chromium sulfides exist on the alloy substrate. Metal sulfides become more apparent as Na_2SO_4 content increases to 50% in the salt mixtures.
Corrosion mechanism	● The mechanism of NaCl-induced hot corrosion is the oxychloridation, chloridation, and re-oxidation process. ● Hot corrosion under 801°C will be dominated by molten salt due to the low-melting-eutectic NaCl-Na_2CrO_4 and exothermic reaction process. ● The formation of voids is due to the selective chloridation of chromium and iron, leading to the outward migration of these elements, and resulting in molten salts filling in voids by capillary action.
Voids formation	Selective chloridation of chromium and iron causes the formation of voids at the substrate and the filling in of molten salt in the voids, leading to the formation of a uniform interconnecting void-oxide network in the alloy substrate.

Table 4 (cont.)

Test items	**Key notes**
Cyclic thermal	● The repeated NaCl deposition leads to severe corrosion loss as well as internal void formation, and oxide scale spalled during every thermal cycle test. The total depth of attack increases rapidly with increasing cycles. ● The hot-dipped alloy with repeated NaCl deposits shows much better corrosion resistance than that without aluminum coating in thermal cycling test. ● The repeated NaCl deposit causes the breakdown of the coated layer after five cycles. When the protective coatings break down, the corrosion behavior of 310SS alloy is similar to that observed in uncoated control specimens. ● The total depth of attack increases with increasing cycles. The specimens is fully penetrated after nine test cycles at 850°C.
HDA 310SS	● The total depth of attack increases with increasing cycles. The specimens is fully penetrated after nine test cycles at 850°C. ● For the coated specimens with repeated NaCl deposits, the aluminized layers are adherent on the specimens during the first four heating-cooling test(850°C) and voids form in the aluminized layer. After four cycles of testing, a thick alumina oxide scale forms on the outer aluminized layer and interconnecting void networks have been spread over the aluminized layer

Table 5 Summary of 9Cr-1Mo steel hot corrosion research discovery

Test items	**Key notes**
simple oxidation	● The weight-gain kinetics is a parabolic rate law after 3hr. ● It follows the parabolic rate law up to 50 hr at 750 and 850°C, while specimens follow parabolic oxidation rate law only to about 25 hr under 950°C. It shows that the alloy oxidation rate increase with increasing temperature. ● There is no scale spalling during each cyclic test at 750 and 850°C.
Corrosion mechanism	● The mechanism of NaCl-induced hot corrosion is the oxychloridation, chloridation, and re-oxidation process. ● Hot corrosion under 801°C will be dominated by molten salt due to the low-melting-eutectic NaCl-Na_2CrO_4 and exothermic reaction process.
Voids and crack formation	● Voids and cavities form beneath the Aluminum oxide layer due to oxidation consumption and inward diffusion of Al. ● Vacancies arising from differential diffusion rates of Fe and Al condense into voids along the interface between FeAl intermetallic compound and the steel substrate. ● The thermal expansion mismatch at the interface between the brittle Fe_2Al_5 + $FeAl_2$ layer and the steel substrate caused a tensile stress to be generated in the Fe_2Al_5 + $FeAl_2$ layer during heating and cooling, leading to the formation of cracks. ● Al in Fe_2Al_5 + $FeAl_2$ surrounding precipitated FeAl diffused outwardly into FeAl island, causing the transformation of Fe_2Al_5 + $FeAl_2$ transferred into FeAl, leading to the growth of FeAl and vacancies generated in FeAl island
Cyclic thermal	● without NaCl deposition, the thickness of aluminide layer retained constant and cracks formed in the aluminide layer in all cases, regardless of temperature and thermal cyclic times. ● The internal voids near the aluminide layer/substrate interface grew readily with increasing cyclic times under 750 and 850°C temperatures tests.

Table 5 (cont.)

Test items	**Key notes**
HDA 310SS	● The aluminide layers degraded after 5 cycles at 750°C and 4 cycles at 850°C. ● NaCl deposition leads to accelerated-degradation of hot-dip aluminum-7%silicon coatings on the steel substrate, especially at 850°C.
morphalogy	● The structure of the aluminide layer can be distinguished into two layers, an aluminum topcoat and an inner layer composed of Fe-Al intermetallic compounds with dissolved Si and minor Cr. ● For 10min oxidation at 850°C, phases present in the aluminide layer are similar to that of as-coated specimen, which consist of Al, Si, $FeAl_3$, Fe_2Al_5, and $FeAl_2$. ● For oxidation at 750°C for 24hr, phases present in the aluminide layer as if seen at 850°C for 1hr, which consist of mainly Fe2Al5, FeAl2, and FeAl phases. ● Oxide at 750°C for 56hr is analogous to Oxide at 850°C for 8hr. Oxide at 850°C for 56hr is analagous to Oxide at 950°C for 8hr. Five distinct layers from external scale to matrix are observed: Al_2O_3+FeAl, FeAl, Fe_2Al+Fe_2Al_5, FeAl, and the steel substrate, respectively. ● There were twice as many cracks in the aluminide layer exposed for 20min as there were after 10min.

REFERENCES

[1] A.A. Elliott, P. Ansarim and R. Nabovi, Corr. Sci. 44 (1988) 544.

[2] G.W. Meetham, J. Mater. Sci. 26 (1991) 853.

[3] G.Y. Lai, High-Temperature Corrosion of Engineering Alloys, American Society for Metals, Materials Park, OH, 1990, p.54.

[4] Y. Kawahara, Corr. Sci. 44 (2002) 223.

[5] Y. Shinata, F. Takahashi, and K. Hashiura, Mater. Sci. and Eng. 87 (1987) 399.

[6] Action Stainless Kwa Zulu Natal, Grade of Stainless-Grade 310, http://askzn.co.za /tech/tech_grade_310.htm, (accessed February 2, 2004)

[7] A.S. Khanna, Introduction to High Temperature Oxidation and Corrosion, American Society for Metals, Materials Park, OH, 2002, p. 230.

[8] Y. Ihara, H. Ohgame and K. Hashimoto, Trans. Jan. Inst. Metals. 25 (1984) 96.

[9] C.M. Schillmoller, Chem. Eng. (1980) 161.

[10] N.S. Jacobson, Oxid. Met. 26 (1986) 157.

[11] C.J. Wang, J.W. Lee and T.H. Twu, Surf. Coat. Tech. 163 (2003) 37.

[12] C. Dang, Ngoc Chan, C. Huvier, and J.F. Dinhut, Intermetallics, 9 (2001) 817.

[13] H.E. Boyer and T.L. Gall, ASM Metals Handbook, American Society for Metals, Materials Park OH, 9th ed. Vol.5, 1982, p. 333.

[14] C.J. Wang and C.C. Li, International Conference on Metallurgical Coatings and Thin Films 2003, April 28 - May 2, San Diego, CA, Paper #A1-2-8.

[15] A.P. Greeff, C.W. Louw and H.C. Swart, Surf. Interface Anal. 30 (2000) 120.

[16] A.P. Greeff, C.W. Louw and H.C. Swart, Corros. Sci. 42 (2000) 1725.

[17] A.P. Greeff, C.W. Louw and J.J. Terblans, Corros. Sci. 42 (2000) 991.

[18] S.R. Pillai, N.S. Barasi and H.S. Khatak, Oxid. Met. 53(2000)193.

[19] R.K.S. Raman, A.K. Tyagi and J.B. Gnanamoorthy, Mater. Sci. Tech. Ser. 14 (1998) 362.

[20] K. Suzuki, S. Kumai and H. Kushima, Tetsu. To Hagane, 89 (2003) 691.

[21] T. Itagaki, K. Nakazato and H. Kutsumi, J. Jpn. I. Met. 67 (20034) 189.

[22] N. Eberle and F.L. Jones, Mater. Sci. Tech-lond, 19 (2003) 365.

[23] T. Sundararajan, S. Kuroda, T. Itagaki and F. Abe, Isij. Int. 43 (2003) 95.

[24] T. Sundararajan, S. Kuroda, T. Itagaki and F. Abe, Isij. Int. 43 (2003) 104.

[25] H. Kutsumi, T. Itagaki and F. Abe, Testu. To Hagane, 88 (2002) 520.

[26] Z. Tokei, H. Viefhaus and H.J.Grabke, Appl. Surf. Sci. 165 (2000) 23.

[27] J. Hucinska, Mater. Corros. 51 (2000) 173.

[28] J. Hucinska, Mater. Corros. 50 (1999) 267.

[29] M. Vijayalakshmi, S. Saroja and V.S. Raghunathan, Scripta. Mater. 41 (1999) 149.

[30] S.R. Pillai, N.S. Barasi, H.S. Khatak and J.B. Gnanamoorthy, Oxid. Met. 49 (1998) 509.

[31] D. Laverde, T. Gómez-Acebo and F. Castro, Corr. Sci. 46 (2004) 613.

[32] J. Wang and T.T. He, Oxid. Met. 58 (2002) 415.

[33] Z.W. Li, W. Gao, P.M. Kwok and Y. He, High Temp. Mater. Proc. 19 (2000) 443.

[34] W.T. Tsai and K.E. Huang, Thin Solid Films 366 (2000) 164.

[35] H.W. Hsu and W.T.Tsai, Mater. Chem. Phys. 64 (2000) 147.

[36] D.R. Gaskell, Introduction to the Thermodynamics of Materials, 3rd Ed., Taylor and Francis, Washington, D.C., 1995, p. 370.

[37] J. Botella, J. Almagro, E. Otero, P. Hierro and C. Merino, Rev. Metal Madrid 35 (1999) 22.

[38] W. Kai, C.J. Leu and Y.J. Wu, Oxid. Met. 50 (1998) 122.

[39] M.P. Sibi and Z.G. Zong, Prog. Org. Coating 47 (2003) 8.

[40] I.G. Wright, in Metals Handbook, 9th ed., Vol 13, Corrosion, ASM International, Materials Park, OH, 1987, p. 97.

[41] G. H. Meier, Matl. Sci. Eng. A120 (1989) 1.

[42] C. Wagner, Z. Elektrochem. 63 (1959) 772.

[43] R. A. Rapp, Acta Metall. 9 (1961) 730.

[44] F. Gesmundo and F. Viani, Oxid. Met. 25 (1986) 269.

[45] A. Atkinson, Corros. Sci. 22 (1982) 87.

[46] T. Adachi and G. H. Meier, Oxid. Met. 27(1987) 347.

[47] D. L. Douglass, P. Nanni, C. De Asmundis and C. Bottino, Oxid. Met. 28 (1987) 309.

[48] F. S. Pettit, Trans. Metall. Soc. AIME 239 (1967) 1296.

[49] C. Wagner, J. Electrochem. Soc. 99 (1952) 369.

[50] G. H. Meier, D. Appalonia, R. A. Perkins and K. T. Chiang, in T. Grobstein and J. Doychak (eds.), Oxidation of High Temperature Intermetallics, American Society for Metals, Materials Park, OH, 1989, p. 185.

[51] K. Hirano and Y. Iijima, in M. A. Dayananda and G. E. Murch (eds.), Diffusion in Solids: Recent Developments. Metallurgical Society, Warrendale, PA, 1985, p. 315.

[52] A. Grodner, Weld Res. Counc. Bull. No.31, 1956.

[53] The Making, Shaping and Treating of Steel, H.E. McGarrow, Ed., United States Steel Corp. Pittsburgh, PA, 1971, p. 1136.

[54] A.P. Greeff et al., Corrosion Science 42 (2000) 991.

[55] H. J. Grabke, in E. Lang (ed.), The Role of Active Elements in the Oxidation Behaviour of High-Temperature Metals and Alloys, EEC, Amsterdam, 1989, p. 229.

[56] C. S. Giggins and F. S. Pettit, Oxid. Met. 14 (1980) 363.

[57] C. J. Spengler and R. Viswanathan, Metall. Trans. 3 (1972) 161.

[58] G. M. Kim, Ph.D. Dissertation, University of Pittsburgh, PA,1986.

[59] C. S. Giggins and F. S. Pettit, J. Electrochem. Soc. 118 (1971) 1782.

[60] G. R. Wauwork and A. Z. Heal, Oxid. Met. 3(1971) 171.

[61] R. A. Perkins, K. T. Chiang and G. H. Meier, Scr. Metall 21 (1987) 1505.

[62] R. A. Perkins, K. T. Chiang and G. H. Meier, Scr. Metall. 22 (1988) 419.

[63] A.W. Zeuthen, Heating, Piping and Air Conditioning 42 (1970) 154.

[64] D. P. Whittle, in R. A. Rapp (ed.), High Temperature Corrosion, NACE, Houston, TX, 1983, p. 171.

[65] G.Y. Lai, High-Temperature Corrosion of Engineering Alloys, American Society for Metals, Materials Park, OH, 1990, p. 154.

[66] Y. Bourhis, C St. John, Oxid. Met. 9 (1975) 507.

[67] Y. Niu, F. Gesmundo, F. Viani and W. Wu, Oxid. Met. 42 (1994) 265.

[68] D.M. Johnson, D.P. Whittle and J. Stringer, Corr. Sci. 15 (1975) 649.

[69] D.M. Johnson, D.P. Whittle and J. Stringer, Corr. Sci. 15 (1975) 721.

[70] ASTM, Standard Practice for Simple Static Oxidation Test, G54-84, 1996.

[71] A.U. Seybolt, Oxid. Met. 2 (1970) 119.

[72] A.U. Seybolt, Oxid. Met. 2 (1970) 161.

[73] Y. Shinata, Oxid. Met. 27 (1987) 315.

[74] C. J. Wang and T. T. He, Oxid. Met. 58 (2002) 415.

[75] Y. Shinata, M. Hara and T. Nakagawa, Mater. Trans. JIM 32 (1991) 969.

[76] N. Hiramatsu, Y. Uematsu, T. Tanaka and M. Kinugasa, Mater. Sci. and Eng. A120 (1989) 319.

[77] A. Holt and P. Kofstad, Mater. Sci. and Eng. A120 (1989) 101.

[78] O. Kubaschewski, C. B. Alcock, P.J. Spencer (Eds.), Materials Thermochemistry, 6th ed., Pergamon Press, Tarrytown, NY, 1993, p. 272-299.

[79] V. Buscaglia, P. Nanni and C. Bottino, Corr. Sci. 30 (1990) 327.

[80] M.A. Clevinger, K.M. Kessell, C.G. Messina, and H.M. Ondik (Eds.), Phase Diagrams for Ceramists, The American Ceramic Society, Inc., Columbus, OH, 1989, Fig. 7109.

[81] T. Narita and T. Ishikawa, Mater. Sci. and Eng. A120 (1989) 31.

[82] R. Santorelli, E. Sivieri and R.C. Reggiani, Mater. Sci. and Eng. A120 (1989) 283.

[83] P. Elliott, A. A. Ansari, and R. Nabovi, Corr. Sci. 44 (1988) 544.

[84] Y. Lai, M. F. Rothman, S. Baranow, and R. B. Herchenroeder, J. Metals 24 (1983).

[85] M. K. Hossain and S. R. J. Saunders, Oxid. Met., 12 (1978) 1.

[86] N. Hiramatsu, Y. Uematsu, T. Tanaka, and M. Kinugasa, Mater. Sci. Eng. A120 (1989) 319.

[87] O. Kub and E. II. Erans, in "Metallurgical Thermo-chemistry", Pergamon Press, Tarrytown, NY, 1958, p. 225.

[88] M.A. Uusitalo, P.M.J. Vuoristo and T.A.M. Mantyla, Corros. Sci. 46 (2004) 1311.

[89] C. J. Wang and Y. C. Chang, Oxid. Met. 57 (2002) 363.

[90] Y. Shu, F. Wang, and W. Wu, Oxid. Met. 54 (2000) 457.

[91] Y. Shu and F. Wang, Oxid. Met. 59 (2003) 201.

[92] A. Zahs, M. Spiegel, and H. J. Grabke, Corros. Sci. 42 (2000) 1093.

[93] O. Knacke, O. Kubaschewski, and K. Hesselmann, in Thermochemical Properties of Inorganic Substance, Springer-Verlag Berlin, 1991, p. 251.

[94] G. A. Capuano, A. Dang, U. Bernabai, and F. Felli, Oxid. Met. 39 (1993) 263.

[95] S. Pillai, N. S. Barasi and H. S. Khatak, Oxid. Met. 53 (200) 193.

[96] Z. Tokei, H. Viefhaus, and H. J. Grabke, Appl. Surface Sci. 165 (2000) 23.

[97] H. Glasbrenner and J. Konys, Fusion. Eng. Des. 58 (2001) 725.

[98] H. Glasbrenner and O. Wedemeyer, J. Nucl. Mater. 257 (1998) 274.

[99] S. Kobayashi and T. Yakou, Mater. Sci. Eng. A338 (2002) 44.

[100] Y. B. Liu, M.Z. Zhang and B. Yang, J. Mater. Proc. Technol. 120 (2002) 30.

[101] A.D. Smigelskas and E.O. Kirkendall, Trans. AIME 171 (1947) 130.

VITA

Charng-Cheng Tsaur

4F., No.5, Alley 2, Lane 131, Sec. 1, Chong-Ren Rd.,
Beitou District, Taipei City 112, Taiwan (R.O.C.)

Education

Master of Science in mechanical engineering
National Central University (May 1992)

Diploma of Mechanical Engineering
National Taipei Institute of Technology (May 1986)

Professional Experience

1998 – present (Researcher)
1994 – 1998 (Associate Researcher)
1992 – 1994 (Assistant Researcher)
Safety division, Institute of Occupational Safety and Health, The Council of Labor Affairs, Executive Yuan, R.O.C.
1988-1990 (Mechanical Specialist)
Department of Environmental protection, City of KaoXiong, Taiwan